Naval Research Laboratory
Washington, DC 20375-5320

UNCLASSIFIED

NRL/FR/7227--93-9547

Models of Refraction in the Marine Atmospheric Surface Layer

JOHN S. HORNSTEIN
RICHARD G. PRIEST
EDWARD H. TAKKEN
DAVID BAUKMAN

Remote Sensing Physics Branch
Remote Sensing Division

September 30, 1993

REPORT DOCUMENTATION PAGE

Form Approved
OMB No. 0704-0188

1. AGENCY USE ONLY (*Leave Blank*)	2. REPORT DATE	3. REPORT TYPE AND DATES COVERED
	September 30, 1993	

4. TITLE AND SUBTITLE

Models of Refraction in the Marine Atmospheric Surface Layer

5. FUNDING NUMBERS

PE - 62111N
TA - 2
PR - RA11M16

6. AUTHOR(S)

John S. Hornstein, Richard G. Priest, Edward H. Takken, and David Baukman

7. PERFORMING ORGANIZATION NAME(S) AND ADDRESS(ES)

Naval Research Laboratory
Washington, DC 20375-5320

8. PERFORMING ORGANIZATION REPORT NUMBER

NRL/FR/7227--93-9547

9. SPONSORING/MONITORING AGENCY NAME(S) AND ADDRESS(ES)

Office of Naval Research
Arlington, VA 22217-5000

10. SPONSORING/MONITORING AGENCY REPORT NUMBER

11. SUPPLEMENTARY NOTES

12a. DISTRIBUTION/AVAILABILITY STATEMENT

Approved for public release; distribution unlimited.

12b. DISTRIBUTION CODE

13. ABSTRACT (*Maximum 200 words*)

Models of near-surface refraction are compared with one another and are used to survey effects relevant to the design and use of optical and infrared sensors.

14. SUBJECT TERMS

Refraction, Propagation, Mirages, Optical, IRST, Refractive ducts, Infrared, Atmospheric surface layer

15. NUMBER OF PAGES

83

16. PRICE CODE

17. SECURITY CLASSIFICATION OF REPORT	18. SECURITY CLASSIFICATION OF THIS PAGE	19. SECURITY CLASSIFICATION OF ABSTRACT	20. LIMITATION OF ABSTRACT
UNCLASSIFIED	UNCLASSIFIED	UNCLASSIFIED	UL

NSN 7540-01-280-5500

Standard Form 298 (Rev. 2-89)
Prescribed by ANSI Std 239-18
298-102

CONTENTS

MODELS OF REFRACTION IN THE MARINE ATMOSPHERIC SURFACE LAYER

INTRODUCTION

Designers of infrared (IR) systems have long sought usefully simple but validated models of IR propagation in the atmospheric boundary layer. In addition to being useful for system design, such models would allow the development of adaptive systems which would exploit nearby meteorological measurements. The prospects for simple but validated models are best for the marine atmospheric boundary layer, where major topographic features are absent and the atmosphere is often statistically homogeneous in the horizontal direction.

This report compares several presently available computer programs for computing refractive indices and for tracing rays in the marine atmospheric boundary layer. The programs are compared with each other and with data obtained from two IR sensors. The comparison includes four programs for computing refractive structure, and two codes for tracing the rays. Two of the programs for computing the refractive profiles were provided by the Defence Research Establishment, Valcartier (DREV), Canada. The third refractive profile program was provided by the Naval Ocean Systems Center (NOSC), San Diego, California. The fourth refractive profile program is an implementation by the Naval Research Laboratory (NRL) of a model developed at the Naval Postgraduate School (NPGS). These four codes were used to provide refractive profiles for use by the three ray tracing programs, one developed by NOSC and two developed by NRL. Effects of ray bending are surveyed over a broad range of meteorological conditions using the most recent DREV refractive-profile code and one of the NRL ray-tracing codes. The surveyed results are compared to over-water measurements taken at Wallops Island, Virginia, using a PtSi sensor which is sensitive in the mid-wave (MW) IR spectral region and has very good angular resolution; these measurements were part of the Infra-Red Analysis, Measurements and Modeling Program (IRAMMP). The comparison is preliminary, since the sensor and target heights used in the calculated survey differed from those in the field measurements, but shows the model to account for the main features of the experimental data. The model in conjunction with the data is able to bypass a standard problem in field measurements; namely, that it is usually not possible to determine the absolute origin of angular measurements obtained with a sensor having a narrow field of view. The absolute origin can be estimated from the data used in combination with the refractive model. With an estimate of the absolute origin, many more aspects of the observed ray-bending effects can be compared to the model than would otherwise be possible.

The scenario of interest is an IR source traveling horizontally at some low or moderate altitude above the sea surface, as it appears to an IR sensor mounted on a ship. The aspects of greatest interest are the range at which the IR source first becomes potentially visible to the sensor, and on its apparent direction as it continues to approach the ship. (Because of mirages, the source may sometimes appear in two directions. Both directions are of interest here.) These quantities would be useful in designing both

Manuscript approved January 15, 1993.

sensor hardware and algorithms for detecting and tracking sea-skimming IR sources. Simple formulas (Beaulieu, 1992, pp. 43-44) already exist for predicting the range of first potential visibility, but a ray tracing model capable of taking into account all the important variables will probably be necessary for adequate accuracy. Formulas are not available for the apparent direction(s) of the source as a function of range, and because of the complexity of the phenomenon, simple formulas probably do not exist. Ray tracing models will therefore be indispensible for modeling the apparent directional behavior of the source.

OVERVIEW OF REFRACTION IN THE MARINE BOUNDARY LAYER

Figure 1 shows two bundles of rays illustrating propagation in the marine boundary layer. For convenience, the rays were traced outward from the sensor rather than from the source. (This assures that all traced rays will pass through the sensor. Because the rays are reversible, the sense in which they are traced does not affect the ray trajectories.) The displayed ray trajectories are suitable for analyzing the visibility of IR sources whose altitudes are lower than the sensor's. The bundle of rays in Fig. 1(a) illustrates phenomena occurring when the temperature of the air decreases with altitude, while that in Fig. 1(b) illustrates phenomena occurring when the air temperature increases with altitude over at least some range of altitudes. (The concavity of the ray trajectories in Fig. 1 is due to the use of a flattened-Earth plot. Because the refractive index generally decreases with height, the ray trajectories would be convex on a plot in which the Earth's surface was represented by a circle.)

In Fig. 1(a) (air becoming colder with increasing altitude) the bundle of rays folds over on itself. This is especially evident when the ray tracing is watched on a computer monitor. As the launch angle of the rays is lowered, the rays dip closer to the ground. Rays launched sufficiently steeply downward enter a region of strong refractive gradients; this region acts increasingly like a mirror as the steepness of the launch angle increases. As the launch angle becomes steeper, the angle of incidence at the approximate mirror increases, and the "reflections" become steeper. Although the along-surface ranges of the "reflections" increase slightly with the downward steepness of launch, the increase in range is weak, and is more than compensated by the increase in the steepness of rise of the reflected ray. Consequently, the steeply rising "reflected" rays cross the less steeply rising rays which had been launched less steeply downward; the crossing produces the "folding over" of the ray bundle in Fig. 1(a). Rays launched sufficiently steeply downward (more steeply than the "folding" rays just discussed), strike the surface. (The subsequent fate of surface-striking rays is discussed later.)

The folding of the ray bundle corresponds to mirages. A source placed at the intersection of two rays has two paths by which light can reach the sensor. These paths arrive at the sensor in different directions, so the sensor sees the single source as two similar but distinct sources.

In Fig. 1(b), where the air becomes warmer with the increasing altitude, the bundle of rays is torn or bifurcated. Rays launched downward, but not too steeply, eventually rise and escape. Rays launched steeply downward strike the surface. A ray launched at some intermediate angle must asymptotically approach a trajectory having constant altitude above the surface, that is, a circular orbit concentric with the center of the Earth. The density of rays is very small in the vicinty of the asymptotically circularly orbiting ray, so the two extreme behaviors (escaping upward versus striking the surface) seem to define two branches separated by a tear.

The altitude of the asymptotically circular orbiting ray defines the top of a refractive *duct*. The term *duct* is used because many of the rays emitted by a source at an altitude slightly below the duct would

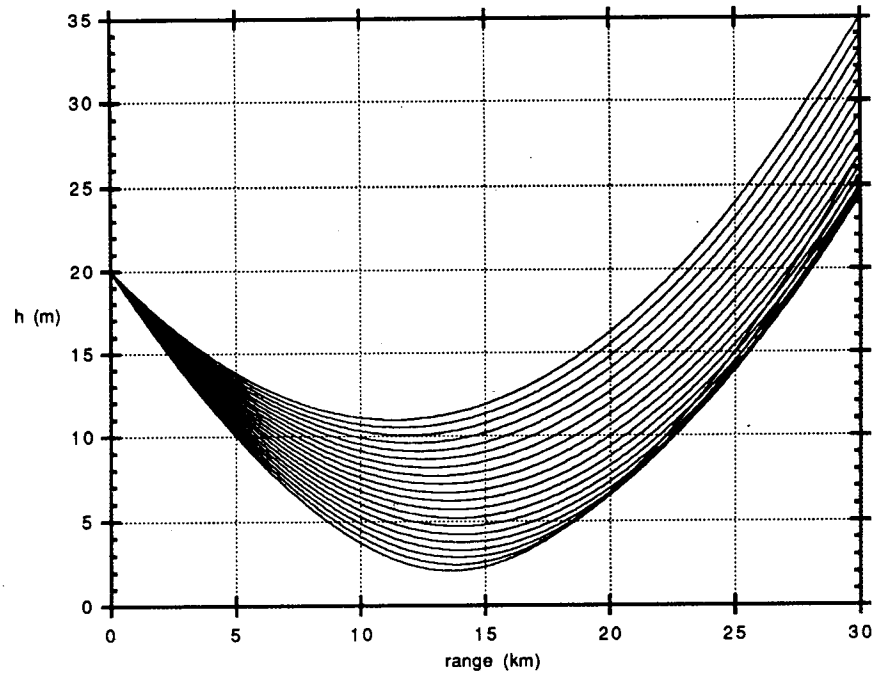

(a)

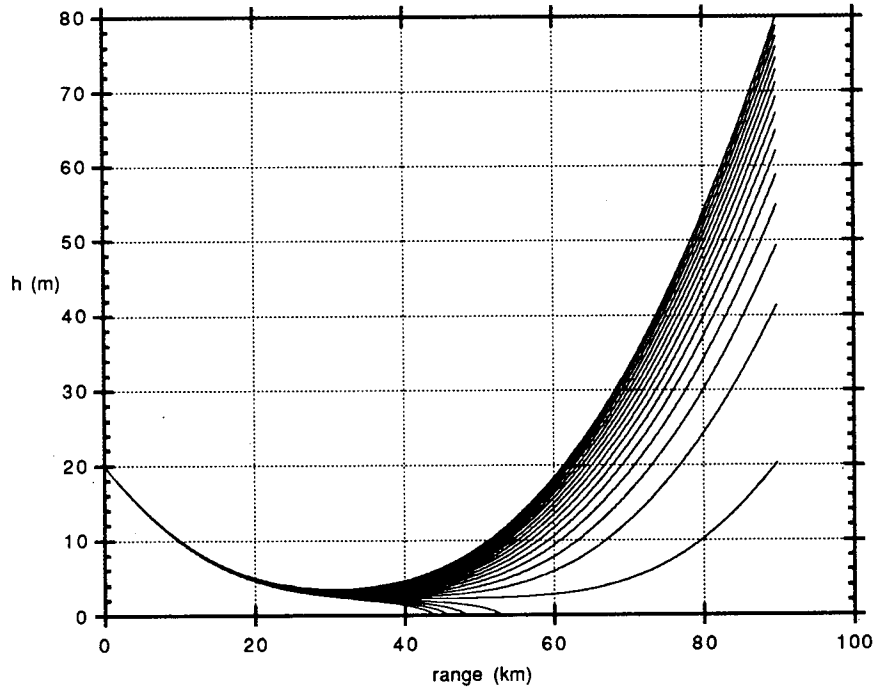

(b)

Fig. 1 — Ray trajectories. Part (a) is for ASTD = −7, and part (b) is for ASTD = +2.5. In both cases the surface temperature is 20°C, the relative humidity is 90%, the wind speed is 4 m/s, and effects of wave topography are not included.

be trapped in the duct by total internal reflection; if the surface were reflective at the wavelengths in question, the trapped rays could travel long distances without rapidly losing intensity from geometric spreading. Chapter V of Livingston (1970) gives a detailed discussion of propagation in the presence of ducts.

It will be useful to have a qualitative understanding of how the behaviors in Figs. 1(a) and 1(b) arise from the corresponding refractive profiles. In this qualitative analysis it is helpful to remember that Fig. 1 is a flattened-Earth diagram. A ray (or ray segment) which is horizontal on the diagram corresponds to a circle in three dimensions: a circle concentric with the center of the Earth and having a radius of curvature negligibly larger (by at most a few tens of meters) than the radius of the Earth. A straight, unrefracted ray would have an infinite radius of curvature in a curved-Earth diagram, but appears curved in the flattened-Earth diagram. Because of the curvature of the Earth, the surface would fall away from a horizontally launched unrefracted ray, so the altitude of such a ray would increase with range. Much of the behavior of rays in the lower atmosphere can be conveniently understood in terms of two effects, which may act in the same or opposite directions: (1) the Earth's surface pulling away from the horizontal, tending to increase the altitude of rays; (2) the tendency of rays to be drawn toward the region of larger refractive index, which usually pulls them downward.

The refractive profiles which produced the rays in Figs. 1(a) and 1(b) are shown in Fig. 2(a) and 2(b), respectively. The figures show the profile of the refractivity N, which is related to the usual refractive index n by $N = 10^6(n - 1)$. The refractive index profile is almost completely determined by the density profile; compositional changes associated with the humidity profile are small and usually have little effect (apart from a few exceptions to be discussed later). In Fig. 1(a) the decrease of temperature with altitude counters the decrease in density with altitude which would have occurred in an isothermal atmosphere. The refractive gradient is therefore relatively small, except for ray segments very close to the surface. Ray segments close to the surface encounter a large refractive gradient. Near-surface ray segments which are not too vertical are "reflected" by the abrupt change in impedance corresponding to the large refractive gradient. Near-surface ray segments which are sufficiently vertical are drawn toward the region of larger refractive index, and strike the surface at a smaller range from the source than if they had not been refracted. In Fig. 1(b) the temperature increases with altitude over some range of altitudes, corresponding to a temperature inversion. Over this range of altitudes, the density (and therefore the refractive index) falls with altitude faster than it would for an isothermal atmosphere. But this is only a local deviation from the large-scale decrease of temperature with altitude. Since the refractive index increases downward, some rays which would not have struck the surface in the absence of refraction are pulled downward by the enhanced refractive gradient and now strike the surface; these rays constitute the lower branch in Fig. 1(b). For rays launched horizontally at a particular altitude, the "downward pull" of the thermally-enhanced downward refractive gradient exactly balances the falling away of the Earth's surface, so the ray's altitude remains constant. This corresponds to the circular orbiting ray which defines the duct. (This ray is not shown in Fig. 1(b), which shows only rays launched above the duct; the ray would correspond to a horizontal line through the cusp of the tear in Fig. 1(b).) Rays launched above the duct, but not aimed too steeply downward, encounter a weaker refracting gradient than the orbiting ray does, so the falling away of the Earth's surface wins out over the downward pull of the refractive gradient. Such rays escape and constitute the upper branch in Fig, 1(b).

To show the manner in which the ray traces will ultimately be used, it is useful to apply Fig. 1 to discuss how an approaching boat or sea-skimming air vehicle would appear to a sensor. Consider a source approaching at constant altitude. The apparent direction of the source is shown as a function of range in Figs. 3(a) and 3(b), which corresponds to the ray bundles in Figs. 1(a) and 1(b), respectively.

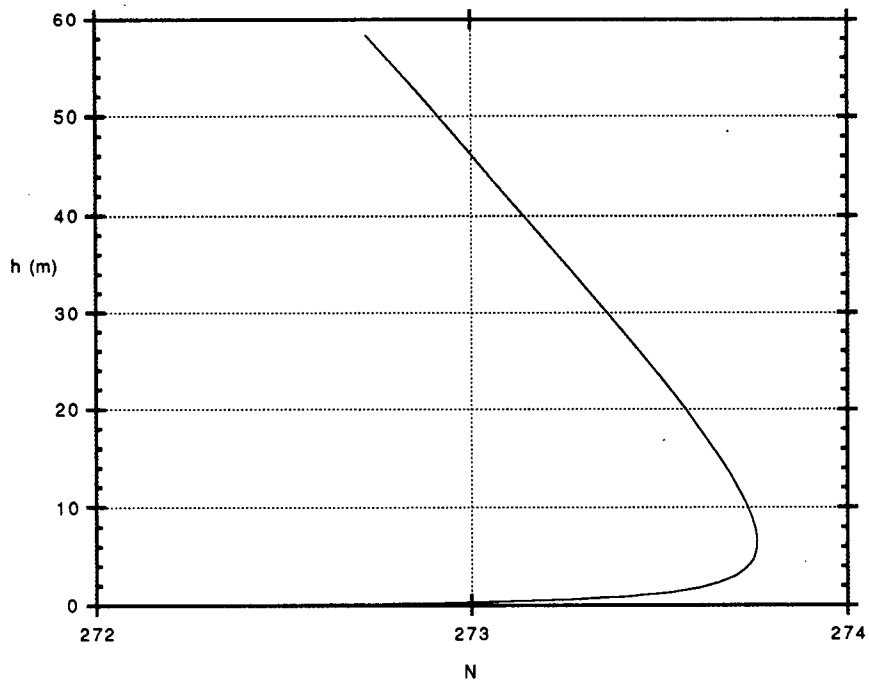

(a)

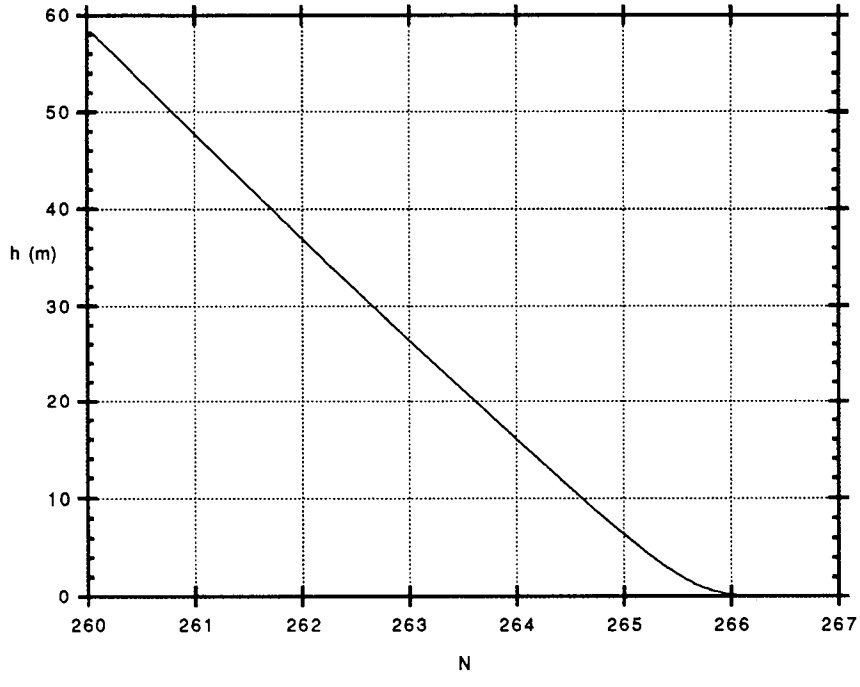

(b)

Fig. 2 — Profiles of refractivity (N). Parts (a) and (b) correspond to parts (a) and (b)) of Fig. 1.

In Fig. 3(a), the source is first potentially visible when it encounters the lower edge of the bundle of rays in Fig. 1(a), i.e., the curve along which the bundle has "folded." Mathematically, the fold curve is the envelope of the rays belonging to the bundle. Since the folding corresponds to a mirage, the image of the target will split. As the source continues to approach, the directions of the two images will vary according to the launch angles of the pair of rays which intersect at the source's current position. The lower image is due to rays which dip relatively close to the surface, where they are more affected by aerosol absorption and scattering, by scattering by turbulence, and by obstruction by an occasional high wave. So the lower image is likely to be fainter and more variable than the upper image.

In Fig. 1(b), a source is not likely to be seen while it is within the V-shaped region of low intensity (the tear), because of the low density of rays there. To understand how image behavior is deduced from the ray trajectories, it is useful to consider both sources which approach at a constant altitude below the top of the duct as well as those approaching at altitudes above the duct. (Unless the air-surface temperature difference exceeds 2.5°C, the top of the duct is below 2.5 m, so actual targets are unlikely to fly below the top of the duct.) If the source were below the top of the duct, it would first become potentially visible when it encountered the lower, surface-striking branch of the ray bundle. The range at first detection would therefore be relatively small; in addition, the rays in the lower branch are subject to the same weakening mechanisms as those which affect the lower mirage in Fig. 1(a), so the image would be relatively dim and turbulent. After a source traveling within or along the top of the duct first becomes visible, the rays it encounters in Fig. 1(b) correspond to rays launched from the sensor at progressively more steeply downward directions; hence the image sinks steadily as it approaches. In contrast, a source traveling above the duct first becomes significantly visible when it encounters the lower edge of the upper branch of the tear. (Ambiguities in the definition of the "edge" of the tear are discussed later.) As the source approaches, it first encounters rays launched in directions sucessively closer and closer to the horizontal, so its image at first rises. But after the source encounters the ray which is tangent to the source altitude, it encounters rays which are launched at increasingly downward directions, and therefore its image seems to fall. Mirages never occur in Figs. 1(b) or 3(b).

For the applications of interest here, the quantities of greatest interest are the range and apparent direction of a source when it first becomes potentially visible, and the history of the direction and strength of the images of the source as a function of the source's range. At the range when a source first becomes potentially visible, it is geometrically possible for the sensor to see the source, but the sensor will actually see the source only if the source is bright enough relative to the attenuation along the refracted path from source to sensor, and relative to path radiance or any other radiance from the portion of the ray on the far side of the source.

When the air-sea temperature difference (ASTD) is negative, there is a maximum along-surface range at which refracted rays from a source can first reach the sensor; even a very bright target cannot be seen until it encounters the edge of the envelope formed when the bundle of rays folds over on itself. This range is called the *maximum intervisibility range* (traditionally denoted MIVR). The detection range for an actual target will be less than the MIVR; the deviation from the MIVR will depend upon the brightness of the target, the background, and the quality of the sensor. But the deviation will be small, because the density of rays does not vary rapidy once the source has crossed the MIVR. So for most practical purposes, the MIVR constitutes a universal approximant to the detection range, useful for almost any combination of sensor, target, and atmosphere. In contrast, when the ASTD is sufficiently positive, the density of rays increases gradually as the target approaches. The detection range increases without limit as the brightness of the source increases, so no MIVR exists when the ASTD is sufficiently positive. However, for convenience in labeling plots, the term MIVR will often be used in this report even when the ASTD is positive. This usage is loose, but it is preferable to repeatedly specifying that one part of

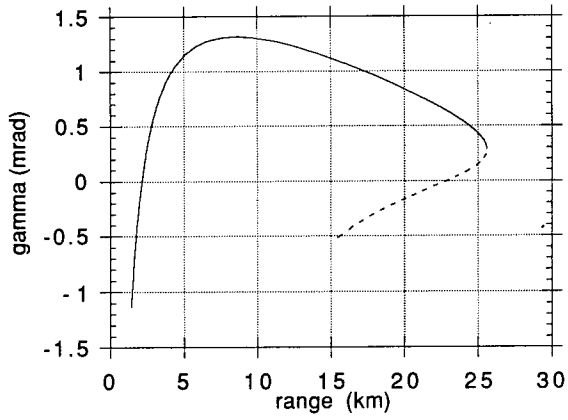

(a)

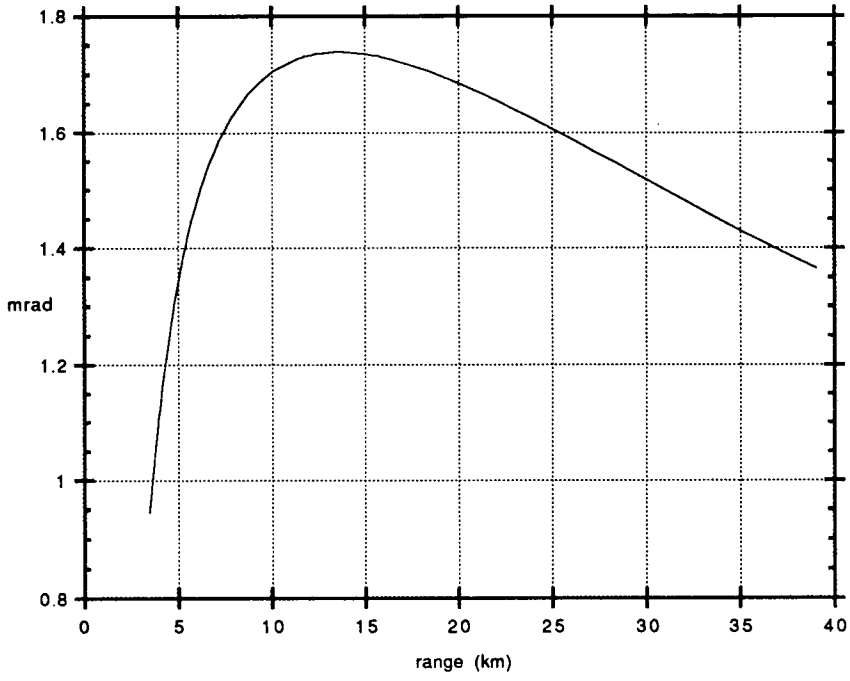

(b)

Fig. 3 — Apparent elevation as a function of true along-surface range, for a target flying 15 m above the surface and observed by a sensor 20 m above the surface. Parts (a) and (b) correspond to parts (a) and (b) of Fig. 1.

a plotted curve gives MIVRs, while the remainder of the same curve gives a quantity which can be used to calculate the detection range when combined with additional information (namely, with details of the sensor, target, and atmosphere).

In the absence of ray bending, the MIVR would always exist. It would be the along-surface separation of source and sensor when the ray joining them is tangent to the surface of the Earth. The MIVR in this case would equal the sum of the ranges of the source and the sensor from their respective horizons. This relation no longer holds when the rays bend. Given the ray corresponding to the detection range, the detection range is still the sum of the ranges of source and sensor from the point where the given ray becomes horizontal; but that point no longer in general defines the source's and sensor's apparent horizons. Indeed, as will be discussed later, when the rays bend the apparent horizon does not always exist as a sharp feature.

PHYSICS OF REFRACTION IN THE MARINE ATMOSPHERIC BOUNDARY LAYER

The refractive index n in nonionized air is close to unity over the entire electromagnetic spectrum. The small but significant deviations of n from unity are more clearly exhibited by working with the quantity $N = 10^6(n - 1)$. N is typically close to 300 for altitudes near sea level, over a wide spectral range: from the radio frequency (RF) region through the infrared and visible regions. N is usually called the *refractivity*, but it is called the *refractive modulus* in Atlas et al. (1965). The symbol N and the term *refractivity* are now standard, but beware: one standard older reference, Kerr et al. (1951, p.13), uses N to denote a different but related quantity, the *modified refractivity*, which is nowadays usually denoted M.

The first subsection below shows how the refractivity at any point in the atmosphere is determined by local atmospheric variables. The second subsection shows how the local atmospheric variables often behave in the marine atmospheric boundary layer.

Refractive Index in Terms of Intensive Variables

The refractivity at any point in the atmosphere is determined to a good approximation by the local values of a small number of intensive variables: the temperature T, the total pressure P, and the partial pressure e of water vapor. The partial pressure of dry air, $P_d = P - e$, also occurs frequently in the following discussion.

To a good approximation, the refractivity of dry air at visible and IR wavelengths is (Eqn. 9-6 in Atlas et al., 1965)

$$N = \left[77.6 + \frac{0.584}{\lambda^2}\right] \frac{P_d}{T}. \qquad (1)$$

Here P_d is in mb, T is the temperature in Kelvins, and λ is the wavelength (in vacuum) in μm. Eq. (1) applies to dry air containing 0.03% CO_2, by volume. According to the ideal gas law, the factor P_d/T is proportional to the density of dry air. Atlas et al. assert that Eq. (1) will not be in error by more than ± 1 unit at IR and visible wavelengths, throughout the troposphere.

Equation (1) implies that N depends only weakly upon wavelength exept at the shorter wavelengths in the visible. Evaluating Eq. (1) at 0.5, 5 and 10 μm gives 77.94, 77.62 and 77.61 times P_d/T,

respectively. (The fourth significant digit is not meaningful; it is given only to make the changes in N discernible.)

Equation (1) should be valid for wavelengths longer than a few times 0.2 μm, but should not be used for wavelengths shorter than that. This can be seen from Edlén's (1953) careful numerical study of the wavelength dependence of the refractivity of *standard dry air* (dry air at 15°C (288.16°K) and 1013.25 mb, with 0.03% CO_2 by volume). (Edlén's results were adopted as an international spectroscopic standard in 1952.) Edlén found

$$N(288.16K,\ 1013.25\ \text{mb},\ \lambda) = 64.328 + \frac{29498.10}{146 - \frac{1}{\lambda^2}} + \frac{255.40}{41 - \frac{1}{\lambda^2}} . \tag{2}$$

This has simple poles at wavelengths of 0.1562 and 0.08276 μm, which simulate the effects of the singularities in the photon scattering amplitude: a branch cut associated with the ionization and dissociation of air molecules, and a large number of discrete poles associated with bound states. Edlén's formula can therefore be valid only for wavelengths somewhat larger than 0.1562 μm. Figure 1 in Edlén's paper shows his formula to be valid to within about 1% even for wavelengths as short as 0.2 μm. Edlén's formula gives $N = 272.60$ for standard air as the wavelength becomes very large, which is close to the 272.86 given by Eq. (1) for the same conditions. If Edlén's formula is generalized to other temperatures and pressures by scaling by the density (as in Eq. (1)), the result is

$$N(T,P,\lambda) = 77.5 \left(1 + \frac{0.741168}{1 - \frac{1}{146\lambda^2}} + \frac{0.0228514}{1 - \frac{1}{41\lambda^2}} \right) \frac{P_d}{T} . \tag{3}$$

(Scaling by the density cannot be exact, since it fails to include the effect of changes in pressure and temperature upon the implicitly included spectral lines. Scaling by density also fails to include the effects of local fields, which, at least for non-polar molecules, can be taken into account by means of the Lorenz-Lorentz approximation. (Owens, 1967, discusses the effect of local fields upon atmospheric refraction.) But the empirical sucess of Eq. (1) shows the neglected effects to be negligible. For wavelengths sufficiently greater than 0.1562 μm, the binomial expansion allows Eq. (3) to be approximated by

$$N(T,P,\lambda) = 77.5 \left(1 + \frac{5.64 \times 10^{-3}}{\lambda^2} \right) \frac{P_d}{T} = \left(77.5 + \frac{0.437}{\lambda^2} \right) \frac{P_d}{T} . \tag{4}$$

This is similar to Eq. (1) (Atlas et al. use slightly different coefficients than Edlén); the derivation of Eq. (4) therefore shows Eq. (1) to be valid only for wavelengths exceeding a few times 0.2 μm.

A formula like Eq. (1) might be expected to fail near any of the many spectral lines which occur in the visible and infrared regions. But empirically, Eq. (1) works well. Small deviations from Eq. (1) should occur for narrow-band radiation very close to a spectral line, because of anomalous dispersion at frequencies just below the line or enhanced normal dispersion at frequencies just above the line. But the deviations are small, because most spectral lines in the visible and infrared regions are due to minority

species in the atmosphere, and also because the refractive effects of the line sits on top of contributions from the wings of the many lines below and above the frequency of interest. For broad-band radiation the deviations are even smaller: the bands detected by general purpose sensors (not specialized to a particular laser line) are broad enough to include many lines, so that the average refractivity over the band is not significantly influenced by any one line.

The saturation vapor pressure of water vapor does not exceed 43mb for temperatures below 30°C, or 74mb for temperatures below 40°C (see e.g., Table 2.1 on p.18 of Rogers, 1979). Hence using P instead of P_d in the above formula will not produce errors exceeding 4.3% at temperatures below 30°C or 7.5% at temperatures below 40°C. But the errors will be systematic: replacing P_d by P in Eq. (1) will overestimate N, and the overestimate will increase systematically with temperature. Atlas et al. (1965) ignore the distinction between P_d and P.

Water vapor has relatively little effect on the refractivity at visible and infrared wavelengths, despite its significant effect at radiofrequency (RF) wavelengths. But the effect of water vapor might not be negligible close to the sea surface, especially in the tropics. To first order, the effect of water vapor can be included by adding the refractivity of water vapor to that of dry air. (For a discussion of the approximate character of this approach, see Owens (1967).) This is the approach followed by Dion et al. (1989). For the refractivity contributed by the "dry" component they use Edlén's formula (2), scaled by the ideal gas law to the density of the dry component. For the refractivity contributed by water vapor, they use a numerical fit due to Hill and Lawrence (1986). This procedure gives

$$N(T,P,\lambda) = N_E(\lambda) \cdot \left(\frac{P_d}{T}\frac{1}{3.516}\right) + 216.7 \cdot \left(\frac{e}{T}\right) \cdot \zeta(T,\lambda) , \tag{5}$$

where N_E is Edlén's formula (2), $P_d = P - e$ is the partial pressure of the dry component, the coefficient of N_E is the ratio of the densities of the dry component at T,P_d to its value for standard dry air (3.516 is the value of P_d/T for standard dry air), 216.7 e/T is the absolute humidity (the mass density of water vapor) in g/m^3, and ζ is a numerical function given by Hill and Lawrence:

$$\zeta(T,\lambda) = \frac{0.957 - 0.928t^{0.4}(x - 1)}{1.03t^{0.17} - 19.8x^2 + 8.1x^4 - 1.7x^8} + \frac{3747}{12440 - x^2} . \tag{6}$$

In ζ, $t = T/273.16$ is a normalized temperature and $x = 10\mu m/\lambda$ is a normalized spatial frequency (in vacuum). The formula used by Dion et al. differs from Eq. (5) in two minor respects: Dion et al. have 3.518 instead of 3.516 in the dry term of Eq. (5), and they have 216.5 instead of 216.7 in the water vapor term. They have 3.518 because they believe Atlas et al.'s claim that Edlén's formula applies at a temperature of 288°K; but Altas et al. cite a rounded value, since Edlén actually used 288.16°K (15°C). The number 216.7 arises as 1000/461.51, where the denominator is the gas constant for water vapor and the numerator converts the gas constant to correspond to pressure in millibars instead of in Pascals. It is not clear why Dion et al. have 216.5. Water vapor deviates slightly from the ideal gas law; the careful analysis by Owens (1967, Eq. 18) would give 216.582 as the leading coefficient at a temperature of 15°C. This value is intermediate between the value used by Dion et al. and the value given by assuming water vapor to act as an ideal gas at the low concentrations of water vapor encountered in the atmosphere. The discrepancy provides some idea of the uncertainties in the refractive index.

To see the effect of water vapor, consider a temperature of 293.16°K (20°C), a relative humidity 0f 50%, a total pressure of 1013.25 mb. Using Eq. (9) below to calculate the saturation vapor pressure of water, and then the relative humidity to calculate e, the values of N given by Eq. (5) at wavelengths of 0.5, 5 and 10 μm are 273.7, 267.5 and 266.8, respectively. The contributions of water vapor were 2.7, 2.6 and 2.0, respectively; that is, 1%, 0.98% and 0.73%, respectively. For comparison, Eq. (1) gives refractivities of 273.1, 265.2 and 265.1, independent of humidity (unless P is mistakenly used instead of P_d in Eq. (1)).

A warning may be useful to the reader at this point. Several authors (such as Penndorf, 1957, and Goody, 1964, p.389) describe water vapor as reducting the refractivity. This is a potentially confusing formulation. Except in narrow spectral regions where the line structure in the water spectrum produces a small amount of anomalous refraction, adding water vapor to air increases the air's refractivity. Water vapor decreases the refractivity only if dry air is removed when water vapor is added, to keep the total pressure the same. Carefully distinguishing P_d from P will prevent confusion. When this distinction is remembered, the expression cited by Goody for the effect of water vapor gives an effect of the same sign (but with a different size) as the water vapor term in Eq. (5).

Hill et al. (1980) and Hill and Lawrence (1986) give a careful discussion of the refractivity due to water vapor. They warn that their numerical fit, used in Eq. (5), may be in error near spectral lines, and display the spectral lines of water vapor in the spectral regions of interest here. But as discussed earlier, the line structure in the spectrum of water may not cause significant errors for wide-band radiation.

When the refractive index of air must be known very precisely (as in correcting laboratory spectroscopic wavelengths), carbon dioxide and water are both treated as variable constituents of air. In this case dry CO_2-free air is distinguished from standard dry air. In addition to their variability, carbon dioxide and water vapor at atmospheric concentrations both deviate by small but noticeable amounts from the ideal behavior. Their contributions to the refractivity are discussed in detail by Owens (1967). Owens also points out that the group refractive index must be used instead of the phase refractive index for discussing the propagation of short pulses, and gives numerical expressions for the group refractive index. Although spectral details are not significant when using broad-band radiation, they may need to be taken into account when using narrow-band lasers, whether pulsed or continuous wave. Thus group refractive index or spectral structure, or both, may need to be borne in mind if 10.6 μm radiation from a CO_2 laser is used in experiments on atmospheric refraction.

For the RF region, formulas analogous to Eq. (1) are given by Atlas et al., and more detailed formulas analogous to Eq. (5) are given by Livingston (1970, pp. 60-61) and by Crane (1976, pp. 186-187).

The partial pressure e of water vapor must be known in order to use formulas such as Eq. (5). Atmospheric moisture is usually measured as relative humidity s, or by the dew-point temperature T_{dew}, or by specifying both the difference $T_{dry} - T_{wet}$ between the temperatures indicated by dry and wet bulb thermometers and the temperature T_{dry} indicated by the dry-bulb thermometer. (Relative humidity is usually denoted by U, but s (for degree of saturation) is used here to avoid confusion with the equally standard symbol for the wind speed.) Relative humidity and wet and dry bulb temperatures are readily measured in the field, by hygrometers and psychrometers, respectively; dew-point temperature is difficult to measure except in the laboratory. The partial pressure e is readily obtainable from the relative humidity s; unfortunately, there are several widely used definitions of relative humidity, so it is necessary to know which definition is being used before selecting an equation for e in terms of s. Writers in this field sometimes do not say which definition they are using; and if they do, they do not indicate the

existence of competing definitions or give the relation between their definition and the others, so detective work is often required. The most *authoritative* definition is that endorsed by the World Meteorological Organization: degree of saturation as measured by mole fraction. Let s_N denote the relative humidity defined in this manner. This is taken to be the primary definition by careful writers, such as Iribarne and Godson, 1981). Insofar as the ideal gas law is accurate, $s_N \approx e/e_s$. The degree of saturation as measured by partial pressure, $s_e = e/e_s$, is another widely used definition of relative humidity. The ideal gas law is satisfied to within about 0.3% under atmospheric conditions (see, e.g., Iribarne and Godson, 1981, Table IV-2, p.70), so even those who accept s_N as the primary definition of relative humidity often use s_e as a convenient approximation. Together, those who define relative humidity as s_e and those who use s_e as a convenient approximation to s_N make s_e the most widely used *de facto* definition of relative humidity. In terms of s_e, the desired relation is very simple: $e = s_e \cdot e_s$, where e_s is the saturation pressure of water vapor at temperature T. But a substantial number of writers define the relative humidity to be the degree of saturation as measured by mass density rather than as measured by number or by pressure. This definition (call the resulting relative humidity s_ρ) is used by Hess (1959,1979), by Rogers (1979), and by Crane (1976), for example. The relation of s_e to s_ρ is

$$s_e = \frac{e}{e_s} = \frac{s_\rho}{1 - (1 - s_\rho)\dfrac{e_s(T)}{P}} \cdot \tag{7}$$

Since e_s is always small under atmospheric conditions, $s_e \approx s_\rho$. Crane (1976, p.188) can be reinterpreted as showing that "this approximation is in error by 8% at 40°C, 2% at 20°C, and by less than 0.6% at 0°C." Since e has only a slight effect upon the refractivity, even the 8% error in s_e at 40°C produces errors of less than 0.1% error in N in all of the illustrative values given earlier for Eq. (6). Still another concept of relative humidity is s_q, the degree of saturation as measured by the specific humidity q of water vapor. (The specific humidity is the fractional mass of moist air that is contributed by the water vapor.) The impetus behind this definition of relative humidity is that the similarity laws for the atmospheric surface layer, discussed in the next subsection, give the profile of the specific humidity. The most convenient way of determining e from s_q is to use s_q to calculate s_ρ as follows,

$$s_\rho = s_q \cdot \frac{1 - \dfrac{e_s}{P}}{1 - \left(1 - \epsilon \cdot (1 + s_q) \cdot \dfrac{e_s}{P}\right)}, \tag{8}$$

and then use Eq. (7) to calculate e from s_ρ. In Eq. (8), $\epsilon \approx 0.62198$ is (as is standard in this field) the molecular weight of water divided by the molecular weight of dry air. Since the saturation vapor pressure of water is small in the atmosphere, Eq. (8) gives $s_\rho \approx s_q$, as expected.

The saturation vapor pressure is needed to use the preceeding formulas. The saturation vapor pressure is obtainable from meteorological tables, but Crane (1976, p.187) gives a convenient formula, valid to within 0.4% for temperatures between −30°C to 30°C:

$$e_s(T) \approx 6.105 \cdot \exp\left[25.22\left(\frac{T-273}{T}\right) - 5.31 \ln \frac{T}{273}\right]. \tag{9}$$

The form of this expression suggests that it is an approximate solution of the Clausius-Clapyron equation, similar to the approximate solutions discussed by Iribarne and Godson (1981, pp. 67-68).

Besides the refractivity N, it is sometimes convenient to consider the *modified refractivity* $M = N + 10^6(h/r_E)$, where h is the height of the point of interest above the surface of the Earth, and r_E is the radius of the Earth. As explained by Livingston (1970, p.106), the definition of M is a compromise between two *desiderata*: the desire for a refractivity-like quantity whose vertical derivative vanishes wherever horizontally launched rays have circular orbits concentric with the Earth (i.e., at refractive ducts), and the desire for an easily computable quantity. The first objective could be achieved exactly by a refractivity M' derived as follows. The radius of curvature of a ray in a spherically symmetric medium is

$$\rho = -\frac{1}{\frac{d\ln n}{dh} \cdot \cos\beta}, \tag{10}$$

where β is the angle of the ray's tangent above the local horizontal. (For two very different derivations of this result, see Livingston (1970, p.70 and pp. 163-164) and Born and Wolf (1980, pp. 123-124). At the launch point of an horizontally launched ray $\beta = 0$, and $\rho = r_E + h$ for a duct, so

$$\frac{d\ln n}{dh} + \frac{1}{r_E+h} = 0 \tag{11}$$

at a duct. Define a modified refractive index m' by

$$\frac{d\ln m'}{dh} = \frac{d\ln n}{dh} + \frac{1}{r_E+h} \tag{12}$$

and by requiring m' to equal the ordinary refractive index n when $h = 0$. Then the vertical derivative of m' vanishes at ducts. Equation (12) yields

$$m'(h) = n(h) \cdot \left(1 + \frac{h}{r_E}\right). \tag{13}$$

Introduce an exact modified refractivity by $M' = 10^6(m' - 1)$. Then

$$M'(h) = N(h) + 10^6 n(h) \cdot \frac{h}{r_E} = N(h) \cdot \left(1 + \frac{h}{r_E}\right) + 10^6 \frac{h}{r_E} . \qquad (14)$$

The definition of M is obtained by approximating $n \approx 1$ in the middle part of Eq. (14) or by approximating $(1 + h/r_E) \approx 1$ in the last part. Because of the compromise in the definition of M, refractive ducts occur close to altitudes where dM/dh vanishes, but not exactly at those altitudes. Since $M' = M + N \cdot (h/r_E)$, the error in the vertical derivative is

$$\frac{dM'}{dh} - \frac{dM}{dh} = \frac{N}{r_E} + \frac{dN}{dh} \cdot \frac{h}{r_E} , \qquad (15)$$

which contains a roughly constant offset of about 3×10^{-4} added to a term which vanishes at the surface. An unilluminating formula for estimating the corresponding errors in the height of the duct can be derived from Eq. (15) and the Newton-Raphson root-finding procedure; but if the height of the duct were needed to more accuracy than M could provide, it would be simpler to simply use M' instead of M.

(The foregoing approach differs from the usual approach (e.g., Livingston, 1970) in two respects. First, the present approach provides a quantity M' whose vertical derivative vanishes exactly at the ducts rather than a quantity M whose vertical derivative vanishes merely close to the heights of ducts. Second, the present approach shows the definition of the usual modidied refractivity M to involve only one approximation rather than the two approximations usually thought to be required.)

Ray bending is dominated by the vertical gradient of N (or, equivalently, of M). But the bending produced by a particular value of the gradient is scaled by the value of N; for example, the radius of curvature (10) depends upon the logarithmic derivative of N. As a result, knowing the profile of the gradient of N is not sufficient for tracing rays accurately; the N profile must also be known.

Profiles of the Intensive Variables

The profile of refractivity is determined by Eqs. (1) or (5) together with the vertical profiles of temperature, pressure, and humidity.

Data from vertical arrays of closely spaced sensors of temperature, pressure, and humidity are almost never available. So in most cases it is necessary to use simple rough rules for the profiles of these quantities.

When the mean wind is sufficiently strong, the functional form of the profiles in the first few tens of meters of the atmosphere can be obtained from a *similarity theory* of the near-surface atmosphere, due principally to Monin and Obukhov. The functional forms contain only a few parameters, and these can be estimated from simple measurements of wind speed, temperature, and humidity at two altitudes.

The near-surface layer is traditionally known as the *surface* layer. *Surface* is a slight misnomer, since it is necessary to exclude the thin layer adjacent to the surface where molecular viscosity and diffusion dominate over turbulence; the *surface layer* only begins above this excluded layer. The bottom of the surface layer depends slighly upon the quantity of interest; in principle, it is different for the mean wind, for the temperature, and for humidity. The top of the surface layer is quite variable. It may be

as low as 10 or 20 m on calm nights, and may rise to 100 m or more in strong winds. Panofsky and Dutton (1984, p.113) state that the surface layer typically occupies the lowest 10% of the planetary boundary layer, and discuss the factors (p. 87 and 107-113) controlling the thickness of the planetary boundary layer. Monin (1973, p. 429) gives a formula for an upper bound on the thickness of the surface layer, and cites 50 m as a typical value for this upper bound. A height of 10 or 20 m may seem inconveniently low: it is below likely sensors, and is above or in the range of heights of interesting targets. In most experiments—and certainly in operational situations—there is no alternative to using the similarity profiles above as well as in the surface layer, because arrays of meteorological sensors are usually not available. But in horizon-searching applications the extrapolation is unlikely to produce serious errors, since refractive effects are most important near the surface, and are relatively weak above the surface layer even when the surface layer is thin.

Similarity theory defines universal profiles for two classes of quantities: wind speed and conserved passive scalars. The conserved scalar associated with the temperature is the potential temperature θ, defined as $T(1000\ \text{mb}/P)^{\kappa}$, where T is the kinetic temperature, P is the pressure, and $\kappa = (c_P - c_V)/c_V$; here c_P and c_V are the specific heats at constant pressure and at constant volume, respectively. The adiabatic exponent κ is approximately 0.286 for dry air. For moist air the potential temperature should in principle be computed with the moist adiabatic exponent, although in practice good accuracy is obtained by using the dry exponent. (The potential temperature θ computed with the moist adiabatic exponent should not be confused with three other temperatures having related names: the virtual temperature, the virtual potential temperature, and the potential virtual temperature.) Equation (24) gives another convenient expression for the potential temperature. The potential temperature is conserved in the adiabatic limit. The conserved passive scalars associated with the moisture content are the specific humidity q and the mixing ratio r. Either can be used; it is traditional to use q. The quantities q and r are conserved even without the adiabatic approximation; their conservation requires only that the air parcel maintain its identity (without mixing with extraneous air) and that there be no condensation or evaporation.

Before describing the profiles predicted by similarity theory, it is necessary to define several parameters and constants. The parameters u_*, T_* and q_* are normalized vertical flux densities of horizontal momentum, heat, and specific humidity, respectively. The parameter u_* is called the friction velocity, and is non-negative because the mean wind always increases with height in the surface layer. Except when the wind is very weak, u_*^2 is approximately equal to the negative of the cross correlation between the vertical and along-wind horizontal turbulent velocity fluctuations. (These two velocity fluctuations are anti-correlated, explaining the sign.) An approximate physical interpretation of u_* is therefore as the geometric mean of the vertical and along-wind velocity fluctuations; when the vertical and horizontal fluctuations are comparable, u_* can be interpreted as approximately the RMS velocity fluctuation. In contrast to u_*, the parameters T_* and q_* can have either sign. Their detailed definitions are not needed here: see Monin (1973, p. 433) or Panofsky and Dutton (1984, p. 145,148). The foregoing parameters are dimensional; each has the units indicated by its name. Strictly speaking, each of these flux parameters varies slowly with height, but the variations must be very small in the lowest part of the planetary boundary layer, ultimately because the Coriolis and pressure gradient forces are both small there. The three flux parameters can be treated as constants in the surface layer; this gives the surface layer its distinctive simplicity, and leads to simple forms for the profiles. But simple forms apply only where the dominant eddies are much larger than surface features causing the friction; otherwise the details of the surface features would be reflected in the profiles. In the surface layer the representative linear size of the turbulent eddies grows linearly with height. The coefficient of proportionality is called *von Karman's constant*, κ. Its numerical value is made unambiguous, bypassing the difficulty of defining a representative size of the eddies, by means of Eq. (16) (see below). Empirically, von Karman's

constant falls within a narrow range of values (0.35 to 0.4) for a wide range of meteorological conditions; 0.4 is used in most studies. (Monin includes a factor of $1/\kappa$ in his definitions of T_* and q_*; this slightly simplifies the formulas for the profiles. Panofsky and Dutton do not include κ in their definitions of T_* and q_*; their definition is widely used, and is implicit in the formulas given below.) Another parameter is the Monin-Obukhov length, L. L summarizes the effect of the vertical gradient of average buoyancy on the turbulent energy; L can be positive or negative, depending on whether the buoyancy gradient drains energy from or feeds energy to the turbulent fluctuations. The single number L summarizes the entire profile of the Richardson number as a function of height within the surface layer, as discussed by Monin (1973, pp. 438-439) and Tatarskii (1971, pp. 81-82).

In this section, height will be denoted by z rather than h, for ease of comparison with the literature.

The most essential and least approximate assertion of similarity theory is the following: in the surface layer, the only dimensional variables affecting the vertical derivatives of the mean wind speed u, potential temperature θ, and specific humidity q are the normalized fluxes u_*, T_*, q_*, the buoyancy gradient parameter L, and of course the height z. Dimensional considerations then require

$$\frac{\kappa z}{u_*}\frac{\partial u}{\partial z} = \phi\left(\frac{z}{L}\right), \tag{16}$$

$$\frac{\kappa z}{T_*}\frac{\partial \theta}{\partial z} = \frac{\phi\left(\frac{z}{L}\right)}{\alpha_T\left(\frac{z}{L}\right)}, \tag{17}$$

$$\frac{\kappa z}{q_*}\frac{\partial q}{\partial z} = \frac{\phi\left(\frac{z}{L}\right)}{\alpha_q\left(\frac{z}{L}\right)}, \tag{18}$$

The functions ϕ, α_T, and α_q should be universal functions of z/L. Dimensional considerations cannot specify the placement of dimensionless parameters such as κ, nor of dimensionless functions such as α_T and α_q. The placement of κ in Eq. (16) constitutes a precise definition of its value, as mentioned earlier; its placement in Eqs. (17) and (18) is for the sake of parallelism of form, and is conventional, as was also noted earlier. The placement of κ is also motivated by physical considerations, as embodied in an older, heuristic "mixing-length" theory. As introduced here, the functions α_T and α_q merely allow ϕ to be factored out while allowing the left-hand sides to remain arbitrary functions of z/L. Actually, α_T and α_q have physical definitions (they are ratios of "exchange coefficients," again motivated by mixing-length theory: see Monin (1973, p. 439). (α_T is usually denoted α_H, where H is the flux density of heat; but the present notation provides more parallelism.)

Because u_*, T_*, q_* are approximately independent of height, the foregoing equations can be integrated approximately to yield

$$u(z) = \frac{u_*}{\kappa}\left[\ln\left(\frac{z}{z_0}\right) - \Psi_u\left(\frac{z}{L}\right)\right], \tag{19}$$

$$\theta(z) - \theta(z_{0T}) = \frac{T_*}{\alpha_{0T}\,\kappa}\left[\ln\left(\frac{z}{z_{0T}}\right) - \Psi_T\left(\frac{z}{L}\right)\right], \tag{20}$$

$$q(z) - q(z_{0q}) = \frac{q_*}{\alpha_{0q}\,\kappa}\left[\ln\left(\frac{z}{z_{0q}}\right) - \Psi_q\left(\frac{z}{L}\right)\right]. \tag{21}$$

The functions Ψ_u, Ψ_T, and Ψ_q are universal functions of z/L, and can be expressed as integrals having functions of ϕ, α_T, and α_q in the integrand. But in practice Ψ_u, Ψ_T, and Ψ_q are determined directly, empirically; the forms determined during one complete set of experiments can be used in general, because of the universal character of the functions. (The functions Ψ_T and Ψ_q actually depend upon $\alpha_{0T}(=\alpha_T(z_{0T}/L))$ and $\alpha_{0q}(=\alpha_q(z_{0q}/L))$ as well as on z/L; this dependence is automatically taken into account when Ψ_T and Ψ_q are determined empirically.) The parameters z_0, z_{0T}, and z_{0q} are the heights at which the respective upward integrations of Eqs. (16), (17), and (18) begin. If the same initial height z_0 were used for all three integrations, additional height-independent parameters would have to appear on the right sides of Eqs. (2) and (21) (Monin, 1973, p. 434). These temperature and humidity offsets arise because the surface roughness affects the profiles of passive scalars such as temperature and humidity differently than it affects the profile of the dynamical quantity u. The use of heights z_{0T} and z_{0q} different from z_0 is an equivalent way of allowing for this difference between passive scalars and active quantities.

The roughness height z_0 is related to the drag coefficient u_*^2/u^2 (Monin, 1973, p. 431), and is small compared to the height of the surface features responsible for the surface's friction on the atmosphere. It is independent of the wind as long as the friction-causing surface features are not affected by the wind, but depends upon wind speed when the surface consists of tall grass bent by the wind, or of wind-generated water waves. Estimated roughness heights for various types of surfaces have been tabulated (e.g., Panofsky and Dutton, 1984, p. 121,123).

The roughness height z_0 over the ocean ranges from 10^{-4} to 10^{-3} m; the smaller values correspond to calm open water. The roughness height z_0 over the ocean depends upon both the height and spacing of the waves, perhaps as summarized by the power spectrum of the height of the sea surface. A detailed theory giving z_0 in terms of sea state has not yet been developed, but Monin (1973, pp. 432-433) discusses the major features of the dependence; Panofsky and Dutton (1984, pp. 121-123) also discuss this dependence, but with less detail. Beaulieu (1990) has suggested a plausible method of taking sea state into account, at least provisionally. He assumes the vertical profiles above each point on the wavy surface to be those which would have occurred over a flat surface having the same instantaneous height as the wavy surface at that point. In effect, the similarity profiles are assumed to ride rigidly up and down with the waves (the profiles are assumed to relax quickly compared to the oscillation time of the major waves), and are averaged accordingly. Another way of taking waves into account is by using the displacement height, as discussed below.

The functions α_T and α_q are usually assumed to be equal. This is plausible, since potential temperature and specific humidity are both treated as passive conserved scalars in similarity theory. The assumption is widespread because of its convenience and because it is not contradicted by the available data. If α_T is assumed to equal α_q, the functions Ψ_T and Ψ_q are likewise equal. Then $\alpha_{0T} = \alpha_{0q}$, and it is reasonable to also expect $z_{0T} = z_{0q}$. Although the latter assumption is often adopted, Beaulieu (1992) presents strong evidence against it; this assumption is not used in the DREV refractive profile curve, which was used for most of the calculations described in this report.

The functions Ψ_u and Ψ_T are expected theoretically to be different for $L < 0$ and for $L \geq 0$: these cases correspond loosely to hydrostatically unstable and hydrostatically stable air, respectively. Panofsky and Dutton (1984, pp. 133-136 and 146-148) list some of the widely used expressions for these functions. For $L < 0$, Paulson's (1970) integral of the Businger-Dyer function is widely used for Ψ_u. In terms of a variable x (to be defined below),

$$\Psi_u = \ln\left[\left(\frac{1 + x^2}{2}\right)\left(\frac{1 + x}{2}\right)^2\right] - 2\arctan x + \frac{\pi}{2}, \tag{22}$$

Panofsky and Dutton take x to be $(1 - 16z/L)^{1/4}$, whereas Davidson et al. (1981) use $(1 - 15z/L)^{1/4}$. For $L \geq 0$ Panofsky and Dutton use $\Psi_u = -5z/L$, whereas Davidson et al. use $\Psi_u = -4.7z/L$. For $L < 0$, Paulson's result for ψ_T is,

$$\Psi_T = 2\ln\left[\frac{1 + x}{2}\right], \tag{23}$$

Panofsky and Dutton take x to be $(1 - 16z/L)^{1/2}$ (note the change in exponent), whereas Davidson et al. (1981) use $(1 - 9z/L)^{1/2}$. For $L \geq 0$ Panofsky and Dutton use $\Psi_T = -5z/L$ (as for Ψ_u), whereas Davidson et al. use $\Psi_T = -6.5z/L$.

Based on the derivation of the similarity profiles, they should apply only at heights much greater than either ν/u_* or the height of the friction-causing surface features. ($\nu = \mu/\rho$ is the kinematic viscosity, where μ is the dynamical viscosity and ρ is the density.) Since z_0 is much smaller than the surface features, this implies that the similarity profiles only become valid at heights much greater than z_0. The decreasing accuracy of the similarity profiles with decreasing height is illustrated schematically by Panofsky and Dutton (1984, p. 125). The applicability of the similarity profiles can be extended slightly downward by replacing z in the logarithmic term by $z - d$. The height offset d is called the displacement height. The same result can be obtained by perturbatively correcting Eq. (16), as discussed by Monin (1973, p. 431-432). These extrapolation techniques are usually only readily implentable for a neutrally stratified atmosphere (buoyancy forces the same at all heights), where the Monin-Obukhov length L becomes infinite, and only the logarithmic terms survive in Eqs. (19), (20), and (21). The above correction procedures do not appear to lead to a formulation in terms of an effective displacement when the stratification is significantly non-neutral.

The concept of the displacement height suggests two other approximate ways of allowing for the effect of ocean waves upon the refractive profiles. In both methods, the waves are regarded as frozen

(relative to the short time required for the atmosphere to adjust locally to wave-produced changes in the topography of the surface), and the displacement height is ignored. The first method starts by noting that similarity theory would ordinarily measure heights from the troughs of the waves, not from mean sea level (MSL). But the displacement height is typically 0.7 or 0.8 of the height of the surface elements, that is, 0.7 or 0.8 of the wave height, so including the displacement height would be equivalent to measuring heights from almost the tops of the waves instead of from the troughs. This argument is most valid for nearly neutrally stratified atmospheres, since—as noted above—the displacement height appears to be a useful concept only for such atmospheres. The second method was developed by Beaulieu (1992), and is not limited to nearly neutrally stratified atmospheres. This method starts by noting that a nearly horizontal ray is deflected scarcely at all as it travels from one ocean wave crest to another. So its cumulative bending should correspond approximately to a refractive profile obtained by averaging over the profiles erected on the various surface heights which occur from one crest to the next. It is plausible to weight the profile erected on each surface height by the fraction of the wavelength during which the height falls within a small band centered on that height. (This can only be approximate, since the wind field within a wave trough has to move down and up to follow the surface, and so is likely to contain laminar rolls, unlike the wind field at even a moderate distance above the wave tops.) The refractive gradient decreases rapidly with increasing distance above the surface, since it would be infinite at the surface in Monin and Obukhov's simplified model. The average is therefore dominated by the portions of the ray which lie above the crests of the waves; the portions lying over the troughs contribute much less. For nearly horizontal rays at heights not very close to the surface, the effect of the wave topography is therefore much as if altitudes were measured from the tops of the waves, as in the other method discussed in this paragraph. For nearly horizontal rays traveling just above the wave tops, the averaged profile is more reliable than this simple rule of thumb, however. Calculations based on Beaulieu's method are described later in this report, as well as in Beaulieu (1992). Its generality, plausible approximations, and plausible predictions favor Beaulieu's method over other methods. Its role is discussed further in the *Discussion and Summary* at the end of this report.

Assuming $\alpha_T = \alpha_q$, six numbers would be needed to specify the profiles. The six numbers are: z_0, z_{0T}, L, u_*/κ, $T_*/(u_*\alpha_{0T})$, and $q_*/(u_*\alpha_{0T})$. The latter two numbers are the ratios of the coefficients in Eqs. (20) and (21) to that in Eq. (19). Davidson et al. (1981, p. 2923) have proposed an iterative method of determining the parameters needed for specifying the profiles from four easily measured meteorological quantities: the wind speed, temperature, and specific humidity at a single reference height, and the air-sea temperature difference. The specific humidity is usually obtained from the relative humidity or dew-point temperature. The humidity need not be measured near the surface because it will be nearly 100% there, and the wind speed need not be measured at the surface because it is assumed to vanish there. (The similarity profile predicts the wind speed to vanish at z_0, but z_0 is below the altitudes where the similarity profile is valid.) The reference height is used as a datum, so six parameters must be determined from five measured quantities. As reformulated in terms of the six parameters listed above, this is achieved as follows. A semi-empirical relation due to Kondo (using the mean wind speed at 10 m) together with an assumed value of κ (0.35) gives both z_0 and u_*/κ, and a value (2.0×10^{-5}) is assumed for z_{0T}; at this point there are four parameters yet to be determined and four items of unused data. An assumed value (1.35) for α_{0T} combined with the reference height and temperature and humidity differences yields the remaining parameters. This technique seems to contain redundancies. The technique of Davidson et al. (1981) is used in the NPGS/NRL refractive profile code. Walmsley (1988) uses a slightly different method of achieving the same reduction to four measured meteorological parameters and a height. The weakest step in Walmsley's method is a semi-empirical relation which determines z_0 from the wind speed at the reference height; different studies have found widely different values for the coefficient in this relation, and even if the coefficient were well defined the relation applies only under long-fetch conditions. Walmsley's approach is used in DREV's refractive profile code.

The profiles predicted by similarity theory can be used to determine T, P and e at each height. This requires two-way conversions between the potential temperature θ and the kinetic temperature T, and also between the specific humidity q and the partial pressure e of water vapor.

Consider conversions between θ and T first. The definition of potential temperature together with the hydrostatic equation yield

$$\theta = T + \Gamma_{\text{moist}} \cdot (z - z_{1000\ \text{mb}}) \ , \tag{24}$$

where $z_{1000\ \text{mb}}$ is the height where the pressure is 1000 mb and Γ_{moist} is the moist adiabatic lapse rate. The moist adiabatic lapse rate is approximately given by

$$\Gamma_{\text{moist}} = \frac{\Gamma_{\text{dry}}}{1+0.87q} \ , \tag{25}$$

where Γ_{dry} is the dry adiabatic lapse rate. Hence under ordinary atmospheric conditions $\Gamma_{\text{moist}} \leq \Gamma_{\text{dry}}$, with an error of at most 4%. Γ_{dry} is about 0.00976°K/m. Since the lapse rate is inversely proportional to the specific heat at constant pressure, the lapse rate depends upon temperature; but the variations are negligible under atmospheric conditions. (In defining the potential temperature, older usage took the reference pressure to be at the surface. Modern usage avoids the variations in surface pressure by using 1000 mb instead. If the older usage were followed, the $z_{1000\ \text{mb}}$ in Eq. (2) would be replaced by zero.)

Now consider conversions between q and e. The ideal gas approximation yields

$$e \approx \frac{1}{\epsilon} P \cdot q \frac{1 + \epsilon \cdot s_N}{1 + s_N} \approx \frac{1}{0.62198} P \cdot q \frac{1 + 1.62198 s_N}{1 + s_N} \ , \tag{26}$$

where ϵ was defined below, Eq. (8). When the true relative humidity s_N varies between 0 and 1, the fraction in Eq. (16) varies between 1 and 0.811. A much simpler approximation, valid only to within 20%, is obtained by replacing this fraction by 1:

$$e \approx \frac{1}{\epsilon} P \cdot q \approx 1.608 P \cdot q \ . \tag{27}$$

A 20% error in the water vapor contribution to the refractivity may not be unacceptable, since water vapor contributes 1% or less to the refractivity (as illustrated following Eq. (6)). A 20% error in the water vapor contribution is only a 0.2% error in the total refractivity. Of course, the error would be systematic, not random.

Instead of using the profiles predicted by similarity theory to determine T, P, and e at each height, it is possible to use similarity theory directly to obtain the profile of the conserved passive scalar

associated with the refractivity. The conserved passive scalar corresponding to the refractivity N is the potential refractivity N_p, a concept due to I. Katz (p.199 in Kerr, 1951). The potential refractivity of an air parcel is the refractivity the parcel would have if brought adiabatically to a reference pressure. That is, all meteorological parameters in the expression for the refractivity are replaced by the corresponding values produced by adiabatic transformation to a reference level. (As with potential temperature, older usage took the constant pressure to be at the surface. Modern usage avoids the variations in surface pressure by using 1000 mb instead.) NOSC computes refractivity profiles by applying similarity theory to the potential refractivity.

A standard reference on similarity profiles is Panofsky and Dutton (1984). Holton (1979), pp.101-107) provides a very digestible first encounter with the subject, although he considers only near-neutral stratification, and does not discuss the profiles of temperature, humidity, or refractivity. Monin (1973) contains essential material not included in Panofsky and Dutton. Other useful supplements are: Monin and Yaglom (1965, 1971), Priestley (1959), and Tatarskii (1971, pp. 74-83). Tatarskii also discusses (pp. 74-76 and 102) effects on optical and radio propagation.

Height and Temperature Ambiguities

A convenient and widely used way of indexing atmospheric conditions is according to the air-sea temperature difference, ASTD = $T_{air} - T_{sea}$. The ASTD does not completely specify those aspects of the atmosphere relevant for refraction, but it is one of the most important specifiers. Two persons using the same temperature profile will report different values of the ASTD if they use a different pair of heights for measuring it. So the ASTD will be a useful index only if the two heights are standardized. Unfortunately, there are wide variations in practice in this respect, making it difficult to compare results obtained by different authors, even when both index their results by the ASTD. The greatest variations are in the height at which T_{air} is measured, although there are also disagreements about where to measure T_{sea}.

Consider first the measurement of T_{air}. According to Low and Hudack (1990, p. 17): "For [Ocean Weather Ships] the standard height of measurement for all meteorological variables (with the exception of winds) is specified in the database as being at the 12 m level. In a previous study, Blanc (1986) showed that the heights at which these intruments are sited can vary considerably even among Ocean Weather Ships. Low and Hudack accordingly use 12 m in their calculations, except where 10 m had to be used for purposes of comparison to some other work. Dion et al. (1989, p. 12) use 6 m, but say that weather ships typically measure T_{air} between 15 and 20 m. According to Hepfer (1992), official policy requires only that reported air temperatures be measured in an exposed location shielded from direct sunlight. Most reported air temperatures would therefore be measured at about 1.5 m above the deck, or at a similar distance above a higher floor. The heights would vary according to the size of the boat; for common aircraft carriers, a measurement height of about 13 m above mean sea level (MSL) seems representative. A height of 12 m will be assumed in the calculations described in this paper, since it is about the height at which air temperatures are likely to be measured in vessels of a size likely to be equipped with a horizon-searching infrared system. A conversion is needed when comparing calculations such as these to experiments performed using sensors mounted on small boats: an actual temperature profile or one obtained from similarity theory must be used to determine the ASTD which would have been obtained at 12 m from the ASTD measured by the small boat. No such problem occurs when the boat carries the source, and the sensor is mounted sufficiently high on a tower, however. Despite all the variations in practice just described, it would be wrong to conclude that elaborate conversions are needed even for rough comparisons between calculations or data obtained by different groups. Temperature gradients are small at all of the larger heights mentioned above. So only small discrepancies in ASTD

would be produced if the different choices of heights were simply ignored, except when comparing ASTDs determined by small boats to any of the others.

Now consider the measurement of T_{sea}. In most cases the surface temperature is nowadays read from a thermometer immersed in subsurface water which has been taken in to cool the ship's engines. But surface temperature is sometimes obtained by retrieving a bucket of water, or by throwing a thermometer overboard, especially on smaller vessels. In any case, the reported temperature is most closely related to subsurface water, not to the surface film or to the air at a roughness length or so above the water. It is sometimes claimed (see, e.g., discussions reported by Davidson et al. (1981)) that T_{sea} should refer to the surface film on the sea. This claim is implausible, both because the surface film is often broken (see, e.g., Wells (1986, p. 80)) and because the derivation of similarity theory shows that the values ascribed to the surface by the theory are really just parameters in formulas which become applicable only at some height above the surface. The air temperature at a height of one or several roughness lengths has a better claim to be used as T_{sea} in calculating the ASTD, since the ASTD is of interest mainly as an index to the similarity profiles. Fortunately, Davidson et al. (1981) found that using the temperature of the surface film made little difference to their results, and it is likely that the other ambiguities in the surface temperature are likewise unimportant in practice.

According to the practices just described, the heights used in measuring the ASTD must be measured relative to MSL, even when ray altitudes are measured relative to the "tops" of the waves.

Winds are usually measured at a height of 19.5 m above MSL; see, for example, Donelon and Pierson (1987) and Pierson and Moskowitz (1964). However, the reader should be warned that in the literature on ocean waves the term "surface wind" often refers to the wind at a height of 10 m.

Ambiguities also occur in specifying the heights of waves. The *height* of a surface wave is traditionally defined to be the vertical distance from trough to crest (see, e.g., Bowditch, 1966), or Kinsman, 1965). This definition of height is general enough to handle any periodic wave, including the vertically unsymmetric catenary-shaped waves often encountered at sea. The usual concept of wave amplitude is not suitable for such wave shapes. For a vertically symmetric wave such as a sinusoid, the wave's height would be twice its amplitude. The wave field encountered at sea is not periodic: it is a jumble of waves of various heights at each location. This difficulty is traditionally handled by introducing the concept of the *significant height* of the waves in a wave field. The significant height is the average height of the tallest one third of the waves (see, e.g., Bowditch, 1966, p. 730). This concept was introduced as a concession to reality; the definition gives values close to those reported by mariners, who tend to overlook the smaller waves. According to Bowditch (1966, p. 730), the true average height in a wave field is about 0.64 of the significant height; and the highest waves are about 1.87 times the significant height; see also Longuet-Higgens (1952). In the literature (see, e.g., Cox and Munk, 1954, and Charnock, 1958) the significant height is traditionally denoted $H_{1/3}$, for obvious reasons.

The significant height is a plausible candidate for the wave height to be supplied as input to refractive codes: waves taller than the significant height are relatively rare and widely spaced, and will not have much effect on the average refractive field. But the use of the equivalent height in this context should be regarded as only provisional, pending further analysis. The correct weighted average wave height for use with refractive codes should be determined from the method used to allow for the effect of waves on the atmospheric profiles, such as the method of displacement lengths or the averaging method suggested by Beaulieu, both of which were described earlier. Once the appropriate weighted average has been determined, the resulting effective wave height should be expressed as a multiple of the significant height (much as the the true average height can be expressed as 0.64 of the significant height), because the

significant height is relatively easy to estimate (as indicated by the history of the concept, mentioned in the previous paragraph); the significant height is the height reported in meteorological logs, and would be the most convenient height for sailors to supply to an in-service IR system.

As noted in the previous Section, it is sometimes desirable to measure altitudes from the nominal tops of the waves. Whether or not the significant height is the wave height that should be provided to the refractive codes, the significant height seems suitable for defining the tops of the waves, since it is easily estimated.

This discussion has a moral: there are abundant opportunities for misunderstandings about heights and ASTDs. Besides variations in practice from one research group to the next, even a single research and design group will be tempted to measure heights from a variety of reference levels, and to measure air temperatures at a variety of heights. Sensor and target heights are most conveniently measured from the water line; end-users will certainly assume that to be the intended reference level. Heights given by ray-tracing codes may be measured from the wave troughs, from MSL, or from the nominal tops of the waves. Air temperatures will be measured at much greater heights on large ships or towers than on small boats used in testing the theory.

PROGRAMS FOR COMPUTING THE REFRACTIVE PROFILE

As mentioned in the Introduction, four programs are available for computing refractive profiles. Two of the programs were provided by DREV. The third refractive profile program was provided by NOSC, San Diego, California. The fourth refractive profile program is an implementation by NRL of a model developed at the Naval Postgraduate School. All four programs obtain the refractive profile from Monin-Obukhov similarity profiles. They differ only in the choice of quantities for which Monin-Obukhov profiles are computed, and in how the parameters in the profiles are obtained from a limited amount of meteorological data. Only DREV's latest code includes the effect of wave height upon the refractive profiles.

DREV calls its refractive profile program WKDMBL (for Walmsley-Kel Research-DREV Marine Boundary Layer). The two versions of WKDMBL are usually denoted WKDMBL1 and WKDMBL2 in this paper, except in plots, where for brevity DREV1 and DREV2 or even DRV1 and DRV2 are used. WKDMBL2 is an improved version of WKDMBL1, and is described in Beaulieu (1992).

Both WKDMBL codes use Walmsley's (1988) method of determining the parameters of the similarity profiles from meteorological data, as extended to include a profile for water vapor. (Although the similarity profile for water vapor is usually in terms of specific humidity, the user provides humidity data to WKDMBL in the form of the dew-point temperature at some reference height above the surface.) The extension is described by Low and Hudack (1990) and by Beaulieu (1990). WKDMBL2 differs from WKDMBL1 by including the effect of wave action upon the time averaged refractive profile (see Beaulieu, 1992), as mentioned earlier.

DREV has compared the WKDMBL model to other models, including the NOSC code. DREV's comparisons are discussed in Low and Hudack (1990).

NOSC's refractive profile code is part of the Engineer's Refractive Effects Predictive System (EREPS), which also includes the RAYS ray tracing program. EREPS is described in Patterson et al. (1990) and in Paulus (1991). EREPS uses similarity theory to determine the profile of potential

refractivity instead of using the profiles for potential temperature and specific humidity. Unlike all the other codes discussed here, NOSC's code neglects the effect of water vapor on the refractive index.

The Naval Postgraduate School's method (Davidson et al., 1981, p. 2923) of determining the parameters needed by the Monin-Obukhov profiles for potential temperature and specific humidity were briefly described earlier. This approach has been embodied in a refractive code by NRL. It will be called the NPGS/NRL model in what follows.

None of the refractive codes will operate when the wind speed vanishes or is very small. The smallest allowed wind speed varies from code to code, and for some codes varies with ASTD. The codes refuse to consider vanishing or small wind speeds because the similarity theory profiles are valid only when wind driven turbulence dominates the dynamics: when the wind speed is small, the flow becomes laminar or is dominated by thermally driven (convective) turbulence. For this and other reasons, discussed in the Appendix, the codes are not valid under all meteorological and geographic conditions.

Sensitivity of Refractive Profiles to Parameters and Models

This section shows the application of the four refractive profile codes to determine the effects of various meteorological conditions, and the differences between the various refractive profile codes. The first subsection discusses the effect of varying the meteorology, and uses the DREV2 code for all calculations, since only the DREV2 code includes the effects of wave height. The second subsection compares the four refractive codes.

Comparisons will be based on the vertical profiles of dN/dh (that is, dN/dh as a function of height). Since profiles of N or of the radius of curvature and ρ might seem to be more natural choices, the selection of dN/dh requires some explanation.

Differences between refractive profiles show up most dramatically in profiles of the instantaneous radius of curvature of the rays, given by Eq. (10). Small differences in refractive profile can produce prominant differences in the radius of curvature because the radius of curvature can become infinite, and even changes sign as it crosses infinity. The cosine in Eq. (10) is constant to first order near $\beta = 0$, so the radius of curvature is the same for horizontal and nearly horizontal rays at a given height. Since the horizon-search problem emphasizes nearly horizontal rays, it might seem tempting to base comparisons on vertical profiles of the instantaneous radius of curvature of horizontal and nearly horizontal rays. But the bottom-line effects on refraction on horizon-searching depend upon the curvature, not on the radius of curvature. If the curvature were zero, the propagation would be straight-line propagation near a curved Earth, and the simplest formulas for the MIVR would apply. The curvature rather than the radius of curvature measures the deviation from straight line propagation. If two refractive profiles lead to dramatically different profiles of the radius of curvature but to similar profiles of the curvature, they are nearly equivalent as far as horizon searching is concerned.

Equation (10) shows the instantaneous radius of curvature of a ray to be inversely proportional to the logarithmic derivative of the refractive index. The instantaneous curvature is the reciprocal of the radius of curvature, and is directly proportional to the logarithmic derivative of the refractive index. Since n is close to unity, the logarithmic derivative,

$$\frac{d\ln n}{dh} = \frac{1}{n} \cdot \frac{dn}{dh} = \frac{1}{n} \cdot \frac{dN}{dh} , \tag{28}$$

is well approximated by *dN/dh*. So the profile of *dN/dh* provides a good charcterization of the effect of a refractive profile upon horizon searching.

Effect of Meteorological Parameters

Only the WKDMBL2 (DREV2) code was used for determining the sensitivity of the refractive profiles to the meteorological parameters, because only this code considers the effects of wave heights.

For the sake of digestibility, the region of parameter space covered by the results presented below has been limited as much as possible. Air temperatures, wind speeds, and relative humidities all refer to a height of 12 m above MSL. Surface temperatures are 0°C and 20°C. ASTDs are −7°C, −0.117°C and +2.5°C; the middle value is the temperature difference at 12 m produced by the dry adiabatic lapse rate, and corresponds to an atmosphere close to neutral hydrostatic stability. Wind speeds are 4 and 20 m/s (4.86 to 38.88 knots). (Because the refractive codes use similarity theory to determine the profiles, they sometimes choke when the specified wind speed is small; the choking point varies with the ASTD.) Maximum wave heights were determined from the typical values cited by the Beaufort scale. Winds from 4 to 6 knots are classified as a light breeze, and are associated with wave heights from 1/3 to 1 m; 1 m is therefore a reasonably conservative upper bound for a wind speed of 4.86 knots (reported as 4 m/s on the plots below). Winds from 34 to 40 knots are classified as a fresh gale, and are associated with wave heights from about 3 to 4 m; 4 m is used as the maximum wave height for a 38.88 knot wind (reported as 20 m/s on the plots below). Relative humidities are 50% and 90%. The surface pressure is fixed at 1.0001 atmospheres (1013.35 mb).

Of the five parameters varied (ASTD, surface temperature, relative humidity, wind speed, and wave height), the ASTD has by far the largest effect on the refractive profiles. The dominance of the ASTD is intuitively understandable, in the light of the discussion in the introductory overview. The effects of all the other parameters are therefore presented separately for each value of the ASTD. The three parameters other than ASTD and wave height are varied one at a time, so each comparison shows the profile for a modified atmosphere together with that of a fixed reference atmosphere (surface temperature = 20°C, relative humidity = 90%, wind speed = 4 m/s, wave height = 0 m). The maximum wave height must be varied in conjunction with the wind speed, as discussed above.

Figures 4, 5, and 6 show the effect of surface temperature (0°C vs 20°C) for ASTDs of −7°C, −0.117°C and +2.5°C, respectively. Part *a* of each figure shows *dN/dh* near the surface, and part *b* of each figure shows *N* over a wide range of heights. As shown by part *b* of Figs. 4, 5, and 6, the principal effect of changing the surface temperature is to add a height-independent constant to the refractivity. Changes to the vertical gradient of the refractivity are barely discernible except for ASTD = −0.117°C (nearly neutral hydrostatic stability), and are confined to very low altitudes. The corresponding ray traces show that these low altitudes are not visited by relevant rays when the ASTD is positive, and are visited only by the lower-mirage rays to very low targets when the ASTD is strongly negative. When the atmospheric hydrostatic stability is nearly neutral (weakly negative ASTD), the change in the refractive gradient is largest, extends to somewhat greater heights, and relevant rays dip closer to the surface. The effect of surface temperature should therefore be significant only for weakly negative ASTD.

The effects of many of the other meteorological parameters, and the effects of switching from one refractive code to another, are usually likewise confined to a small range of heights above the surface. It should be noted here that rays which dip close to the surface are excluded from many studies of near-surface refraction. Surface-grazing rays are most subject to disturbance by waves, aerosols and turbulent

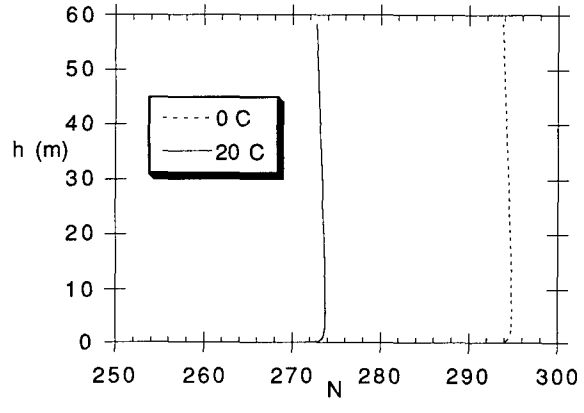

(a)

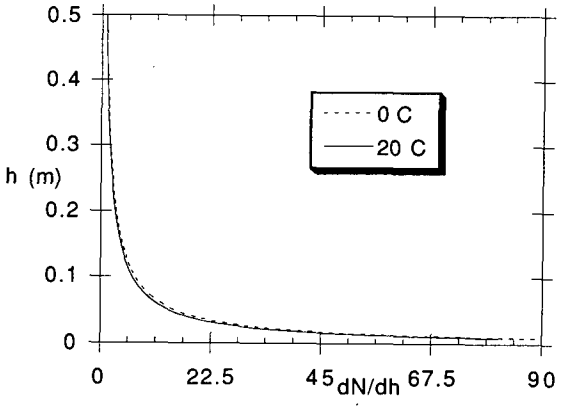

(b)

Fig. 4 — The effect of varying the temperature of the air just above the surface for ASTD = −7°C. Part (a) shows the profile of refractivity; part (b) shows the profile of the refractivity gradient.

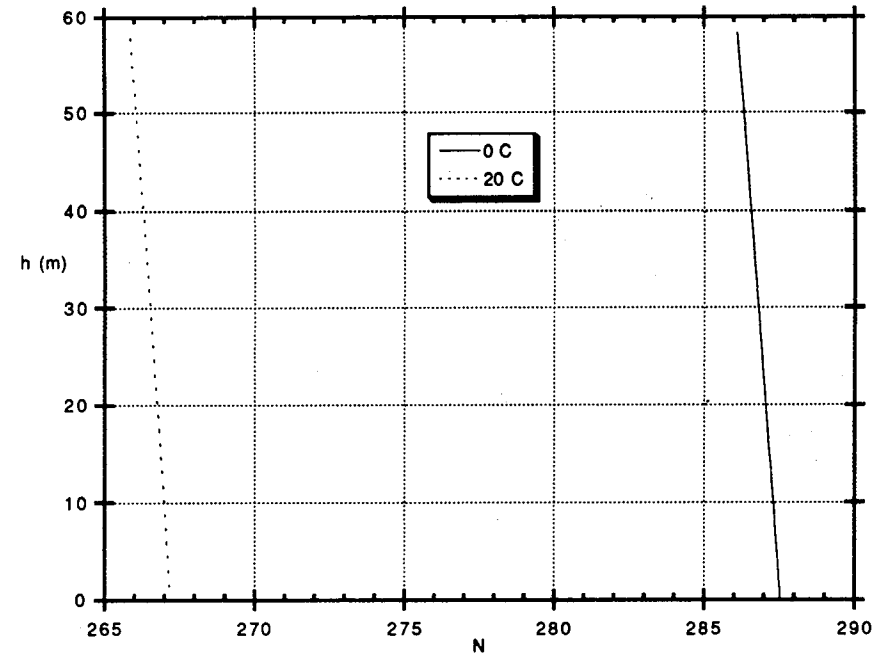

(a)

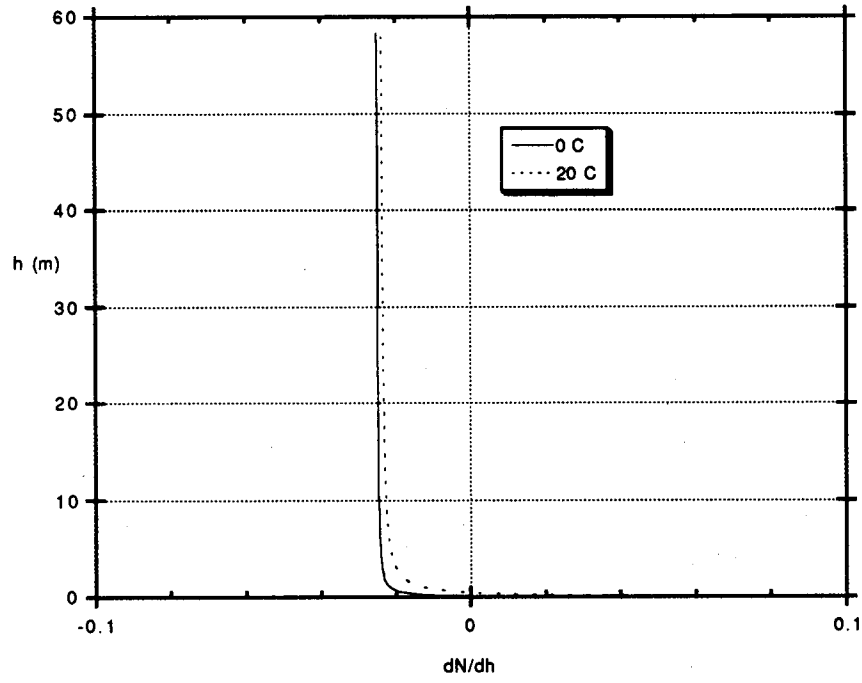

(b)

Fig. 5 — The effect of varying the temperature of the air just above the surface, for ASTD = −0.117°C. Part (a) shows the profile of refractivity, part (b) shows that of the refractivity gradient.

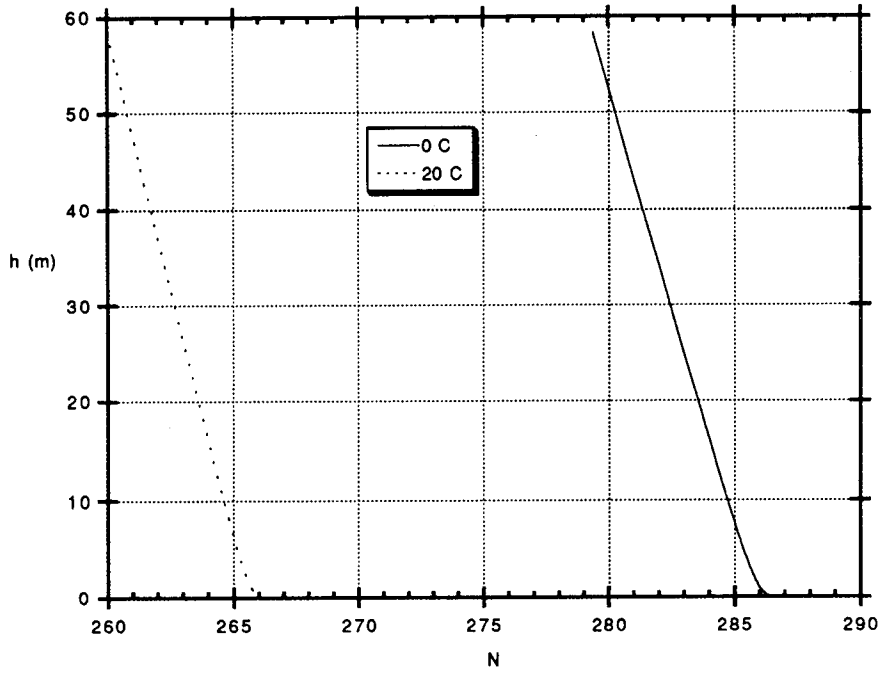

(a)

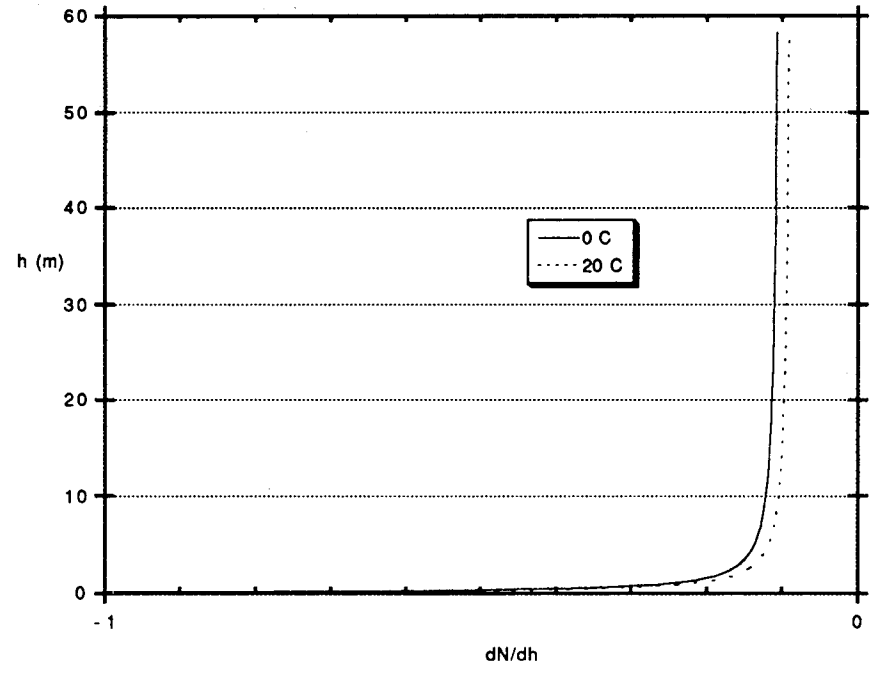

(b)

Fig. 6 — The effect of varying the temperature of the air just above the surface, for ASTD = +2.5°C. Part (a) shows the profile of refractivity, part (b) shows that of the refractivity gradient.

refraction, which are not included or are poorly modeled in many studies. In addition, the similarity profiles do not apply close to the surface. In its studies of near-surface refraction, DREV excludes rays which dip within 1 or 2 m of the surface. Near-surface differences would not show up in such studies. The ray tracing runs described later in this paper exclude rays which approach within 9 cm of the surface. The current state of the art of refractive modeling gives no criterion for choosing the cut-off height.

Figures 7, 8, and 9 show the effect of relative humidity (50% vs 90%) for the same three ASTDs, for a surface temperature of 20°C. For a strongly negative ASTD (Fig. 7) the effect is small and confined to a thin layer just above the surface; the two profiles in Fig. 7(b) are approximate horizontally-translated versions of each other. For a weakly negative ASTD (nearly neutral hydrostatic stability; Fig. 8) the refractive gradients differ significantly very close to the surface, and remain slightly different even at the largest heights considered: the gradient at 90% humidity is 3% more negative than that for 50% humidity even at 58 m, although both values are very small. For positive ASTD the gradients differ importantly over the entire range of altitudes; the gradient for 90% humidity is about 20% more negative than that for 50% humidity at all heights above about 10 m, despite the appearance of convergence with height in Fig. 9(a).

After the ASTD, the wind speed, u_{12}, is the most important parameter, since the ASTD and wind speed together determine the relative roles of wind driven turbulent eddies and of hydrostatic stability or instability in determining the profiles of passive scalars. Figures 10, 11, and 12 show the effect of wind speed (4 m/s vs 20 m/s). The effect of wind speed is large for both positive and for strongly negative ASTD, but, contrary to the pattern for the other parameters, not for weakly negative ASTD. For both positive and for strongly negative ASTD, the profiles cross (at about 10 m, which is an important range of altitudes), and have significantly different slopes throughout the relevant range of heights.

The refractive effects of the varying topography above water waves can be taken into account by Beaulieu's (1992) method, as discussed in an earlier section. In this method, the wave topography is indexed by a single quantity, the wave height. Figures 13, 14, and 15 show the effect of wave height (0 vs 1 m) for the lower wind speed (4 m/s), and Figs. 16, 17, and 18 show the corresponding effect (wave height = 0 vs 4 m) for the larger wind speed (20 m/s). As expected, 1 m waves strongly affect refractive gradients over the lowest meter, and 4 m waves strongly affect refractive gradients over the lowest 4 m. The affected regions extend high enough to be visited by rays relevant in horizon searching. For strongly negative ASTD, the effect of wave heights falls off relatively slowly with increasing altitude, becoming small (in a fractional sense) above 10 m for the smaller combination of wind speed and wave height, and above about 25 m for the larger combination of wind speed and wave height. For positive or weakly negative ASTD, the effect of averaging over the wave height becomes small at lower altitudes: at a few times the height of the waves for weakly negative ASTD, and just above the heights of the waves for positive ASTD.

Comparison of Refractive Profile Codes

The four refractive codes have been compared for a reference set of "bulk" meteorological parameters: ASTD = −7°C, −0.117°C and +2.5°C; surface temperature = 20°C; relative humidity = 90%; wind speed = 4 m/s; wave height = 0 m.

Figure 19 shows the profiles of the refractivity gradient and refractivity for an ASTD of −7°C. At high altitudes the NPGS/NRL and DREV2 refractivity profiles tend to merge, although their refractivity

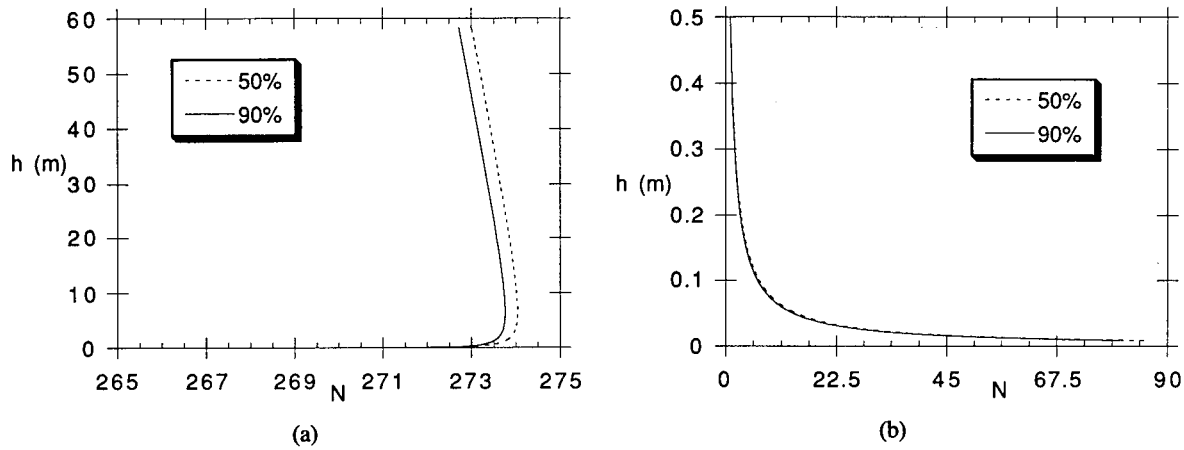

Fig. 7 — The effect of varying the relative humidity at an altitude of 12 m, for ASTD = −7°C. Part (a) shows the profile of the refractivity, part (b) shows that of the refractivity gradient.

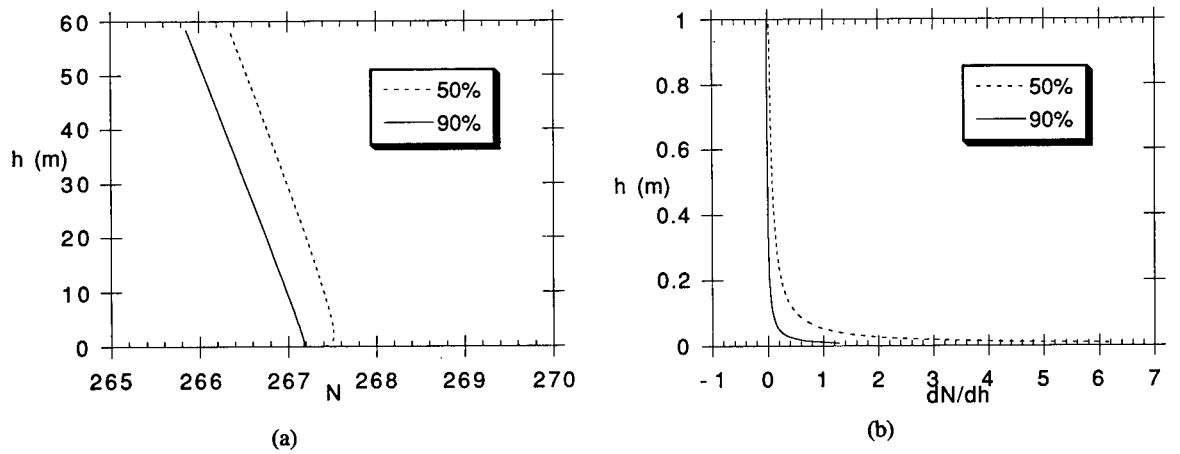

Fig. 8 — The effect of varying the relative humidity at an altitude of 12 m, for ASTD = −0.117°C. Part (a) shows the profile of the refractivity, part (b) shows that of the refractivity gradient.

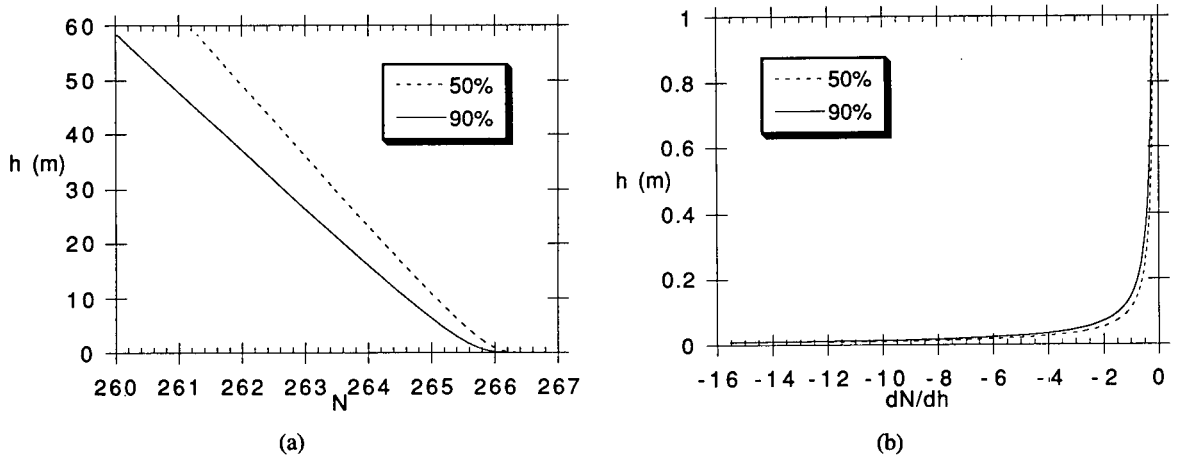

Fig. 9 — The effect of varying the relative humidity at an altitude of 12 m, for ASTD = +2.5°C. Part (a) shows the profile of the refractivity, part (b) shows that of the refractivity gradient.

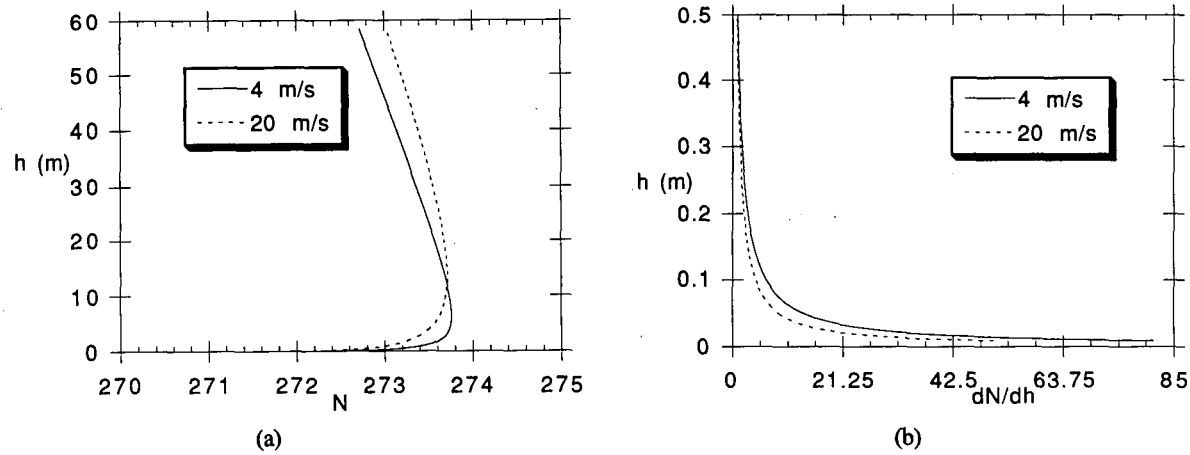

Fig. 10 — The effect of varying the relative humidity at an altitude of 12 m, for ASTD = -7°C. Part (a) shows the profile of the refractivity, part (b) shows that of the refractivity gradient.

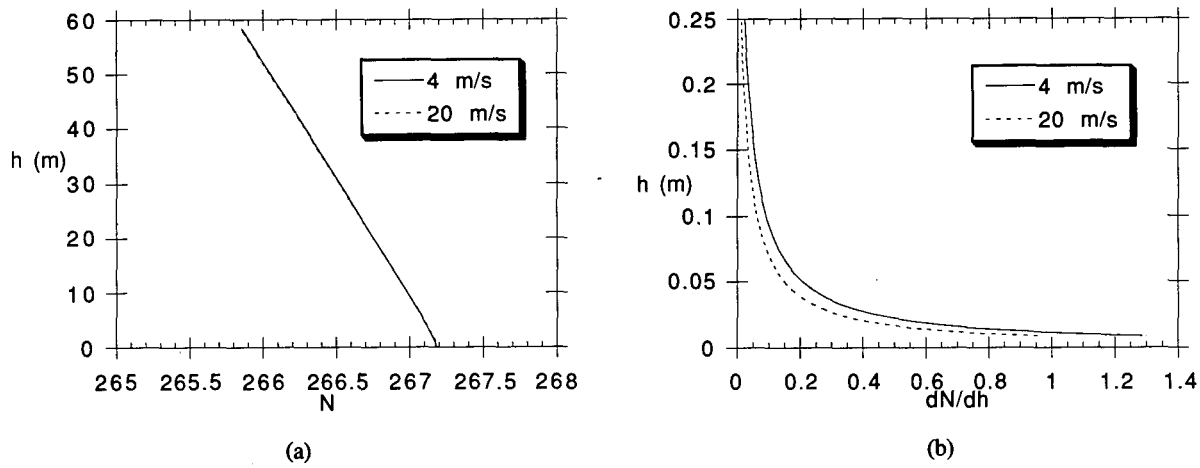

Fig. 11 — The effect of varying the wind speed for ASTD = −0.117°C. Part (a) shows the profile of the refractivity, part (b) shows that of the refractivity gradient.

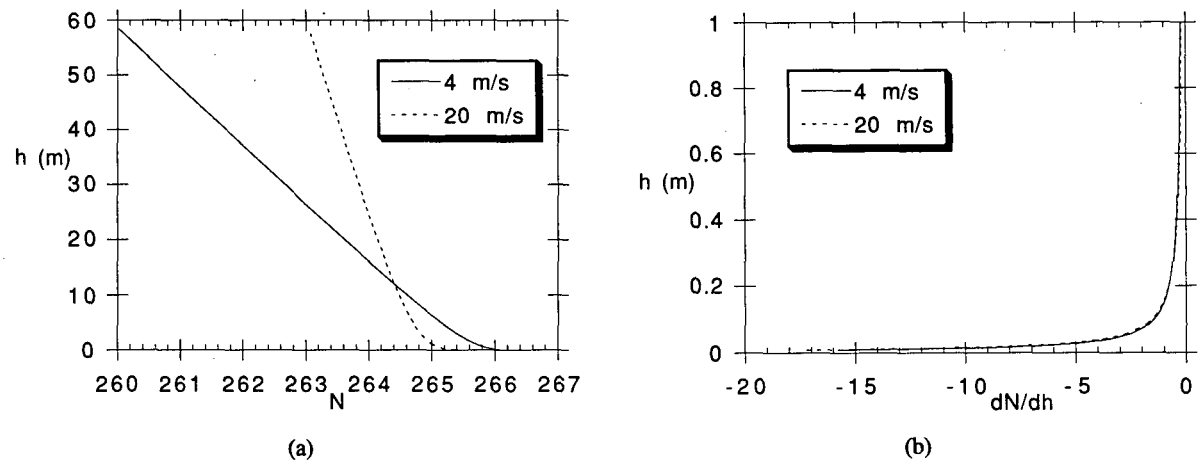

Fig. 12 — The effect of varying the wind speed, for ASTD = +2.5°C. Part (a) shows the profile of the refractivity, part (b) shows that of the refractivity gradient.

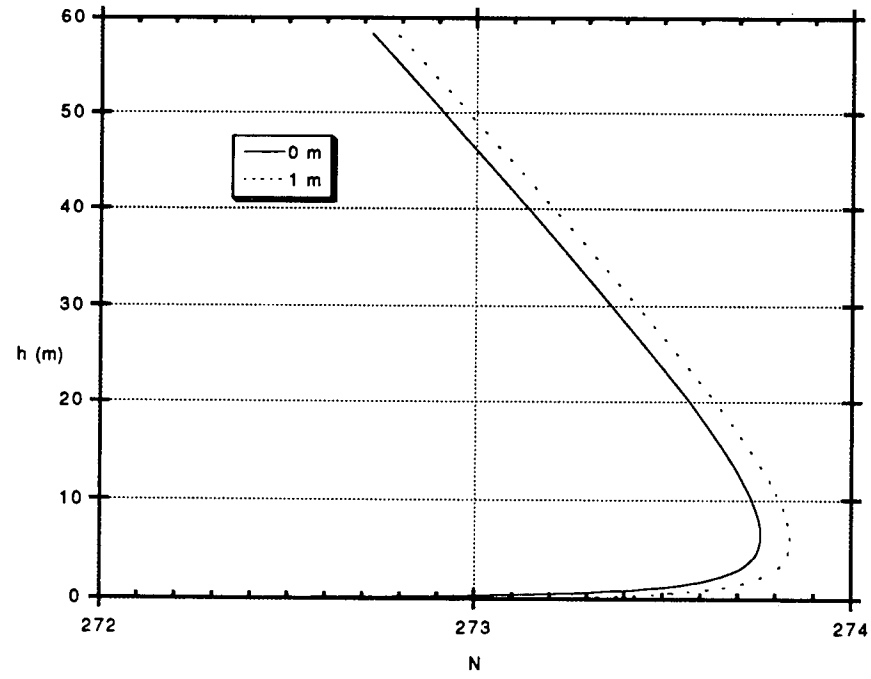

(a)

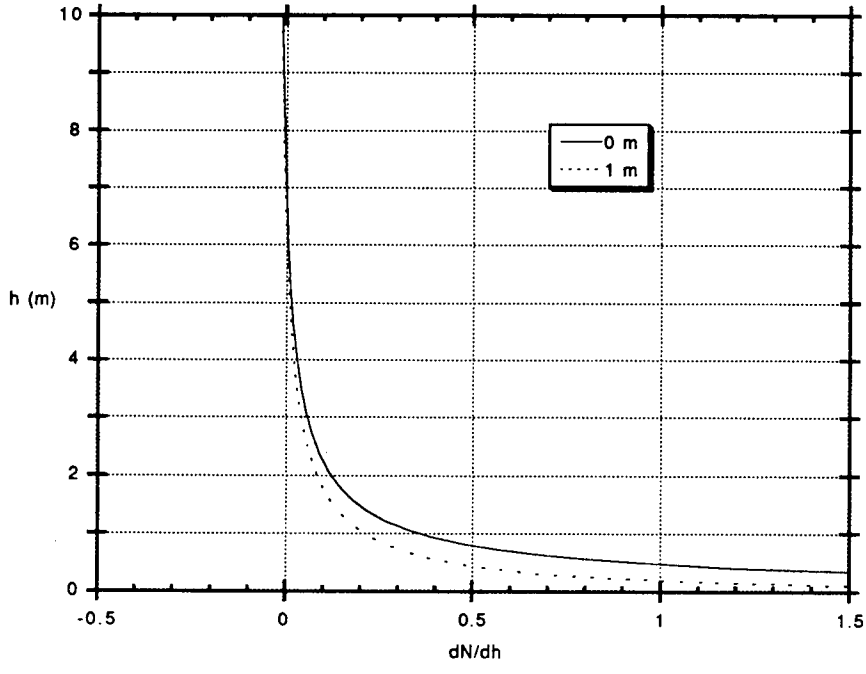

(b)

Fig. 13 — The effect of varying the wave height when the wind speed is low (4 m/s) for ASTD = −7°C. Part (a) shows the profile of the refractivity, part (b) shows that of the refractivity gradient.

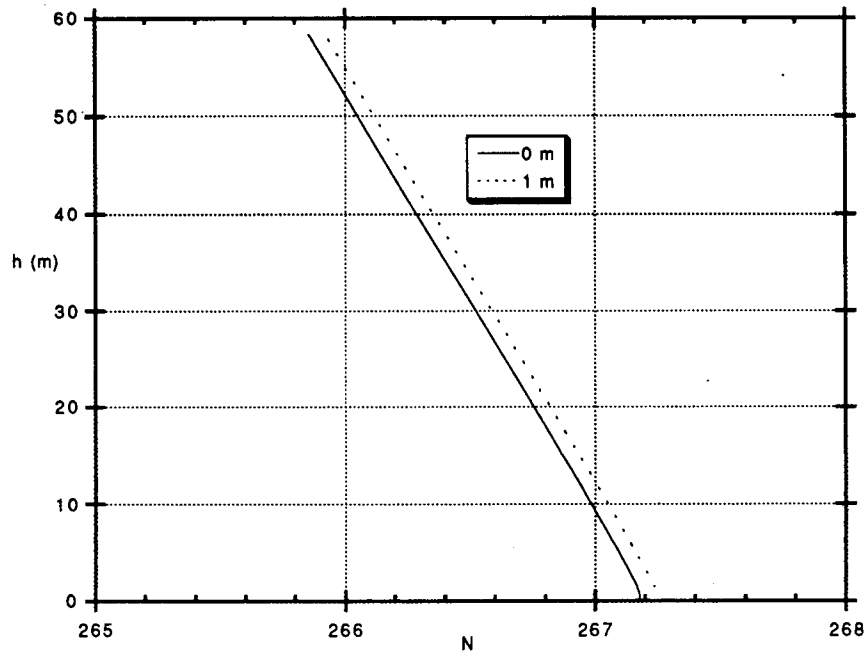

(a)

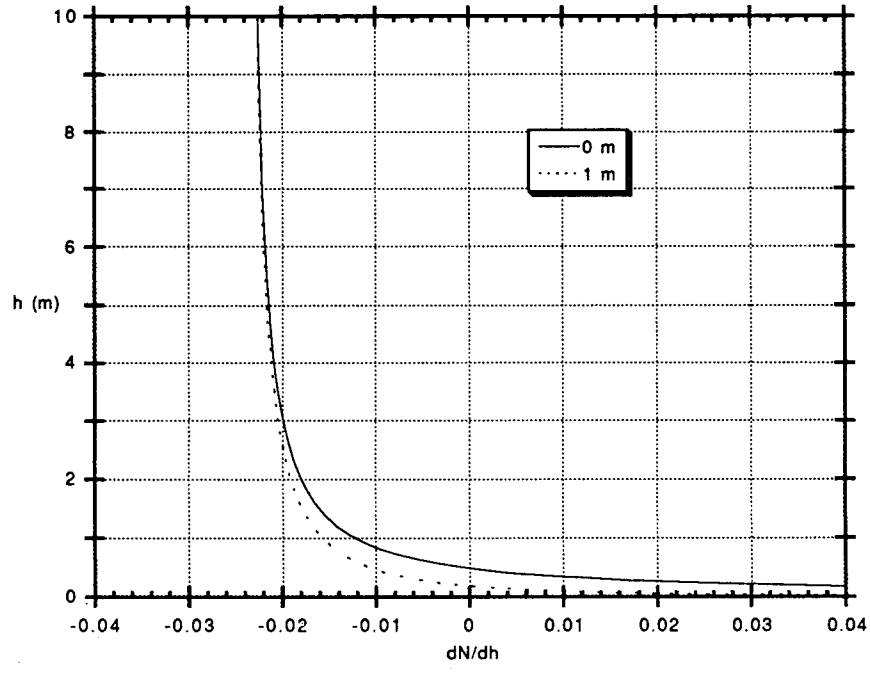

(b)

Fig. 14 — The effect of varying the wave height when the wind speed is low (4 m/s) for ASTD = −0.117°C. Part (a) shows the profile of the refractivity, part (b) shows that of the refractivity gradient.

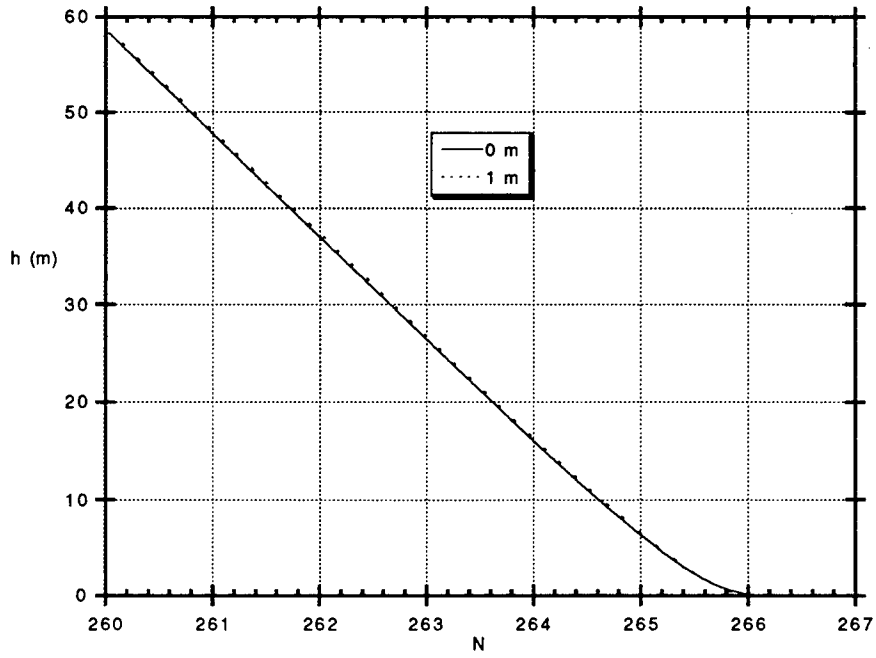

(a)

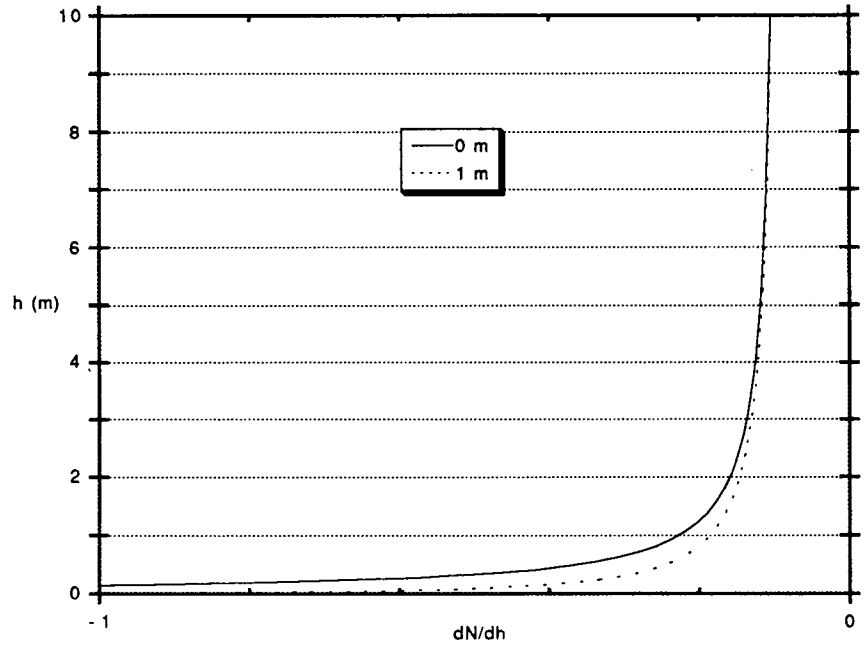

(b)

Fig. 15 — The effect of varying the wave height when the wind speed is low (4 m/s) for ASTD = +2.5°C. Part (a) shows the profile of the refractivity, part (b) shows that of the refractivity gradient.

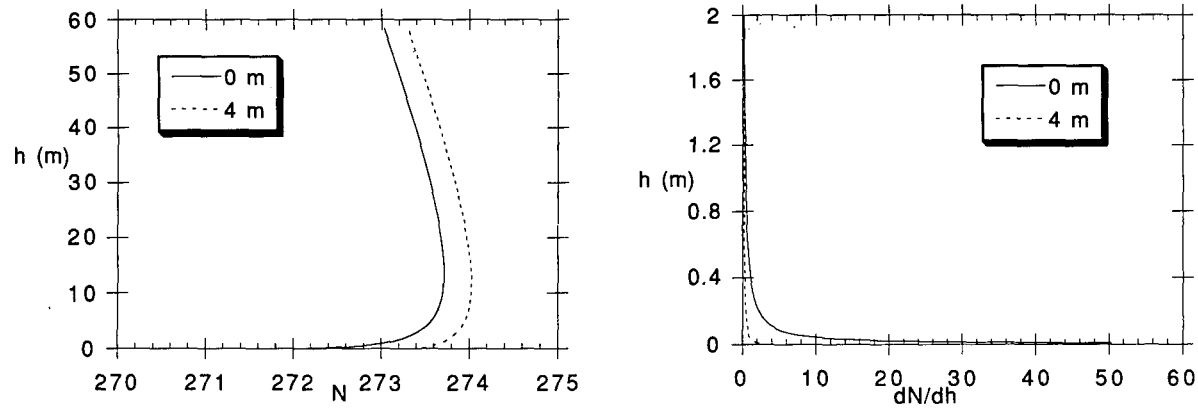

Fig. 16 — The effect of varying the wave height when the wind speed is high (20 m/s) for ASTD = −7°C. Part (a) shows the profile of the refractivity, part (b) shows that of the refractivity gradient.

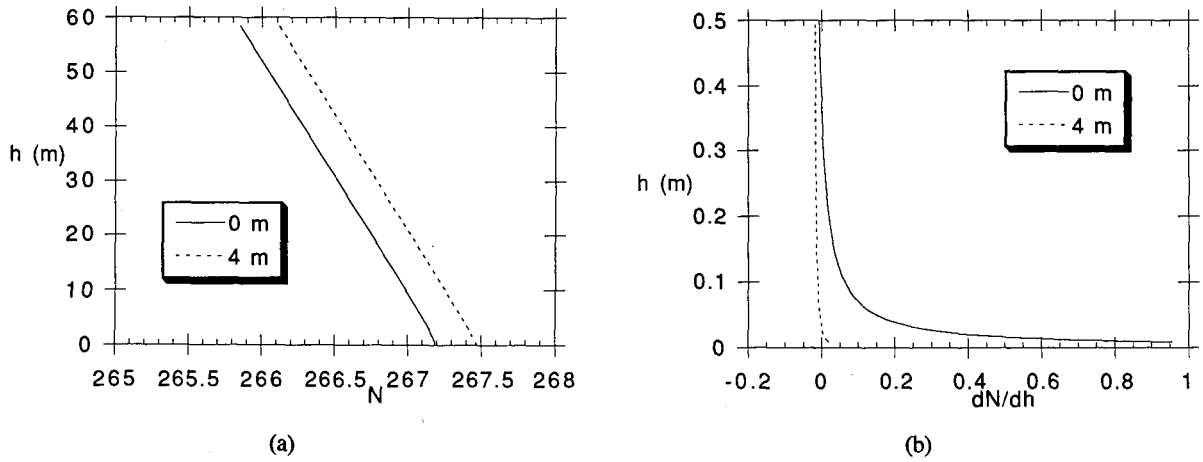

Fig. 17 — The effect of varying the wave height when the wind speed is high (20 m/s) for ASTD = −0.117°C. Part (a) shows the profile of the refractivity, part (b) shows that of the refractivity gradient.

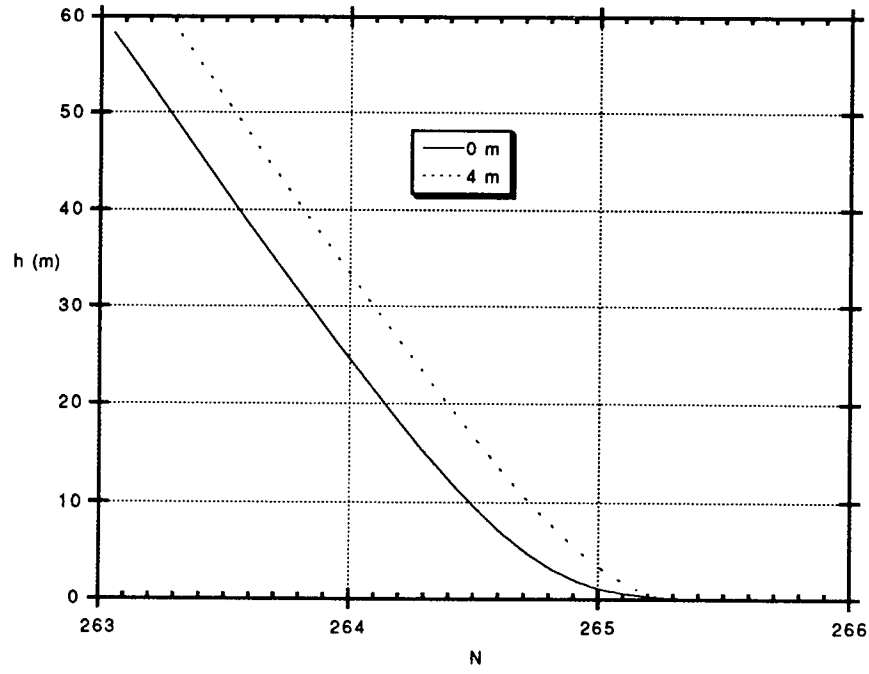

(a)

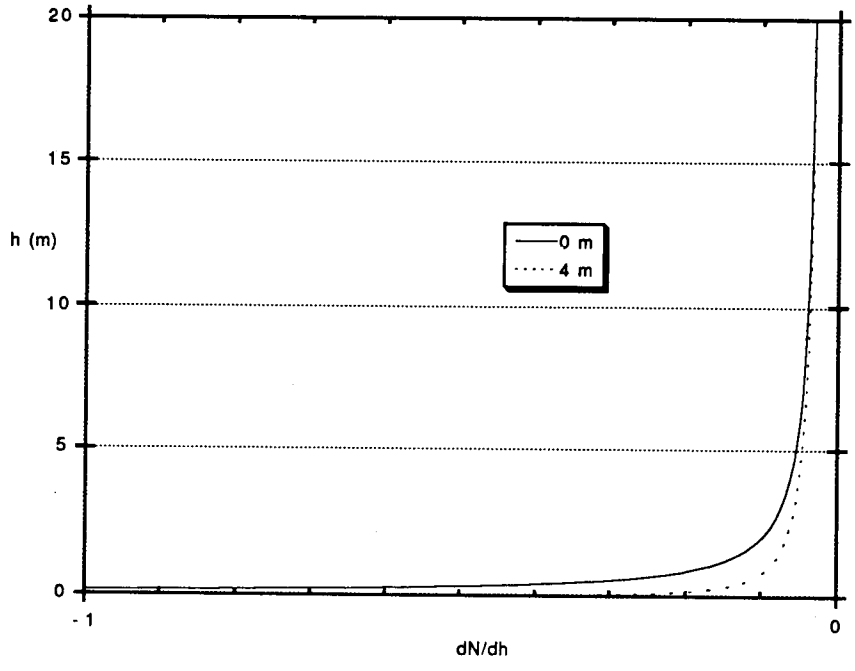

(b)

Fig. 18 — The effect of varying the wave height when the wind speed is high (20 m/s) for ASTD = +2.5°C. Part (a) shows the profile of the refractivity, part (b) shows that of the refractivity gradient.

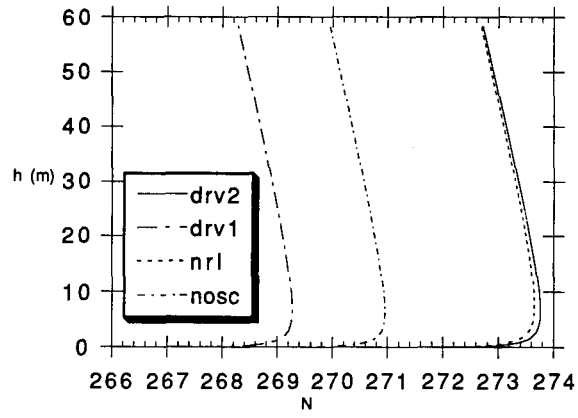

(a)

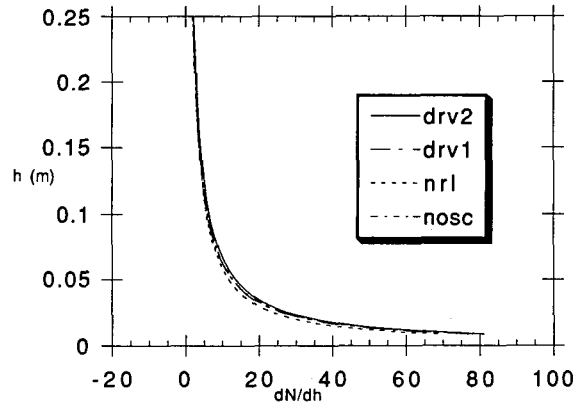

(b)

Fig. 19 — Comparison of refractivity models, for ASTD = −7°C: profiles of the refractivity (a) and refractivity gradient (b).

gradients differ slightly throughout the important range of altitudes, differing by about 4% even at 58 m. The refractivity gradients above 2 m are relatively small (less than 0.1), however. The refractivity gradients differ significantly below about 0.4 m, but rays relevant to horizon-searching do not usually dip so low.

Figure 20 shows the profiles of the refractivity gradient and refractivity for an ASTD of −0.117°C. Again the NPGS/NRL and DREV2 refractivity profiles tend to merge at high altitudes; their refractivity gradients differ by about 6% at an altitude of 58 m. The refractivity gradients above 10 cm are relatively small (less than 0.1), however. Below this altitude the relative differences in the refractivity gradients are large, but the refractivity gradients at low altitude are much smaller for this ASTD than they were for an ASTD of −7°C. Moreover, rays relevant to horizon-searching do not usually enter this low altitude region.

For both of the negative ASTD values just discussed, the refractivity gradient is positive at low altitudes, and becomes small and negative at high altitudes. For an ASTD of +2.5°C, the refractivity gradient is negative at all altitudes. Figure 21 shows the profiles of the refractivity gradient and refractivity for an ASTD of +2.5°C. The NPGS/NRL and DREV2 refractivity profiles are nearly indistinguishable at all important altitudes for this ASTD. The refractivity gradients differ only by about 0.4% at 58 m. The NPGS/NRL, DREV1 and DREV2 refractivity gradients are very similar to one another, but are all almost twice as large as those of NOSC over a wide range of relevant altitudes.

In summary, except for the NOSC code at an ASTD of +2.5°C, the refractive profile codes should give semi-quantitatively similar results for the horizon search problem, although the detailed quantitative predictions should differ, especially for targets at the lowest altitudes.

RAY TRACING PROGRAMS

NOSC's RAYS ray tracing program is an efficient and useful tool. It can be applied to refractive profiles produced by other codes as well as to those produced by the refractive profile portion of EREPS (as long as the refractivity is specified as the modified refractivity M—a trivial matter). But RAYS interpolates linearly between sampled points on the refractivity profile. RAYS therefore sees discontinuities in the vertical gradient of the refractivity at the sampling heights. Since the vertical gradient of the refractivity almost fully determines the refractive bending, the spurious discontinuities in the gradient reduce the accuracy of the ray tracing. They also produce kinks in the traced rays, which sometimes interfere with reading the directions and heights of rays (regardless of the rays' accuracy). NRL therefore developed a ray-tracing program in which the vertical gradient of the refractivity is always continuous. The NRL ray tracing program is called ALLRAYS. DREV has also developed a ray-tracing program, but DREV's program was not available during the runs described below.

ALLRAYS exists in two versions, ALLRAYS1 and ALLRAYS2. ALLRAYS1 obtains a continuously differentiable refractivity profile by means of piecewise parabolic fits to a sampled refractivity profile. ALLRAYS2 instead uses refractive profile programs which have been modified to provide sampled profiles of the refractivity gradient as well as sampled profiles of the refractivity; ALLRAYS2 then interpolates linearly between the samples of the refractivity gradient. Linear interpolation of the refractivity gradient is of course equivalent to quadratic interpolation of the refractivity itself.

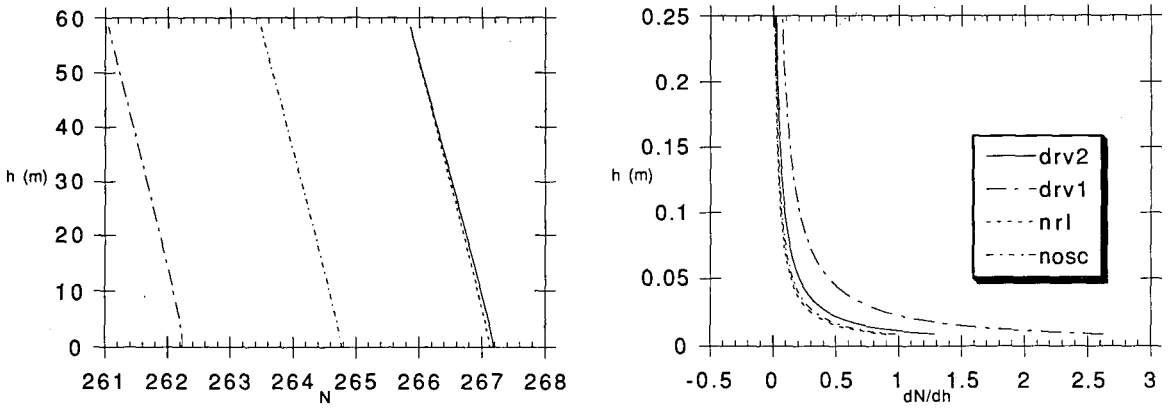

(a) (b)

Fig. 20 — Comparison of refractivity models, for ASTD = −0.117°C: profiles of the refractivity (a) and refractivity gradient (b).

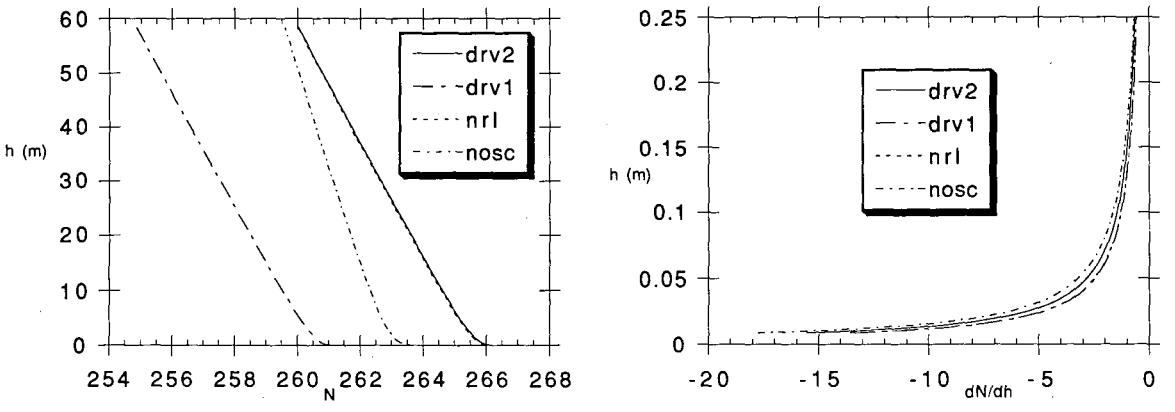

(a) (b)

Fig. 21 — Comparison of refractivity models, for ASTD = +2.5°C: profiles of the refractivity (a) and refractivity gradient (b).

Both versions of ALLRAYS are based on the system of differential equations for a ray in a spherically stratified atmosphere, as summarized by Rees et al. (1991):

$$\tan\beta = \frac{1}{r}\frac{dr}{d\theta} = \frac{d\ln r}{d\theta} \tag{29}$$

and

$$\frac{d\beta}{d\theta} = 1 + \frac{r}{n}\frac{dn}{dr} = 1 + \frac{d\ln n}{d\ln r} . \tag{30}$$

Here r and θ are the polar coordinates of a ray point; the Earth's center is the origin, and $\theta = 0$ is defined by the radial through the initial point of the ray. (The initial point is the point from which the rays are traced. Since the rays are reversible, the initial point can be located either at the source or at the sensor. It is usually most convenient to trace the rays from the sensor rather than from their physical source, but the program does not need to be told the interpretation of the initial point.) The *range* at a ray point is $r_E \cdot \theta$, where r_E is the local radius of the Earth. The range is thus the curvilinear distance along the Earth's surface between the footprints of the ray point and of the initial point. (The range should not be confused with the ray point's curvilinear distance s from the initial point as measured along the curved ray.) As before, h is the altitude above some reference sphere concentric with the Earth; in what follows, the reference surface does not always coincide with the surface of the Earth. The local direction of the ray is specified by β, which is the angle of the ray's tangent vector to the local horizontal. (The tangent vector is in the direction along which the ray is being traced, so it is opposite to the velocity vector of the physical rays if the ray is traced from the sensor.) The local horizontal is the perpendicular to the local radial. It is sometimes convenient to specify the direction of the ray at the sensor as the angle above the geometric (unrefracted) horizon. The ray traces below specify both this angle and β.

The two versions of ALLRAYS use different methods of numerically integrating the system of differential equations. In stepping along the ray, ALLRAYS1 computes the new direction β from the last part of Eq. (30), and the new height h by using Bouguer's conservation law for propagation in a spherically stratified medium,

$$nr\cos\beta = n_0 r_0 \cos\beta_0 . \tag{31}$$

(Born and Wolf, 1980, p.123; Livingston, 1970, in p. 70; and Appendix N), instead of Eq. (29). (Bouguer's law is the analog for rays of conservation of particle angular momentum in a spherically symmetric potential.) In principle, the use of Eq. (31) has the advantage of respecting the symmetries of ray propagation in a spherically stratified medium. The only sources of error when Eq. (31) is used are finite register length, and the need to estimate β and n at the new endpoint from preceeding values. Hence the use of Eq. (31) should limit the cumulative build up of errors. In practice, the calculation of h from Eq. (31) requires some fancy numerical footwork because the most significant digits on both sides of Eq. (31) cancel. This problem is solved by using a double-precision parabolic fit to $1/n\cos\beta$. ALLRAYS1 applies a simple Euler method to Eq. (30), together with automatically adapted stepsizes

determined in part by the local curvature of the ray. In contrast, ALLRAYS2 solves Eqs. (29) and (30) directly, as Rees et al. (1981) do. Like Rees et al. (1991), ALLRAYS2 uses the differential equation solver D02CBF in the NAG package of mathematical subroutines; this routine uses a variable-order, variable-stepsize Adams method. ALLRAYS1 and ALLRAYS2 give essentially identical results. ALLRAYS2 was used for the ray tracing described below.

Both RAYS and ALLRAYS presently neglect attenuation caused by the geometric divergence of the rays, as well as attenuation caused by absorption and scattering by aerosols, and attenuation caused by scattering by turbulence-induced refractive fluctuations. That is, RAYS and ALLRAYS show the trajectories of the rays, and provide only implicit and partial information on radiances. Some of this implicit information is extracted and used in the following section. The ray tracing code developed at DREV includes the attenuation caused by the geometric divergence of the rays.

TYPICAL REFRACTIVE EFFECTS

When designing sensors and algorithms it is essential to know how the apparent direction of a target varies as the target approaches. Figures 22-33 provide this information for a sensor at 20 m and targets at fixed altitudes of 15, 10, and 5 m. Figures 22-24 are for ASTD = −7°C, Figs. 25-27 are for ASTD = −2°C, Figs. 28-30 are for ASTD = −0.117°C, and Figs. 31-33 are for ASTD = +2.5°C. Since the ASTD is by far the most important parameter, the other meteorological parameters were held fixed at the reference values used in the previous section. The apparent direction of the target is displayed as the angle Λ from the geometric (straight-line) horizon; Λ is positive for directions above the straight-line horizon. The angle Λ should not be confused with the launch angle β_0, where β is the angle in the ray equations. The angles β (and, in particular, β_0) are measured relative to the local horizontal; consequently, β_0 differs from Λ by a constant which depends upon the height of the sensor:

$$\Lambda = \beta_0 - \beta_{0g} , \tag{32}$$

where β_{0g} is the launch angle for straight-line ("geometric") propagation to the horizon:

$$\beta_{0g} = \arccos\left(\frac{r_E}{r_S}\right) \approx -\sqrt{2\frac{h_S}{r_E}} , \tag{33}$$

where r_E is the radius of the Earth, r_S is the distance of the sensor from the center of the Earth, and h_S is the height of the sensor above the surface. For a sensor 20 m above the surface and an Earth radius of 6503.64 km, $\Lambda = \beta_0 + 2.4801$ milliradians.

The detailed discussion of refractive effects will be broken into the following topics: mirages; refractive ducts; the maximum apparent elevation of the target; the first visibility of the target to the sensor; the target's range when it appears to be in a particular direction; the apparent directions of targets very close to the surface (at heights much lower than those hitherto discussed); and—closely related to the previous topic—the apparent horizon, and how close the target can approach before it is seen against a background of surface clutter.

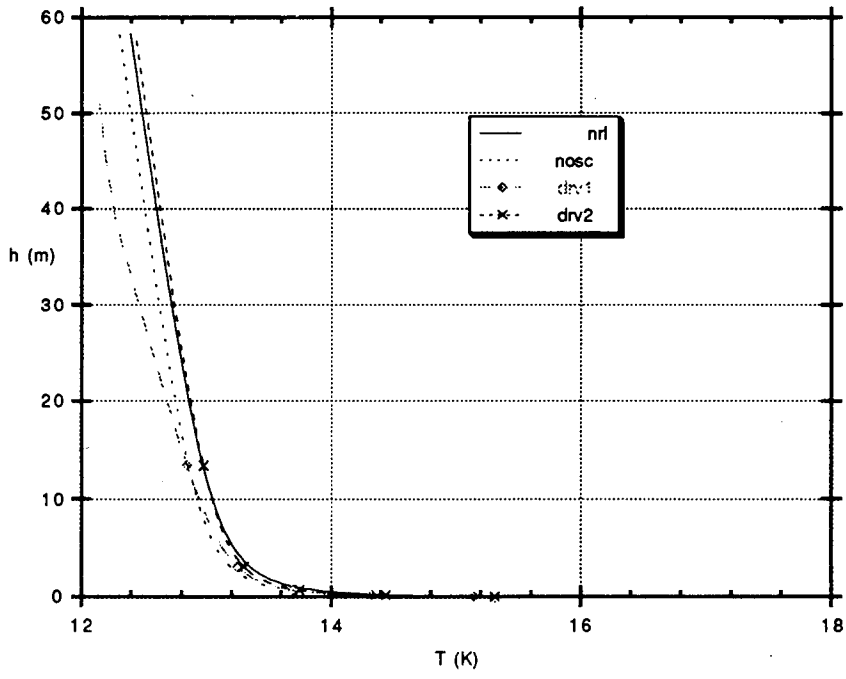

(a)

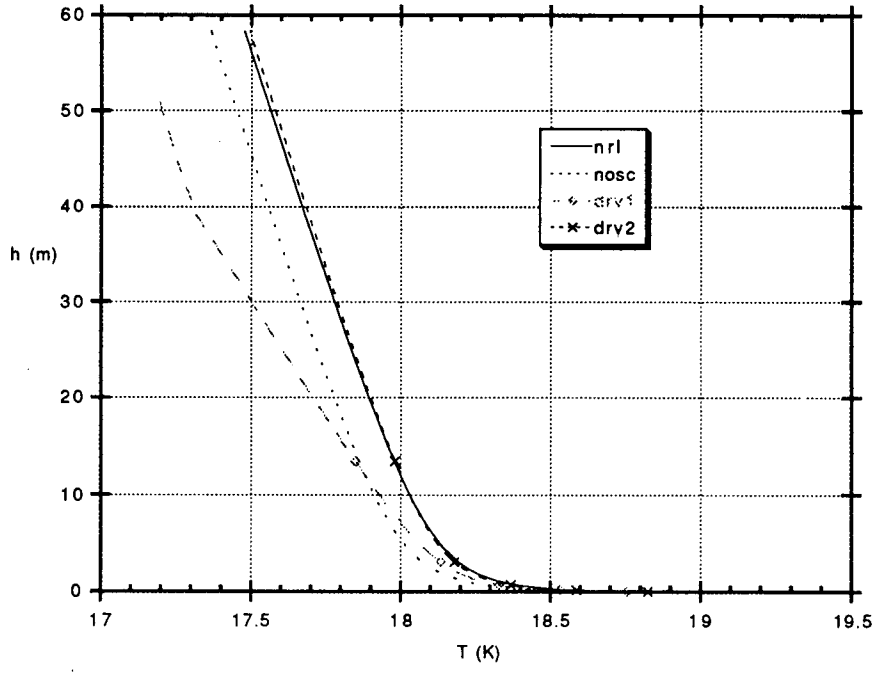

(b)

Fig. 22 — Comparison of meteorological profiles used by the four refractivity models, when provided with the same air temperature. Part (a) is for ASTD = −7°C, part (b) is for ASTD = −2°C, part (c) is for ASTD = −0.117°C, and part (d) is for ASTD = +2.5°C.

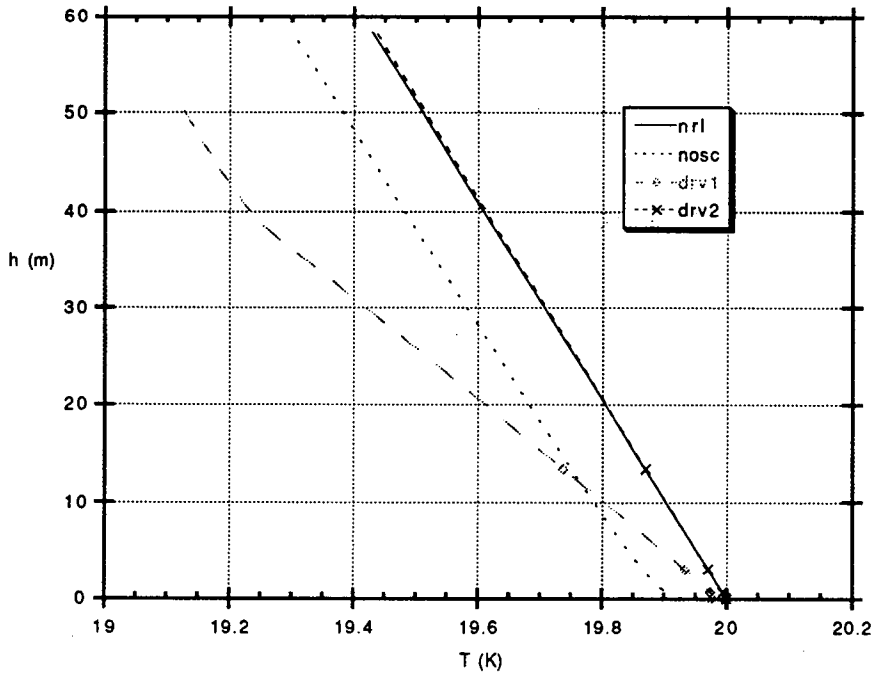

(c)

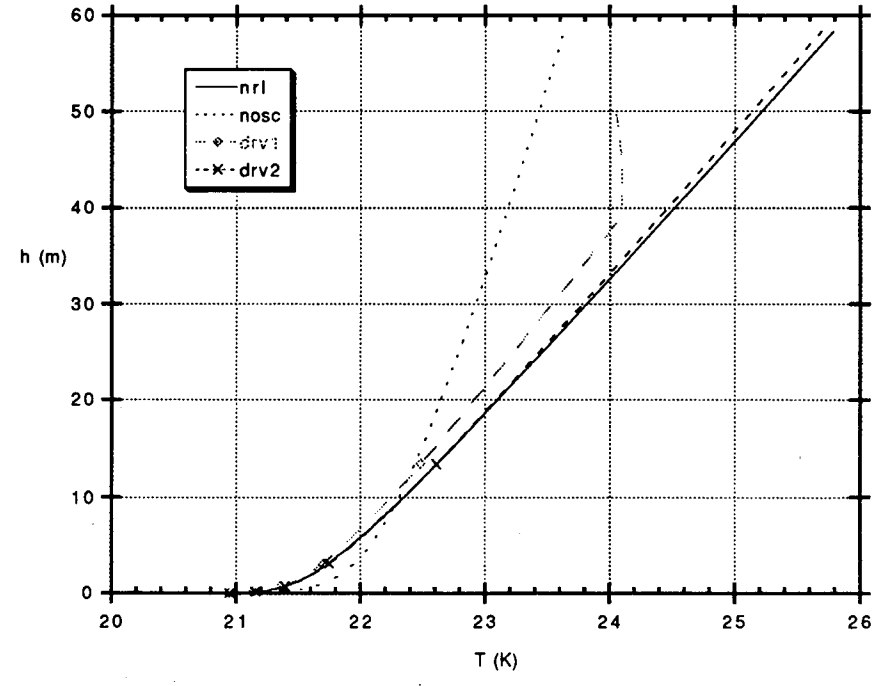

(d)

Fig. 22 (Continued) — Comparison of meteorological profiles used by the four refractivity models, when provided with the same air temperature. Part (a) is for ASTD = −7°C, part (b) is for ASTD = −2°C, part (c) is for ASTD = −0.117°C, and part (d) is for ASTD = +2.5°C.

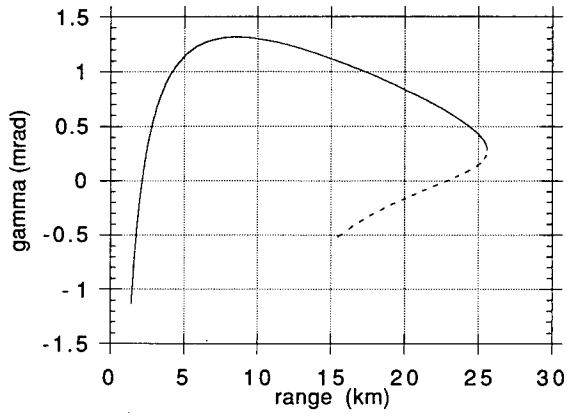

Fig. 23 — Apparent direction of the target as a function of the true along-surface range, for ASTD = −7°C. Target is 15 m above the nominal surface. Angles are relative to the straigh-line horizon.

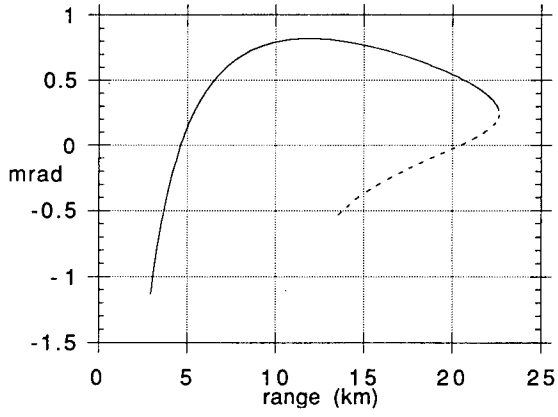

Fig. 24 — Apparent direction of the target as a function of the true along-surface range, for ASTD = −7°C. Target is 10 m above the nominal surface.

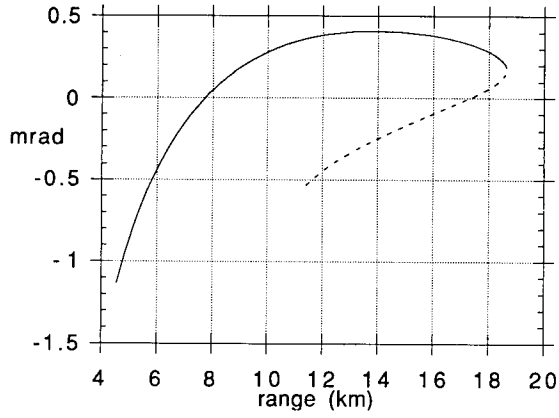

Fig. 25 — Apparent direction of the target as a function of the true along-surface range, for ASTD = −7°C. Target is 5 m above the nominal surface.

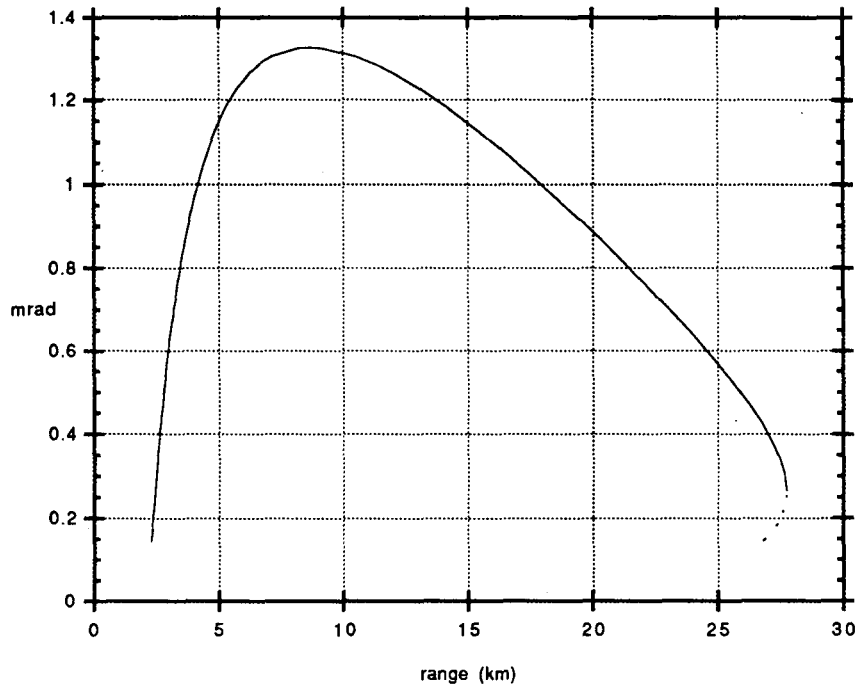

Fig. 26 — Apparent direction of the target as a function of the true along-surface range, for ASTD = −2°C. Target is 15 m above the nominal surface.

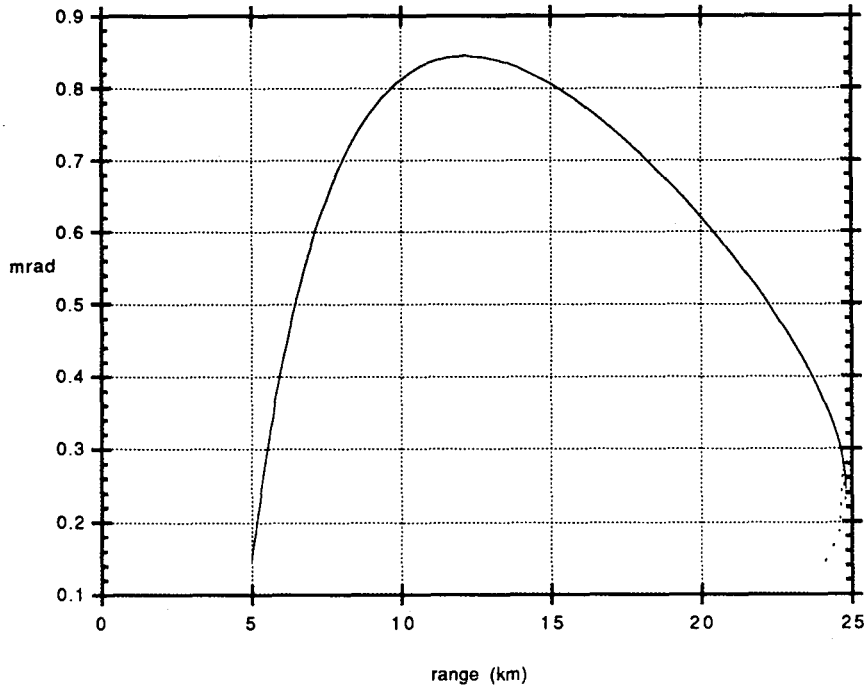

Fig. 27 — Apparent direction of the target as a function of the true along-surface range, for ASTD = −2°C. Target is 10 m above the nominal surface.

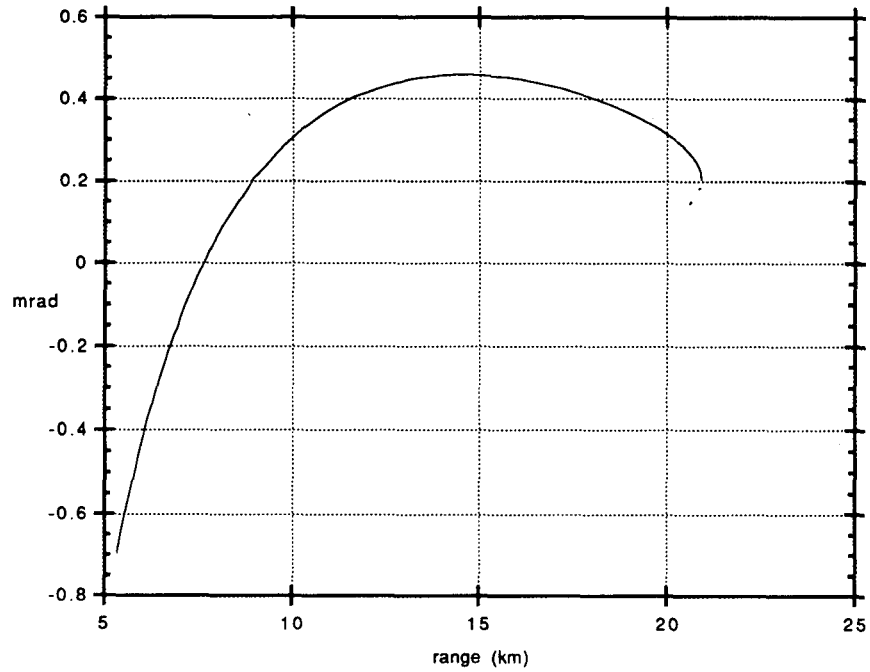

Fig. 28 — Apparent direction of the target as a function of the true along-surface range, for ASTD = −2°C. Target is 5 m above the nominal surface.

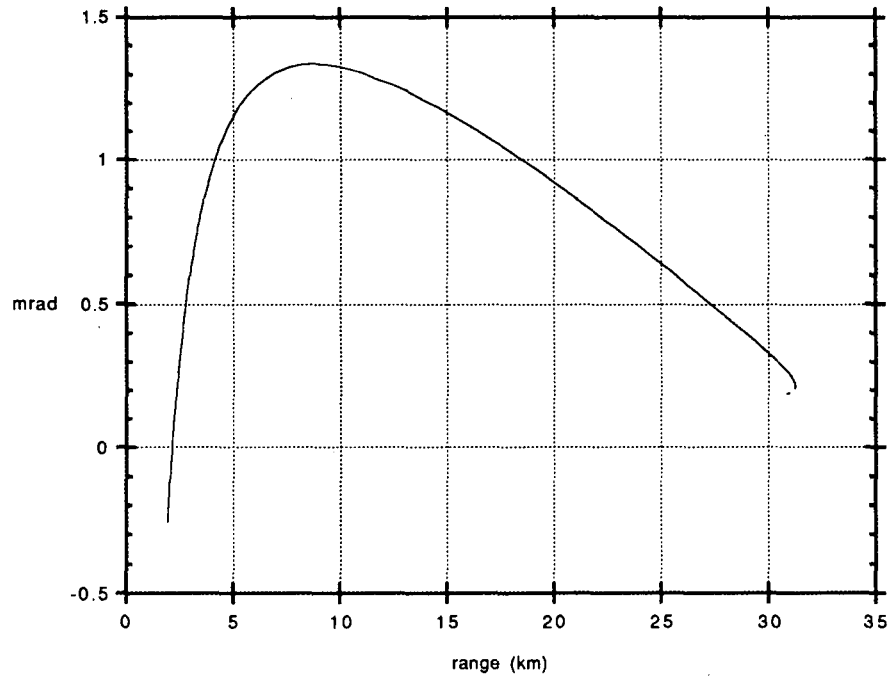

Fig. 29 — Apparent direction of the target as a function of the true along-surface range, for ASTD = −0.117°C. Target is 15 m above the nominal surface.

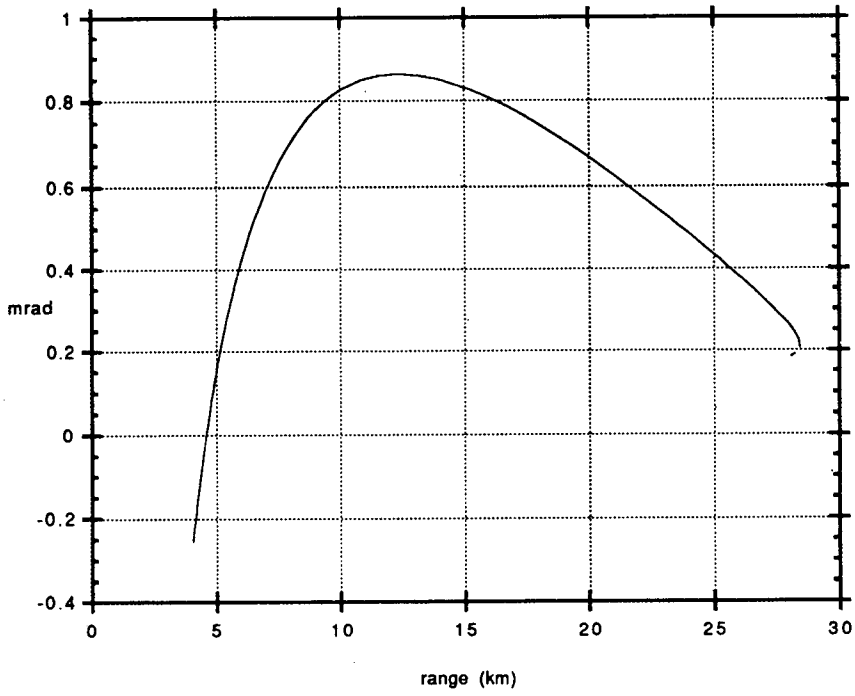

Fig. 30 — Apparent direction of the target as a function of the true along-surface range, for ASTD = −0.117°C. Target is 10 m above the nominal surface.

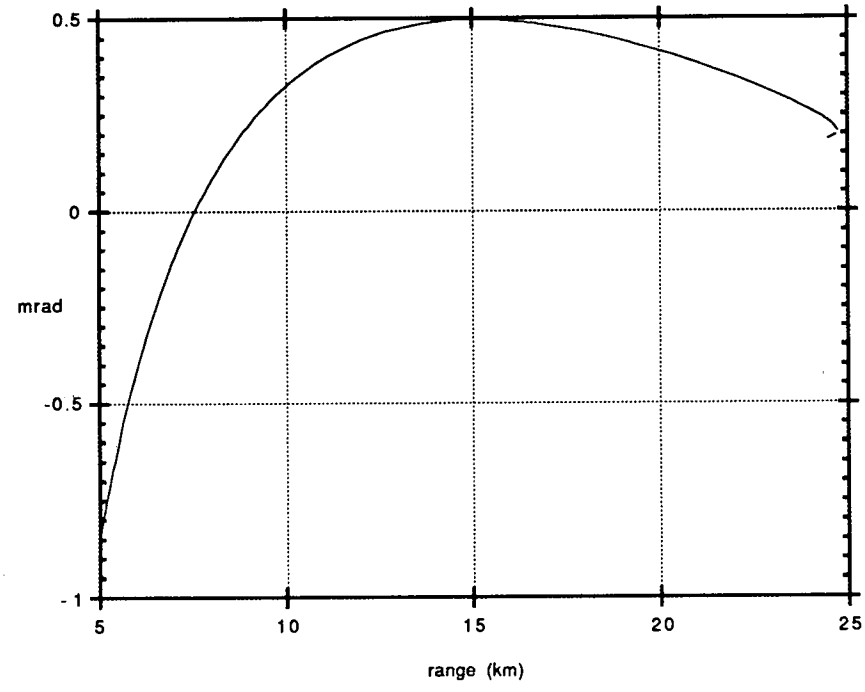

Fig. 31 — Apparent direction of the target as a function of the true along-surface range, for ASTD = −0.117°C. Target is 5 m above the nominal surface.

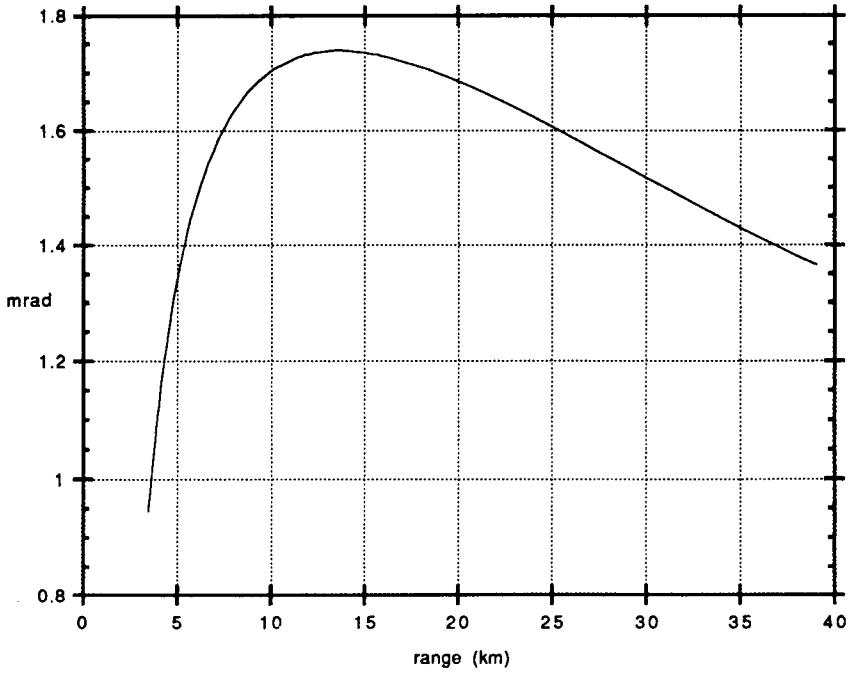

Fig. 32 — Apparent direction of the target as a function of the true along-surface range, for ASTD = +2.5°C. Target is 15 m above the nominal surface.

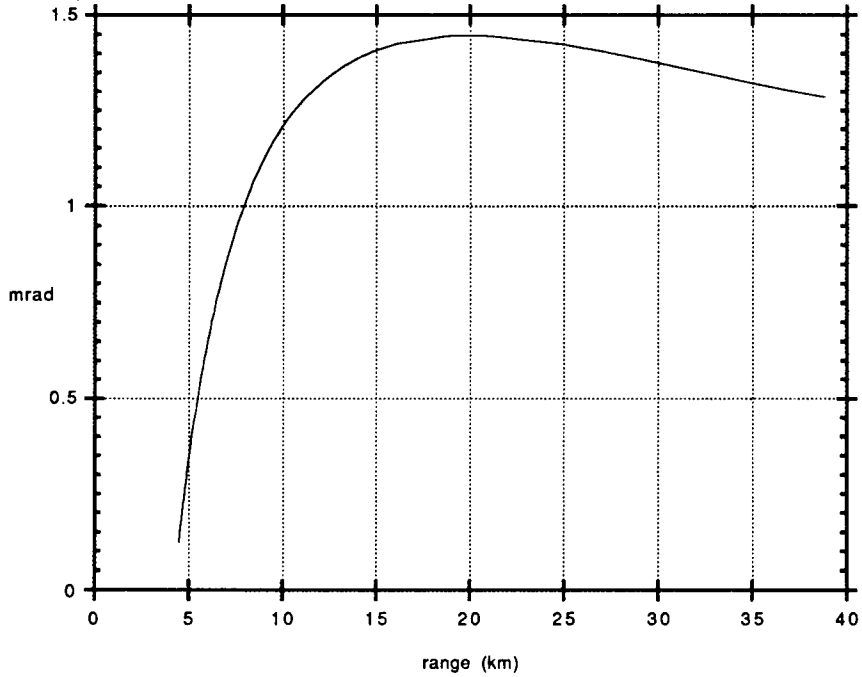

Fig. 33 — Apparent direction of the target as a function of the true along-surface range, for ASTD = +2.5°C. Target is 10 m above the nominal surface.

Mirages

As noted earlier, for negative ASTD the rays have an envelope. (The envelope of a family of rays is sometimes called a *caustic*.) When the target first becomes visible, it is consequently reached by two rays having infinitesimally different launch angles (angles at the sensor). As the target approaches further, it is reached by two rays having a finite separation in launch angle, corresponding to a mirage. The mirage is clearly shown by the beaks in the "bird's head" shapes in Figs. 22-30. The tip of the beak corresponds to the MIVR. As the target comes closer (while maintaining constant true altitude), the upper branch of the mirage rises at first, whereas the lower branch falls. The upper and lower branches of the mirage correspond to the upper and lower edges of the beak, respectively.

At the MIVR the apparent direction of the target is above the straight-line horizon, since Λ is positive at the tip of the beak. The upper branch of the mirage rises at first, but eventually falls and becomes negative. The target's apparent direction becomes strongly negative at small range because refraction becomes negligible when the target's range becomes very small, whence the apparent direction must approach the true direction, and the true direction would approach 90° below the local horizontal (which is itself 2.4801 milliradians above the straight-line horizon) if the target maintained its altitude even at zero range. The angle at zero range would be positive only if the target's height exceeded the sensor's.

The thickness of the bird's beak at a given range depicts the angular thickness of the mirage. The mirage initally grows as the target approaches, but then, in Figs. 22-30 at least, the lower branch of the mirage terminates. Unfortunately, the durations (in range) of the mirages in Figs. 22-30 may not correspond to the actual duration of the mirages. The lower branches of the mirages terminate in the figures because rays were terminated as soon as they dipped below a cut-off altitude. (The cut-off altitude was 9 cm in the present figures.) This was a rough way of incorporating the fact that attenuation by aerosols and turbulence, and clipping by waves, all become large very close to the surface. The depicted durations (in range) of the lower branches of the mirages therefore reflect a somewhat arbitrary criterion for terminating rays. This ambiguity is discussed further in the last two subsections of the present section. But the depicted durations of the mirages have at least indicative value, since 9 cm is an intuitively plausible cut-off. According to Figs. 22-30, as the ASTD increases from negative values toward zero, the mirage persists over an ever narrower range interval. Mirages do not occur for positive ASTD. A very brief mirage might occur for ASTD = 0.

The cut-off altitude, like all altitudes in the plots shown here, is measured from the same origin of vertical coordinates as was used in the refractive profile codes, that is, the origin used in specifying T_{air}, $T_{surface}$, the relative humidity, and the wind speed. Since wave height effects were absent for the refractive profiles underlying Figs. 22-33, the "surface" is close to the surface which would be obtained by flattening the actual wavy surface (i.e., by filling in the wave troughs with the water in the wave crests).

Refractive Ducts

When the ASTD is positive, the refractive model predicts a surface-based refractive duct. As discussed in connection with Fig. 1(b), the most prominent symptom of a refractive duct is the torn appearance of the bundle of rays. The tear marks a bifurcation: rays in the upper branch rise and escape to regions of negligible refraction, while those in the lower branch are fated to strike the surface. The density of rays becomes very small at the center of the tear. When the sensor is above the refractive duct, the center of the tear corresponds to a ray which asymptotically approaches (from above) a trajectory having a constant height above the surface of the Earth. The height of this asymptotically

approached circular orbit is called the "duct height," because rays launched nearly horizontally from sources below this height will be trapped, with this height as their ceiling.

The heights and apparent directions of refractive ducts are important to the designers and users of near-surface side-looking sensors. A target below a refractive duct will be invisible to a sensor situated above the duct, until the target has come so near that it intercepts rays (from the sensor) which would have struck the surface. Another system-level effect of refractive ducts concerns the apparent horizon and surface clutter. Because of the low density of rays (from the sensor) in the vicinity of the tear, the part of the surface swept by the tear will contribute little radiance to the sensor; hence both clutter and the smooth background from the surface will be negligible except from the nearer parts of the surface, where the ray density is larger. When the ASTD is positive, the surface clutter and background will therefore increase only gradually as the sensor lowers its gaze, whereas the surface contribution should increase more abruptly as a function of angle when the ASTD is negative. The apparent horizon should therefore be diffuse when the ASTD is positive.

Refractive ducts occur at altitudes where the radius of curvature of a horizontal ray equals the radius of curvature of the Earth plus the altitude of the ray. As already discussed in connection with the modified refractivity M (see *circa* Eq. (14)), this occurs near where the vertical derivative of the modified refractivity vanishes. Plots of the modified refractivity are given in Figs. 34(a), 34(b), 34(c), for ASTD = 0.5, 1.0 and 2.5°C, respectively. The figures show that only one refractive duct occurs for each suffuciently positive ASTD when the Monin-Obukhov profiles are applicable, and that the top of this duct is near the height where the modified refractivity M has a minimum. The minimum is broad and poorly defined when the ASTD is only slightly positive (indeed, there is no above-surface minimum when ASTD = 0), but becomes better defined when the ASTD becomes more strongly positive. The refractive duct will therefore have only weak optical effects for weakly positive ASTD, and will become more blatant as the ASTD increases. Figure 35 shows the heights of the refractive duct as a function of ASTD. Unless the ASTD exceeds +2.5°C, the duct height is less than 2.5 m. The apparent directions of the the refractive ducts are discussed in a later subsection.

In addition to affecting the visibility of targets flying below the duct height, refractive ducts strongly affect the visibility of targets above the duct height. A target flying above the height of the duct will not be detected at first, even if it is very bright, because of the low density of rays (from the sensor) in the tear. As the target approaches closer, it encounters a gradually increasing density of rays. Hence for positive ASTD the target's signal will emerge gradually, rather than suddenly, as it did for negative ASTD. This is discussed further in the next subsection.

This subsection ends with a warning. The Monin-Obukhov model can yield only surface-based refractive ducts. As discussed by Gossard (1982), elevated refractive ducts can also pose severe problems to ship-borne side-looking electro-optical systems in coastal waters. Gossard discusses the combinations of geography and weather which are most likely to produce elevated refractive ducts, as well as their remarkable optical effects.

Maximum Apparent Target Elevation

The point where the target has its maximum apparent elevation corresponds to the top of the bird's head in plots such as Fig. 22. Based on such data, Fig. 36 shows the maximum apparent elevation of targets flying at various altitudes, as a function of ASTD. Figure 37 shows the target's range at the moment when its image is highest.

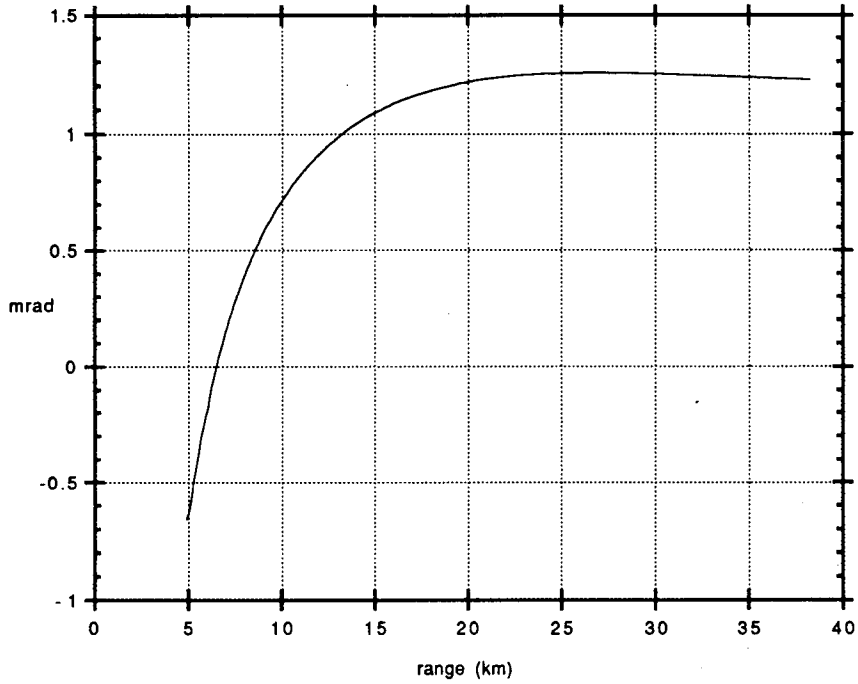

Fig. 34 — Apparent direction of the target as a function of the true along-surface range, for ASTD = +2.5°C. Target is 5 m above the nominal surface.

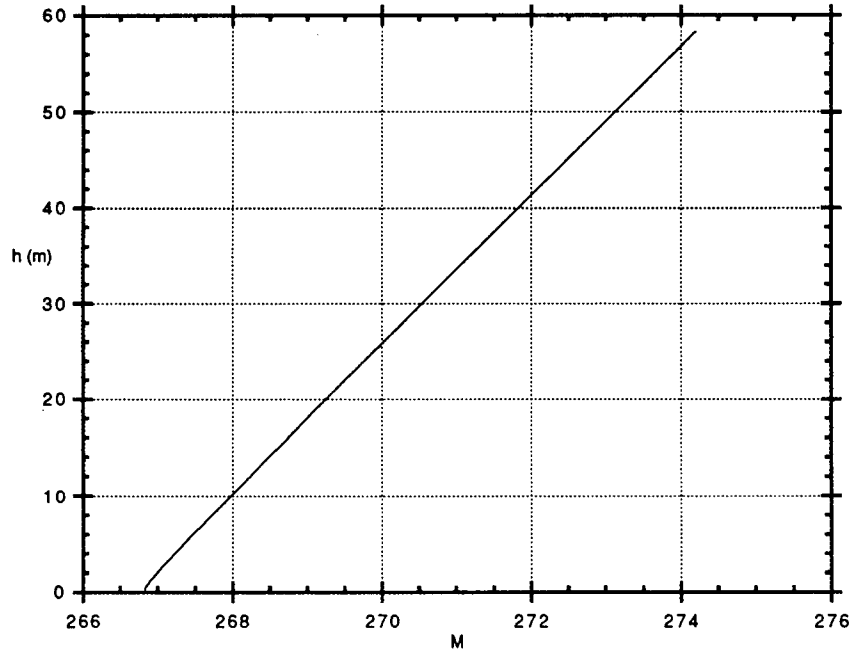

(a)

Fig. 35 — Profiles of the modified refractivity used for estimating the duct heights; (a) is for ASTD = +0.5, (b) is for ASTD = +1.0, and (c) is the ASTD = +2.5.

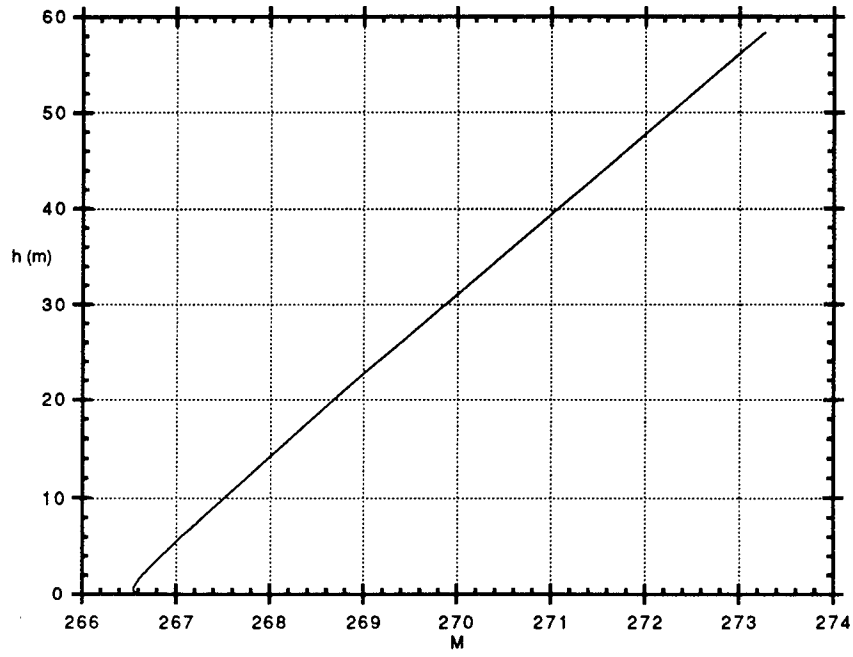

(b)

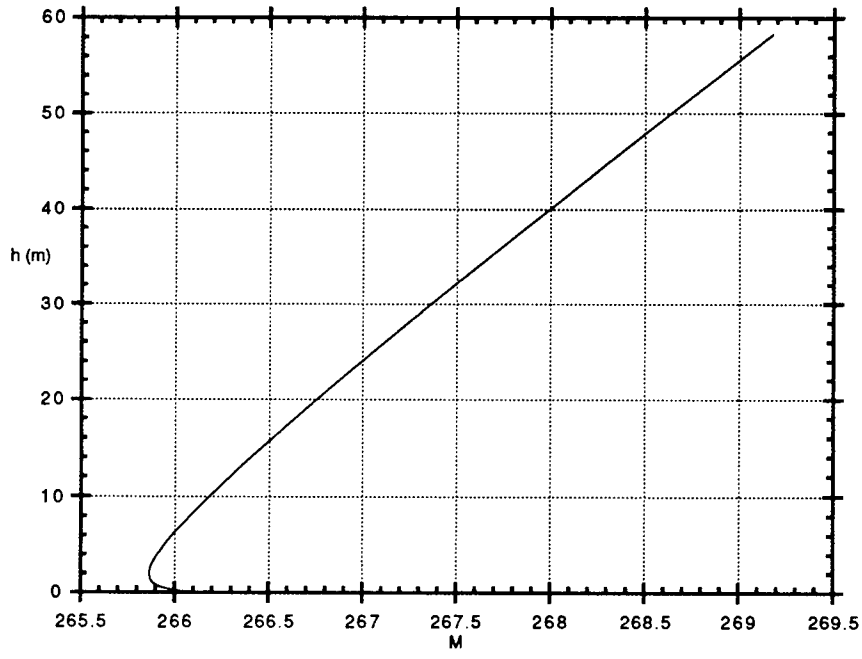

(c)

Fig. 35 (Continued) — Profiles of the modified refractivity used for estimating the duct heights; (a) is for ASTD = +0.5, (b) is for ASTD = +1.0, and (c) is the ASTD = +2.5.

The information in Figs. 36 and 37 is useful in the design of both sensor hardware and detection and tracking algorithms.

First Visibility of the Target to the Sensor

For negative ASTD the bundle of rays from the sensor has a caustic. The target first becomes geometrically visible when it encounters the caustic: no matter how bright the target is, it cannot be seen until it crosses the caustic, because no ray from the sensor intercepts the target until then. If the target were infinitely strong or the sensor were noise-free, the target would actually become visible as soon as it became geometrically visible, but for realistic targets and sensors, the caustic marks mereley the onset of the potential visibility of the target.

When the target is at any position just inside the caustic, it intercepts two rays having different launch angles at the sensor. Thus the range at which the target suddenly becomes potentially visible is also the range at which the target's image bifurcates into a two-branched mirage. The density of rays belonging to the upper branch of the mirage does not vary dramatically as a function of the target's range immediately after the target penetrates the caustic. So neither the target signal nor the path radiance will vary rapidly immediately after the target crosses the caustic. If the sensor noise and the contrast between target and background are such that the target would have been detected at practically interesting ranges in the absence of ray bending, then in the presence of ray bending the target will be detected soon after it becomes geometrically visible. Thus, to a good approximation, for negative ASTD the target will appear suddenly, as soon as it encounters the caustic.

For negative ASTD, the initial appearance of the target to the sensor has two characteristic features: it is sudden, and it occurs soon after the target crosses the caustic. Because the target becomes visible suddenly, the MIVR is well defined for given values of the target altitude, sensor quality, target strength, and atmospheric background. Because the sudden appearance of the target occurs when the target is near the caustic, for a fixed negative ASTD the caustic provides a universal approximant to the MIVRs for all reasonable combinations of sensor quality, target strength, and of atmospheric background. That is, the MIVR for a given ASTD and target altitude is essentially independent of the details of the sensor, target, and atmosphere.

These two characteristics no longer hold when the ASTD becomes positive. As discussed in the previous subsection, when the ASTD is positive the target becomes visible gradually. Since the density of rays at the target increases only gradually as the target's range decreases, the range at which the target will first be detected will depend upon the detailed characteristics of the sensor, target, and atmospheric background.

In compensation, a sensor can potentially detect a target (against a favorable background) at considerably larger ranges for positive ASTD than for negative ASTD. This will become apparent from the quantitative estimates of MIVRs, which will be discussed now.

When the ASTD is negative, the MIVR for each specific target altitude is easily read from ray trajectories such as those in Fig. 1(a): it corresponds to the envelope of the bundle of rays. On the plots of apparent direction (such as Fig. 22) the MIVR corresponds to the tip of the beak on the "bird's head." For example, the MIVR is 25.6 km for a target at 15 m altitude when the ASTD is -7. Figure 38 shows a plot of the MIVRs for targets flying at constant heights of 15, 10 and 5 m, as a function of ASTD.

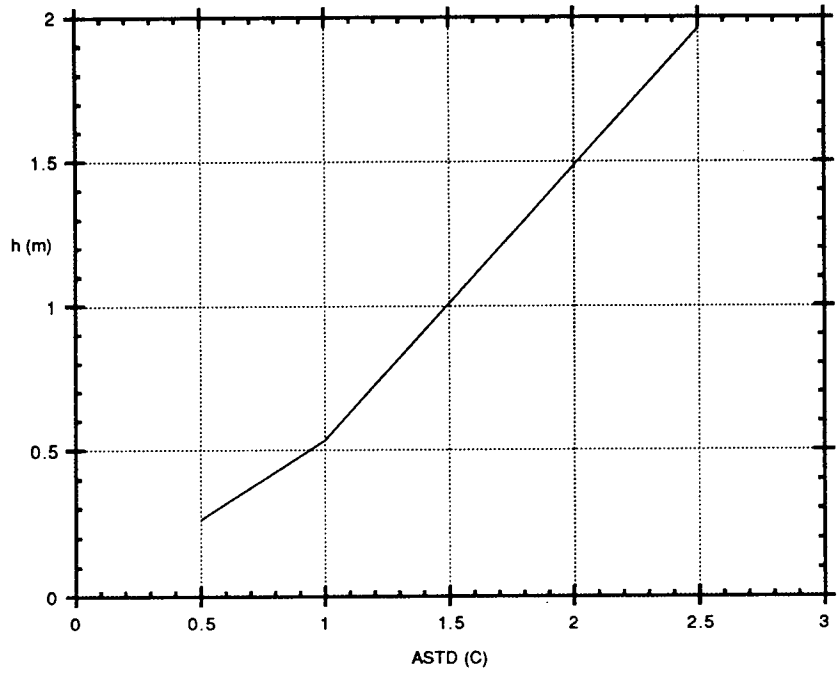

Fig. 36 — Heights of tops of surface-based refractive ducts

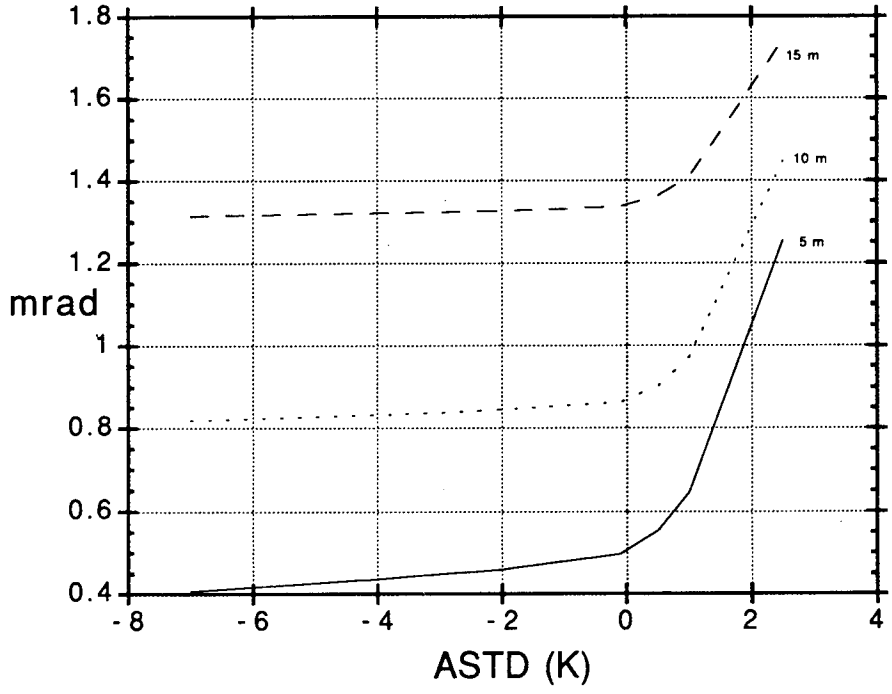

Fig. 37 — Angle of maximum apparent elevation, measured relative to the straight-line horizon

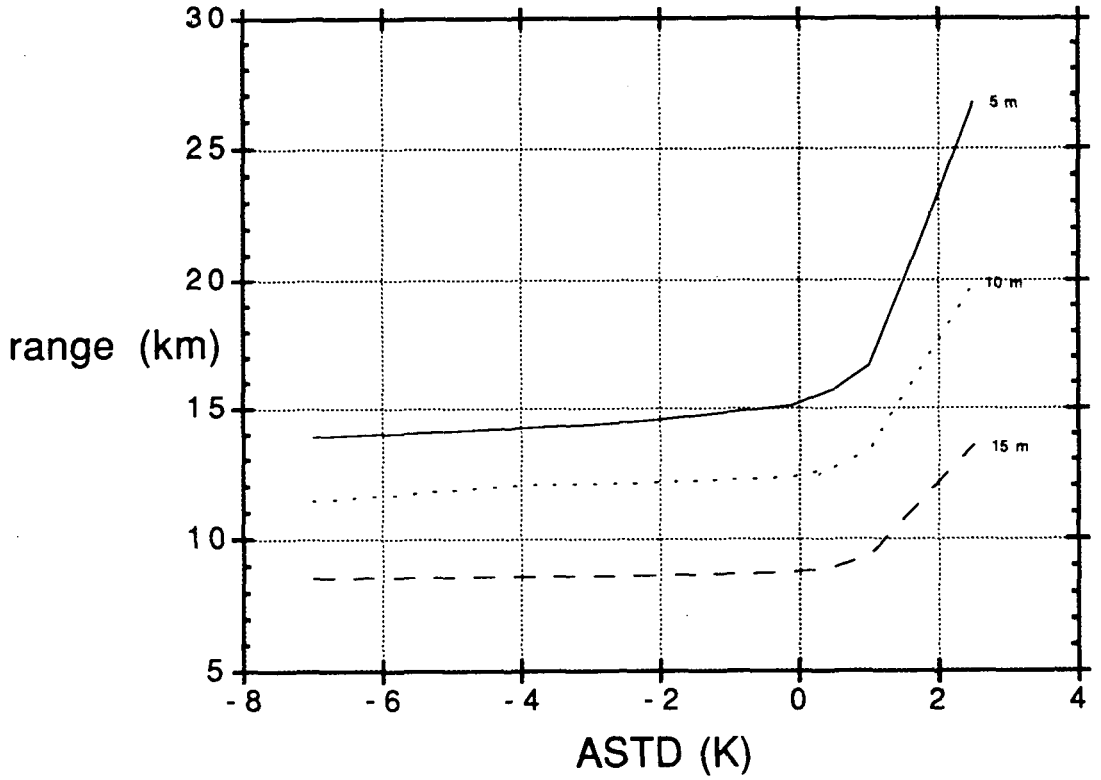

Fig. 38 — Range at which targets have the maximum apparent elevation

Figure 38 shows a single curve for each target altitude when the ASTD is negative. Each such curve becomes a spray of curves when the ASTD becomes positive. The curves belonging to each spray roughly indicate a range of different MIVRs which are possible for a fixed ASTD and target altitude when the ASTD is positive. The multiplicity of curves for positive ASTD corresponds to the dependence of the MIVR upon details of the sensor, target and atmospheric background, a dependence which led to only negligible variations when the ASTD was negative. The curves in the spray do not correspond in any one-to-one manner to the details of the sensor, target and atmospheric background, however, and may not span the full gamut of plausible MIVRs. The curves in the spray were generated as follows.

For a given target contrast and sensor noise level, the signal-to-noise ratio at the sensor's output will become high enough for detection of the target when the density of rays at the target exceeds a certain threshold. The threshold ray density depends upon the details of the sensor, target, and atmosphere: sensor noise; intrinsic brightness temperature of target; path radiance between target and sensor; path radiance from sensor to space or to hard background; radiance of hard background; and losses due to scattering by refractive turbulence. The relation is provided by an analog of the usual range equations used for monostatic radar and infrared systems, but recast in terms of ray density rather than range, so as to take ray bending into account. The calculation would be elaborate and the answers would depend upon a host of details, whereas results of wide applicability are desired in the present study. It therefore seemed preferable to simply pick several values of the threshold ray density at the target, and then see how sensitive the MIVR was to the choice. This divides the problem of calculating the MIVR into two parts: (1) determining the MIVRs for threshold densities of rays at the target; and (2) determining the threshold density of rays for a given combination of sensor, target and atmosphere. The answers to the first of these problems have considerable generality, and are presented here. The answers to the second problem would have to be obtained by users of the present results, using the details of the sensors, targets and atmospheres of interest. As a given target approaches a given sensor through a given atmosphere,

the threshold density of rays will change slowly as a function of the target's range. So the curve of MIVRs for an actual scenario will cut transversely across the curves calculated for fixed ray densities shown here.

(Some readers may object to the use of a ray density threshold, since the radiance from the source at a given point in the ray field is determined by absorption and scattering between the source and the point in question as well as by the local geometry of the field of rays. But the use of the ray density alone is correct for the present purpose. The radiance as computed from the ray density can always be corrected for absorption and scattering by multiplying by a transmittance factor, but this correction factor properly belongs to what was called "the second problem" in the previous paragraph. Only the factor due to the geometrical divergence of the rays belongs to "the first problem," which is being solved here.)

The calculation of the MIVR for a particular threshold density of rays is performed as follows.

Imagine a set of planes all intersecting on the radial line containing the source. (In the present case, it is convenient to consider the sensor to be the source.) In a spherically stratified atmosphere, any ray passing through the source must stay in one of these meridional planes. A plot of ray trajectories is therefore a (flattened-Earth) section of the three-dimensional ray field by one of these meridional planes. The two-dimensional density of rays across the local wavefront is a product of two one-dimensional densities: the density in the meridional plane shown in the ray traces, and the density in a plane which is perpendicular both to the local rays and to the local wavefront. The transverse density factor expresses the effect of the geometric divergence produced by the angles between the various meridional planes, and can be calculated by considering the angle between corresponding ray segments on two representative meridional planes. At a point where the rays are locally perpendicular to the radial through the source, the angle between corresponding ray segments on the two planes equals the dihedral angle between the planes; but at a point where the rays are locally parallel to the radial through the source, the angle between corresponding ray segments vanishes. These two cases correspond to defocussing and to collimation in the transverse direction, respectively. (In the two special cases just discussed, the ray segments were perpendicular and parallel to the radial through the source point, not to the radial through the current ray point. Thus the ray segments were not locally horizontal and vertical, respectively, in the two cases.) Let ϕ denote the dihedral angle betwen the two meridional planes which define the lateral extent of the ray tube containing the ray of interest, and let γ denote the angle between corresponding ray segments. Then for ray segments which need not be perpendicular or parallel to the radial through the source, the general result is

$$\cos\gamma = 1 - (1 - \cos\phi)\cos^2(\beta - \theta) \ . \tag{34}$$

For estimating the ray density, the ray tube must be made small. Then ϕ is small, and γ, which is bound between 0 and ϕ, is also small. The formula for γ then simplifies to

$$\gamma \approx \phi \cdot \cos(\beta - \theta) \ . \tag{35}$$

The derivative (with respect to refracted path length) of the density factor associated with the transverse spreading of the rays is proportional to γ. At almost all ray points of interest to near-surface side-looking

sensors, the angles β and θ are both small. In particular, β is small (at most a few tenths of a radian) at ray points near the upper branch of the tear. (The angle β may not *look* small on the ray traces, because of an optical illusion caused by the extreme difference between the horizontal and vertical scales in the diagram.) The angle θ is small because the along-surface ranges of interest are much less than the Earth's radius: for ranges less than 80 km, θ is less than 13 milliradians. The angle γ therefore remains close to ϕ, which is constant along the ray tube. The transverse spreading of the rays is close to that for rays which remain perpendicular to the radial through the source; the transverse density factor is then approximately inversely proportional to the along-surface range. For the purpose of determining the MIVRs of targets at altitudes exceeding the duct height, the density of rays can be taken to be the product of the one-dimensional density of rays in the plane of the ray traces and a factor inversely proportional to range. However, the second factor has not been included in the calculations leading to Fig. 38 and related figures. The resulting MIVRs are therefore overestimated when the ASTD is positive; the error increases with range, and therefore with ASTD.

(For near-surface side-looking sensors, the variations of γ have to be taken into account in only two special problems: when computing the density of rays striking the surface relatively close to the sensor (to compute the radiance from portions of the surface near the sensor), and when computing the MIVRs of targets having altitudes much less than the duct height (since rays in the lower branch of the tear can be nearly vertical).)

In computing the density of rays in the plane of the ray traces, it is essential to beware of a pitfall. Figure 39 shows rays and local wavefronts. The wavefronts coincide, to within a few microradians, with the vertical lines on the flattened-Earth plot. On the diagram, the wavefronts appear not to be perpendicular to the rays: the wavefronts are perpendicular to the rays in object space, but not in the diagram. This is another instance of the optical illusion caused by the extreme difference between the horizontal and vertical scales in the diagram. Angles are not preserved under linear transformations which stretch different directions by different amounts: such linear transformations are not orthogonal. A surface which was perpendicular to the rays on the diagram would not be perpendicular to the rays in object space, and would be a false wavefront. The density of rays across such a false wavefront would be very different from the density across a true wavefront. The vertical distance between rays in Fig. 39 is of the order of centimeters, and is close to the distance along a true wavefront. But the distance between adjacent ray points along a line which appears perpendicular to the rays on the diagram would be of the order of kilometers: small distances in the horizontal direction correspond to large distances in object space, because the horizontal axis is severely compressed.

Figure 40(a) shows the ray-to-ray distances along a particular wavefront, for 1 μrad increments in launch angle; the rays are for ASTD = +2.5°C. Figure 40(b) shows the corresponding one-dimensional density of rays. The plot of ray-to-ray distances is more informative than the plot of the ray density. The plot of ray-to-ray distances shows a sharp change in slope. In contrast, the density remains featureless all the way from near the duct to well inside the upper branch of the torn bundle of rays. If the shoulder in the plots of ray-to-ray distance occurred at the same ray density for wavefronts at different ranges, then the corresponding density would provide a purely geometric estimate of the edge of the tear.

Figure 41 shows a trajectory of constant in-plane ray density as a function of range. The density corresponds to a ray-to-ray distance of 100 cm for 1 μrad increments in launch angle. The trajectory of constant density can be regarded as an estimate of the edge of the upper branch of the torn bundle of rays. More precisely, the shape of the upper edge of the tear is indicated by contours of constant density, and the trajectory in Fig. 41 is one such contour. As expected, the contours defining the edge of the tear cut transversely across the rays.

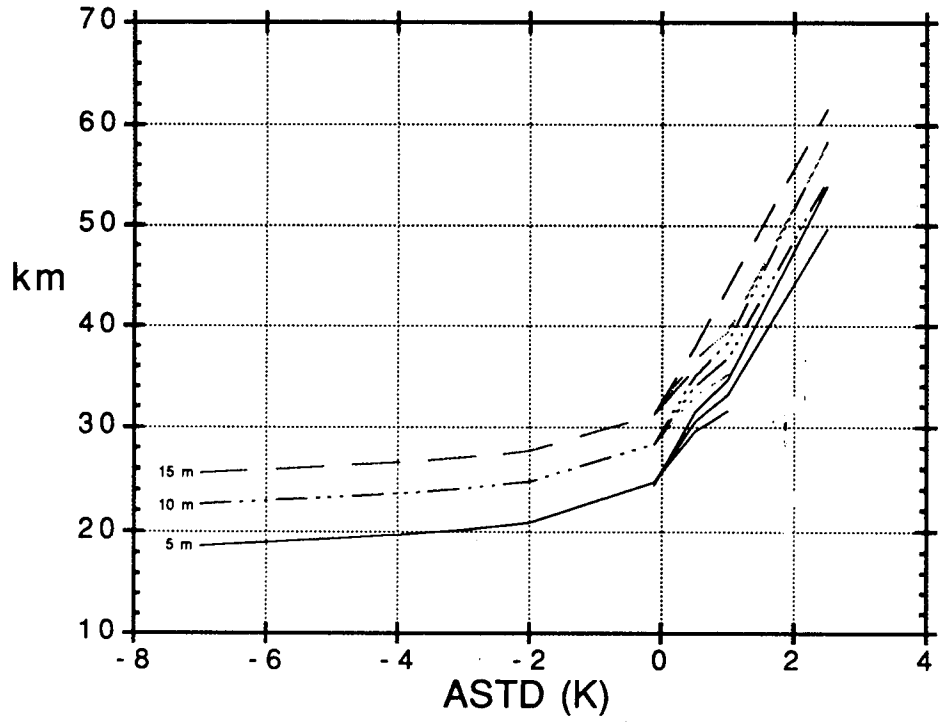

Fig. 39 — Maximum Intervisibility Range (MIVR) as a function of ASTD. Strictly speaking, for positive ASTD the quantity displayed here is not the MIVR (which ceases to exist), but rather a quantity from which detection range can be calculated from additional information about the sensor and target. The curves show the qualitative behavior of the detection range for positive ASTD.

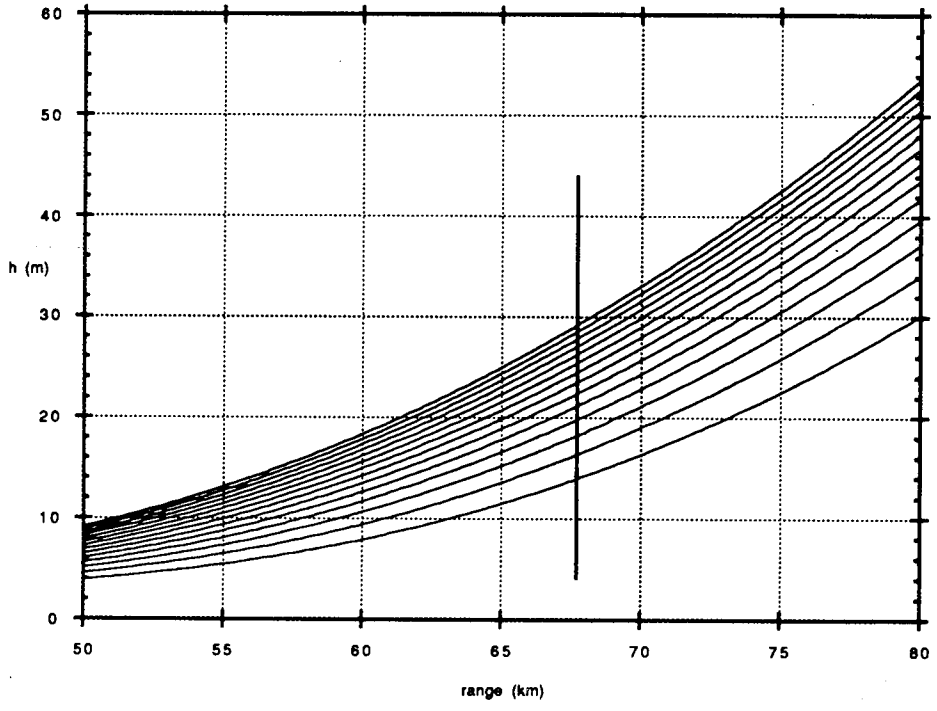

Fig. 40 — Rays and a wavefront which is perpendicular to them in object space, but is not perpendicular on the plot

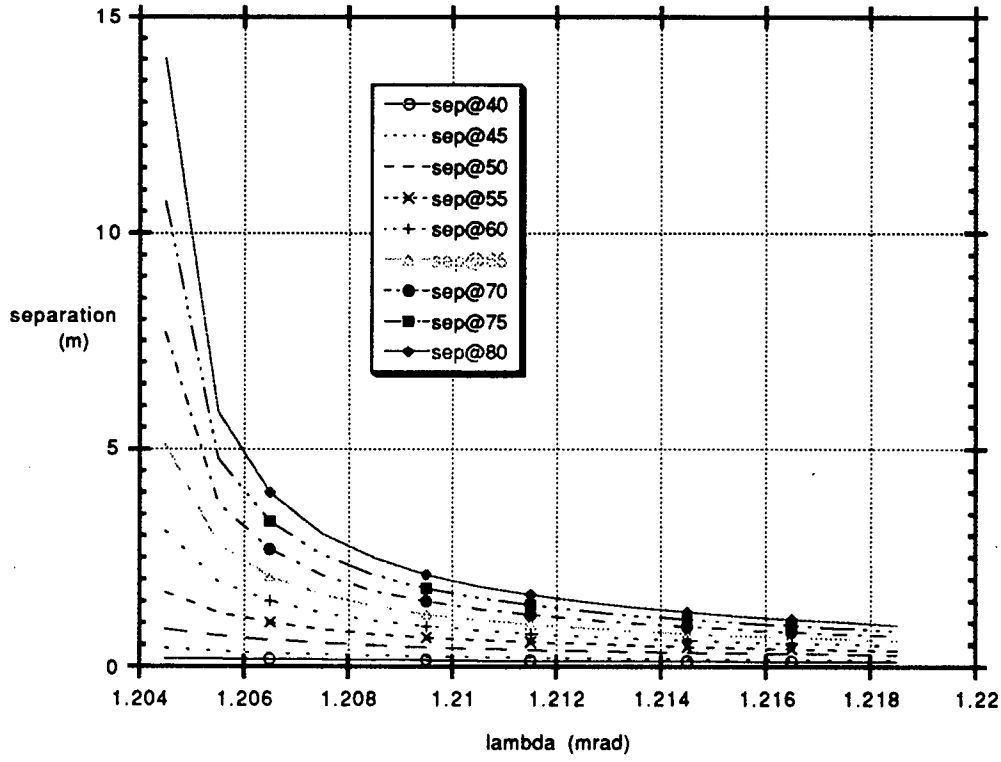

(a)

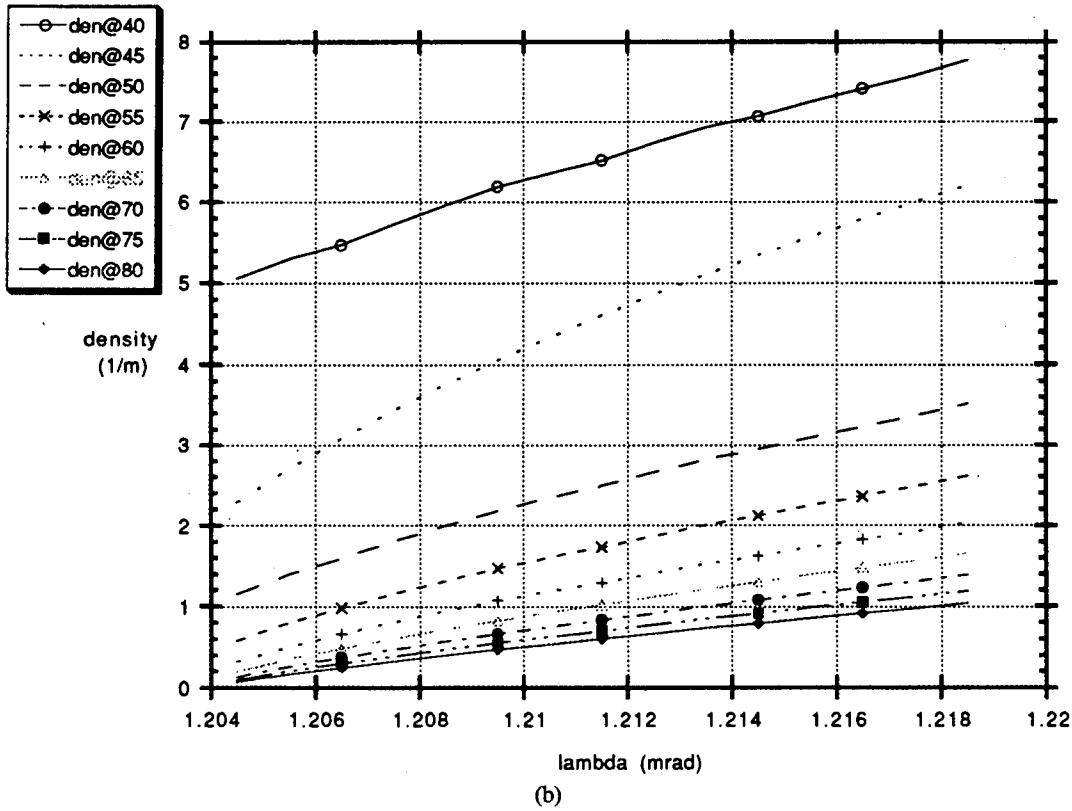

(b)

Fig. 41 — Spreading of rays in a meridional plane. Distances (a) and density (b) along a wavefront, between rays launched at 1 microradian increments in launch angle, for ASTD = +2.5°C.

Curves such as those in Fig. 41 were drawn for various choices of threshold density. The MIVR points for positive ASTD were taken to be the points where these curves intersected lines of constant target altitude. The sprays of curves in Fig. 38 were obtained by plotting the ranges of the points of intersection, as a function of ASTD.

(The threshold densities corresponded to ray-to-ray distances (for 1 μrad increments in launch angle) of 25, 50, and 100 cm: the distance doubled each time. These distances were chosen for convenience: for 1 μrad increments in launch angle, distances of the cited amounts occurred near the target heights of interest for most of the ASTD of interest. The arbitrariness of the threshold distances follows from the earlier discussion of the factorization of the analysis into a purely geometric problem and a detail-dependent problem.)

Despite the ambiguity in the MIVRs for positive ASTD, Fig. 38 shows the MIVRs for positive ASTD to be much larger than those for negative ASTD. This feature is also observable directly from the ray trajectories.

The MIVR gives the target's range when it first becomes visible; it is also useful to know the target's apparent direction at the moment when it first becomes visible. For negative ASTD, this information can readily be read from plots such as Fig. 22. For example, Fig. 22 shows that when a target flying at 15 m first becomes visible, its apparent direction lies above the straight-line horizon. For positive ASTD, the apparent directions of the MIVRs can be read from the same points of intersection that were used in generating the right-hand portion of Fig. 38. Figure 42 shows the results; as in Fig. 38, each curve in Fig. 42 is single valued for negative ASTD, but splits into a spray of curves for positive ASTD.

Target Range for Fixed Apparent Directions

Ray-bending affects the range of a target having a particular apparent direction. Figure 43 illustrates this refractive displacement, for the special case of a target whose apparent direction momentarily coincides with the direction of the straight-line horizon ($\Lambda = 0$). Analogous figures could be drawn for other choices of apparent direction.

In the absence of refraction, the direction $\Lambda = 0$ would have a special significance. It would separate the directions in which the sensor saw the surface from those in which it saw the sky. Targets seen at negative values of Λ would be viewed against the background of the sea surface, with its associated clutter. The analog (for no ray bending) of Fig. 43 would demarcate the range at which the target first had to be distinguished from surface effects: a target would be seen against the surface only when its range was smaller than that shown in the straight-ray analog of Fig. 43. If this interpretation remained valid in the presence of ray bending, Fig. 43 would be extremely useful for system designers and users. For reasons to be discussed in the next subsection, this is not the case: in the presence of ray bending, Fig. 43 should *not* be interpreted as showing the range at which the target is first seen against the surface.

The Apparent Horizon and Near-Surface Phenomena

A sensor aimed sufficiently high sees the sky; if a target is present, it is seen against a background of sky. The near-horizon sky is often smooth: a benign background against which to detect a target, especially in the IR. A sensor aimed sufficiently low sees the surface, or a target against the background of the surface. The surface is typically a more difficult background, particularly when sun glint is present.

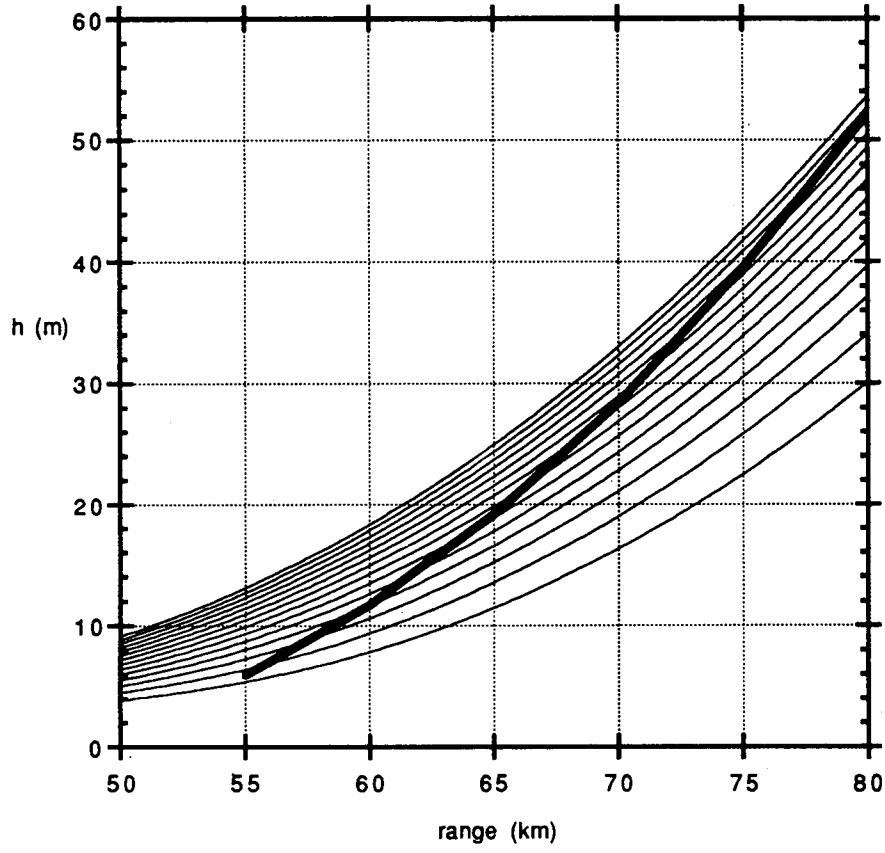

Fig. 42 — Trajectory of constant ray density in the plane of the ray traces, for ASTD = +2.5°C. The constant density corresponds to a 100 cm separation (along the wavefront) of rays launched at 1 microradian increments in launch angle. The curve indicates the shape of the edge of the tear in the bundle of rays.

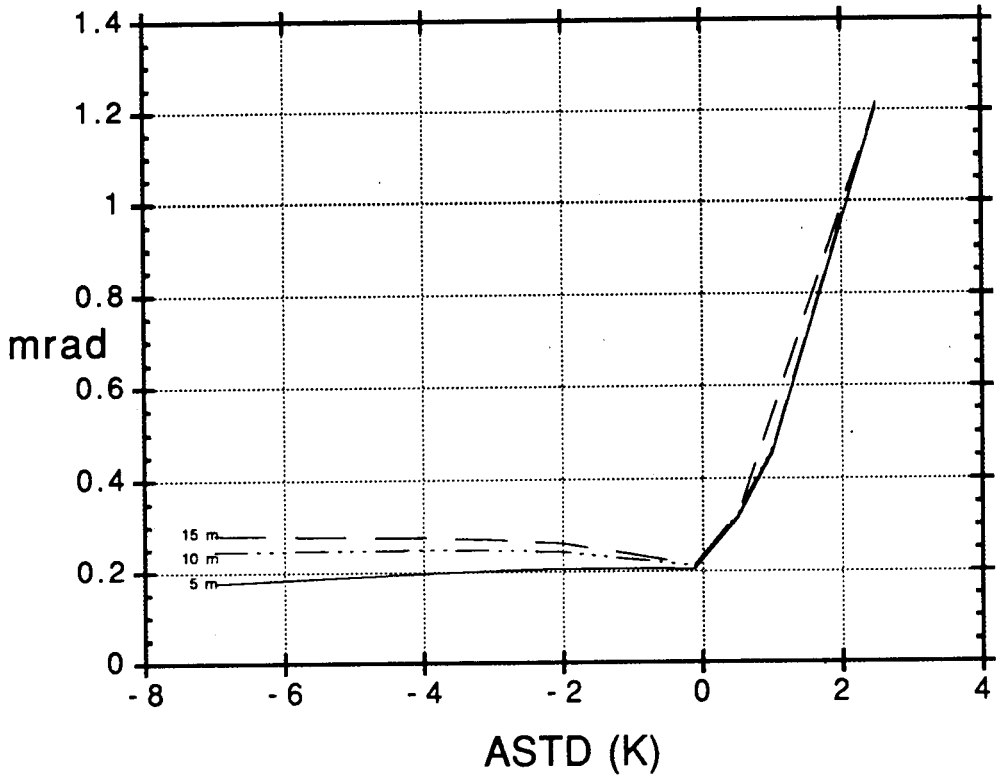

Fig. 43 — Apparent direction of the target when it is at the MIVR (for negative ASTD) or at the indictative range shown for positive ASTD in Fig. 41

The transition between these extremes may be sudden or gradual. When the transition is sudden, it constitutes a well-defined horizon as seen by the sensor. Figure 44 illustrates a sharp IR horizon as seen by a PtSi sensor whose characteristics will be discussed in the next section. When the apparent horizon is sharp, its direction is important to the designers and users of horizon-searching sensors: once the apparent direction of an approaching target crosses that of the apparent horizon, the target must be distinguished against the sometimes intricate pattern of radiance produced by the surface. Even when the transition is gradual, it is useful to know the directions in which surface effects are likely to become important.

As discussed in an earlier subsection, the horizon transition should be gradual when the ASTD is positive. The density of rays is extremely low in the vicinity of the tear between the upper and lower branches of the ray bundle, and this low density suppresses the effects of targets, sun glint, clipping by waves, aerosols, and turbulence. The horizon transition should be more abrupt when the ASTD is negative, because the ray density never becomes very small near the surface in that case. The sharpness of the horizon when the ASTD is negative is borne out by modeling and measurements described by Priest, Shettle, and Takken (1992); however, the sharpness of the radiance horizon is found to vary from day to day. The location and sharpness of the radiance horizon should vary significantly with waveband, despite the insensitivity of the refractive index to waveband throughout the visible and IR. In the experiments just cited, the atmospheric transmission windows and the spectral response of the detector caused the signal to be dominated by wavelengths from 2 to 2.4 μm. The same reference also discusses clipping by waves.

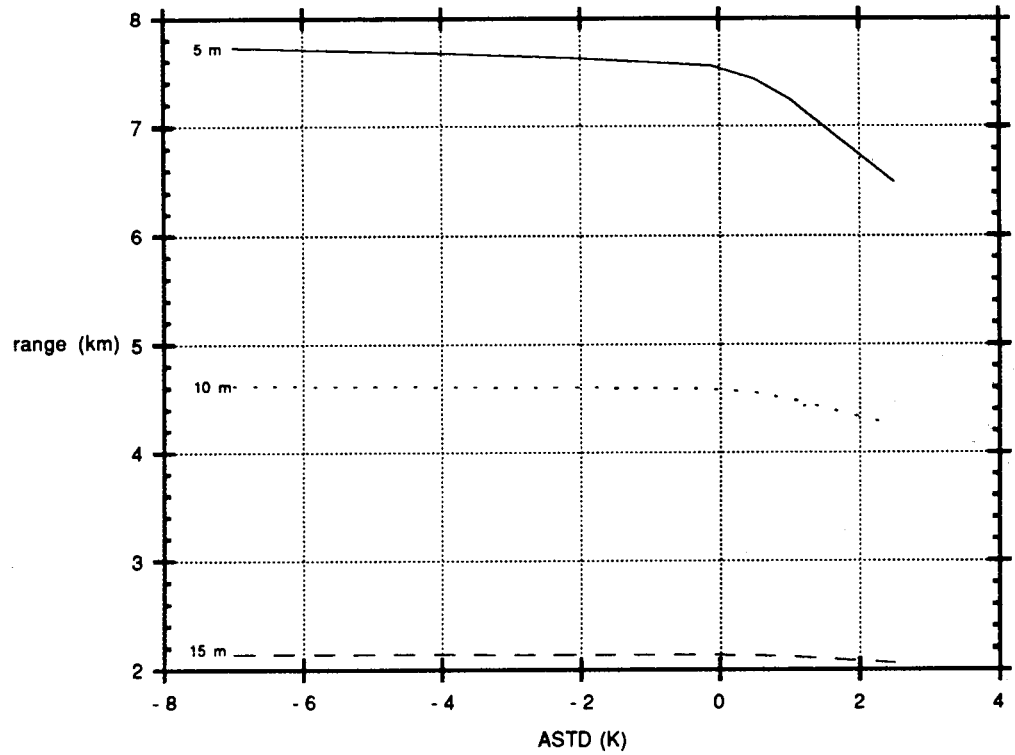

Fig. 44 — Range of target when its apparent direction coincides with the straight-line horizon. Only the first crossing of this direction is shown; there is a second crossing at shorter ranges.

Figure 1(b) showed typical ray trajectories for positive ASTD. The ray density near the surface gradually increases as the range to the sensor decreases, becoming large when the sensor is aimed sufficiently downward. The ambiguity in defining the apparent horizon for positive ASTD is therefore similar to that in defining the MIVR for positive ASTD. The apparent horizon is well defined for any particular combination of sensor and atmosphere, but depends upon a welter of details extraneous to the ray trajectories. The atmospheric details include the profiles of aerosol concentration and of the parameter C_n^2 which describes the refractive strength of turbulence; these profiles depend in turn upon the wind speed, absolute humidity, sea state, and proximity to land. It would be possible to divide the problem into two subproblems, much as the estimation of the MIVR was divided earlier. One of the subproblems would be solved by determining the ranges at which the density of rays attained various threshold values. For positive ASTD, rays launched at sufficiently steep angles actually strike the surface, so the determined ranges would correspond to well-defined apparent directions. The answers to this first subproblem would have considerable generality, since they would depend only upon the ray trajectories. The second subproblem would determine the appropriate threshold density of rays for a given combination of sensor and atmosphere.

Although this factorization approach was used in an earlier subsection to estimate the MIVRs for positive ASTD, it will not be adopted here to estimate the apparent horizon for positive ASTD. The factors affecting the second subproblem are more complex for the horizon problem than they were for the MIVR problem, and models adequate for solving them are unlikely to be available in the near future. So the solution of the first subproblem would have less value than it did for the MIVR problem.

Instead a simpler approach was adopted, namely, to determine the apparent directions of the refractive ducts. The apparent direction of the refractive duct is an upper bound on the apparent direction of the horizon, since the refractive duct occurs at the heart of the tear between the upward and downward bound branches of the ray bundle. Although not much of interest will be seen in the apparent direction of the refractive duct itself, the apparent horizon should be fairly nearby below it, where the density of rays in the lower branch becomes adequate. The apparent direction of the refractive duct therefore has indicative value. It is shown in Fig. 45. The plotted values were determined (to within the nearest μrad) from the ray trajectories, as follows. A set of rays which bracketed the tear were launched with one microradian increments in launch angle. The launch angle of the most upward-launched ray to strike the surface was then averaged with the launch angle of the most downward-launched ray which eventually rose upward.

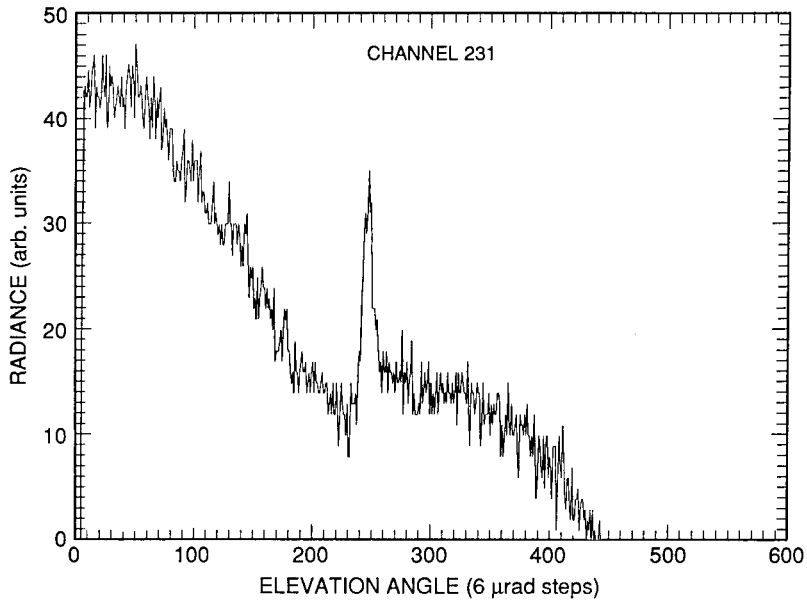

Fig. 45 — Radiance as a function of angle in the vertical plane, for a vertical plane which contained a bright source. The data were obtained as discussed in the text.

For positive ASTD, a target flying above the refractive duct will first be seen against a background of sky as long as the sensor quality and target contrast allow the target to be detected somewhere in the upper edge of the tear. For a low quality sensor or poor contrast, the target will not be detected until it intercepts surface-striking rays from the sensor, and in this case the target is, by definition, seen against the surface.

For negative ASTD, the apparent horizon must be estimated by a different approach, since rays do not actually strike the surface when the Monin-Obukhov refractive profiles are used, except for rays launched so steeply downward as to be irrelevant for determining the horizon. If one ray (in the relevant range of launch angles) is launched more steeply downward than another, it rebounds more steeply upward, and closer to the surface: this is the same behaviour which causes the ray crossings which produce mirages. The refusal of rays to strike the surface is an artifact of the Monin-Obukhov model of the meteorological profiles: the modelled refractivity gradient becomes infinite as the surface is

approached, because of the logarithm in Eqs. (19) through (21). (The other terms in these equations are nonsingular as $z \to 0$.) The divergence arises because the model neglects molecular diffusion of heat and substance, which become significant very close to the surface. But extending the model to include these effects would not be the right way to estimate the geometric horizon. In view of the presence of waves, aerosols and turbulence, the observed horizon is unlikely to be determined by phenomena occuring within the first few microns of the ever-changing surface.

An indication of the apparent direction of the horizon for negative ASTD can be gotten from the launch directions of the rays which first reach within various specified distances of the nominal (flat) surface. Figure 46 shows these directions, for altitudes of 9, 18, and 36 cm. (The chosen altitudes double from one case to the next. The lowest altitude is where rays terminated in all the other calculations in this paper. The reason for this coincidence will be explained in the next paragraph.) In view of the typical heights of waves, the altitude which determines the actual radiance horizon seems likely to fall within the range spanned by the chosen values, for any meteorological condition in which near-surface based horizon searching is of practical interest. The actual apparent horizon will not follow a curve defined by any particular termination height. Indeed, insofar as aerosols and turbulence influence the actual apparent horizons, the actual horizons will not be describable by a single-valued function of ASTD alone, but will depend also upon wind speed and absolute humidity (and therefore upon relative humidity and surface temperature). Nonetheless, if data on the apparent direction of the radiance horizon were available as a function of ASTD (preferably, for each of several bins of wind speed, relative humidity, and surface temperature), the migration of the actual curve amongst the curves of constant termination altitude would provide clues as to the mechanisms determining the radiance horizon.

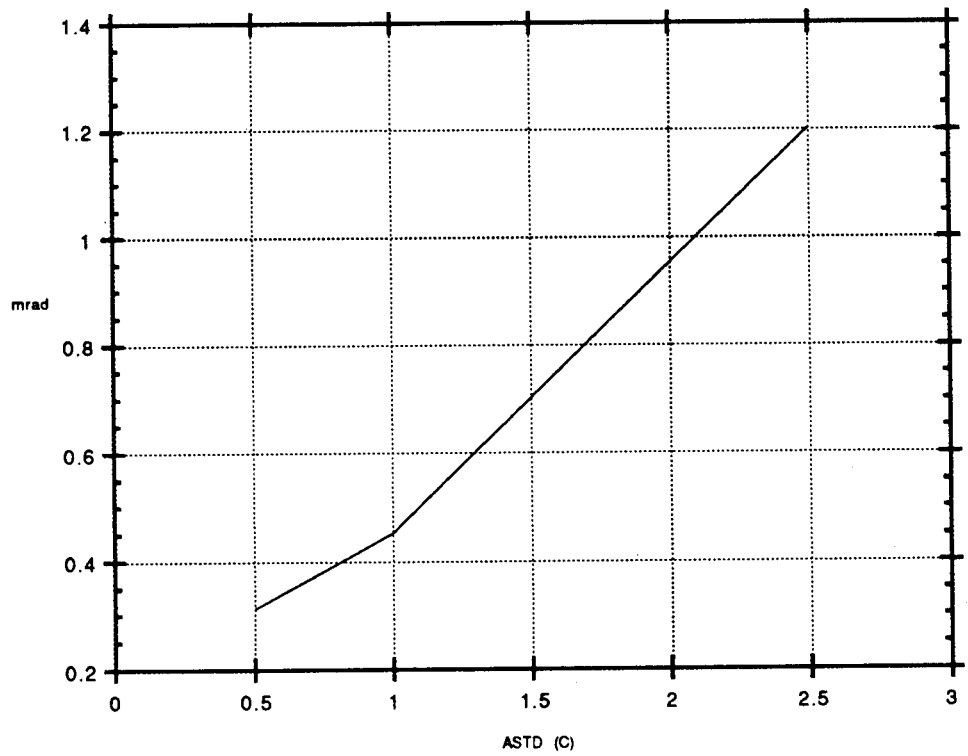

Fig. 46 — Apparent direction of the refractive duct, as seen from above. A ray launched in this direction will asymptotically approach the top of the refractive duct. The density of rays will vanish asymptotically as the ray approaches the duct.

For negative ASTD, the upper branch of the mirage always has a background of sky, whereas rays in the lower branch may or may not pass close to the surface on the way from target to sensor. At the MIVR the upper and lower branches of the mirage merge, and so do the corresponding rays. When the target is first seen, it will therefore be seen against sky if the merged ray does not dip close to the surface, but will be mixed with radiance from near the surface otherwise. The duration (in range) of the mirages in Figs. 22 through 30 indicates whether the rays at the MIVR came close to the surface or not, since the lower branch of the mirage was terminated when the lower ray approached within 9 cm of the surface. Thus the target will first be seen against sky in those cases (as in Fig. 22) where the mirage endures for a considerable distance, but will be seen against surface radiance in those cases (as in Fig. 30) where the mirage is brief.

As was mentioned in an earlier subsection, the duration (in range) of the mirage depends upon the rule for terminating rays which dip too close to the surface. The proper rule for terminating rays is presently unknown, for the same reasons which render the calculation of the radiance horizon uncertain for negative ASTD. Figure 46 provides an indication of how the duration of the lower branch of the mirage would be affected by changes in the termination rule. In detail, for a given negative ASTD, Fig. 46 shows how much the lower limit of the launch angles would be raised if the termination altitude were raised from its usual value of 9 cm. The lower branch of the mirage in a figure such as Fig. 22 would have to be terminated higher on the vertical axis by an equal amount. The new minimum range for the lower branch of the mirage can be read from the point underneath the corresponding point of the lower branch of the bird's head.

The previous subsection warned that Fig. 43 should not be interpreted as defining the clutter horizon. Instead, the figures presented in the present subsection should be used for estimating the direction of the radiance horizon; for a target of specified altitude, the corresponding range on the appropriate bird's head plot then gives the range at which the target begins to be seen against surface radiance.

Several articles and reports are relevant to the topics discussed in this section: Feinberg and Hughes (1979), Hughes (1989), Priest and Schwartz (1988), and Fulkerson et al. (1989).

COMPARISON WITH FIELD TESTS

As part of the Infrared Analysis, Measurements and Modeling Program (IRAMMP), near-surface IR propagation has been measured at Wallops Island, Virginia, in the Florida Keys, and at the Naval Research Laboratory's Chesapeake Bay facility. Two sensors have been used, although both sensors were not used at both sites. One sensor uses PtSi detectors sensitive over a rather broad MW spectral region, and has very good angular resolution. The other sensor provides data in both the MW and LW spectral regions, but with less angular resolution. At both sites the sensors were fixed on an elevated platform, and looked at a boat carrying a propane burner which served as a bright IR source. The sensors and field experiments are described in detail by Priest, Shettle, and Takken (1992), by Takken et al., (1991), and by Kessler et al. (1989).

The PtSi sensor has a 30 in. aperture and a 3 milliradian field of view. Its focal plane array has 512 $\times$ 512 detectors, each having a 6 μrad field of view. The sensor is used in a staring mode. The detectors respond to wavelengths from roughly 1.8 to 5 μm, as set by the PtSi material. Data obtained with this sensor have been shown in Fig. 44, in connection with the discussion of the radiance horizon. The radiances shown are not calibrated: they are merely the deviations of the output from a reference value.

The IRAMMP sensor has a 6 in. aperture. Its focal plane contains MW and LW linear arrays, each detector having an instantaneous field of view of 230 μrad. The IRAMMP sensor is used in a scanning mode.

The application of the refractive models to the analysis of field test data will be illustrated with one set of data obtained with the PtSi sensor at Wallops Island, on June 27, 1991. The sensor was at 22.25 m above mean-sea-level. In principle, the sensor height to be used in the comparisons with the model should be corrected for the tides at the time the data were taken. In the present case, no correction was made for tides, since tides at Wallops Island have unusually small amplitudes. The boat-borne target was about 3.1 m above the water. These sensor and target heights differ from those used in generating the figures presented so far, but are close enough to permit a rough analysis using the existing figures. (The plots of apparent direction vs range are tedious to generate with the present software, and have not yet been generated for this experiment.) Although the comparison between data and model is preliminary and crude, it already provides a partial validation of the refractive model.

Figure 48 shows data on the apparent direction of the target as a function of range. (The data have been corrected for various artifacts.) The information provided by Fig. 48 is analogous to that provided by the bird's head plots, Figs. 22 et seq., except in one respect. In Fig. 48 the vertical axis shows angles as measured from a fixed but unknown reference direction, whereas in Figs. 22 et seq. the angles are relative to a known origin, the straight-line horizon. Under the conditions of the field tests, the sensor's narrow field of view rendered it difficult to use an absolute origin, such as the local horizontal, which was far from the directions to be viewed. Instead, the apparent horizon was roughly centered in the sensor's field of view, and directions were measured relative to the center of the field of view. As discussed earlier, the direction of the apparent horizon varies with near-surface meteorological conditions, cloudiness, and the direction of the Sun; therefore, the relation of the sensor's angular origin to any absolute origin is not known *à priori*. To compare all of the most system-relevant predictions of the model to the data, the angular origin must be known. The analysis which follows will show how this origin can be estimated from the data and the model, thence permitting a fairly comprehensive comparison of the two.

Even without knowing absolute angles, it is easy to determine from Fig. 48 the range at which the target has its maximum apparent elevation. The maximum apparent elevation corresponds to the top of the bird's head, and hence to a range of about 16 km. The range of the point of maximum apparent elevation is not subject to the experimental uncertainties which occur in trying to measure the maximum detection range, as discussed later.

Look now at Fig. 37, and for this preliminary analysis ignore the difference between the 22.25 m actual altitude of the sensor and the 20 m altitude for which Fig. 37 was calculated. The discrepancy in the altitude of the target is more critical, because the results become somewhat sensitive to target altitude when that altitude is low. The discrepancy in target altitudes will be handled by crudely extrapolating the families of curves in Figs. 38 and 42. A curve for a target height of about 3 m would lie a little below the lowest curve in Fig. 37 and would be roughly parallel to it. This crude information is enough to indicate that the ASTD is near zero, but slightly negative.

The inference of a small negative ASTD is supported by the in situ measurements of temperature. The temperature of the air (at 6 m) and of the surface both increased during the 4¼ hours of data taking, but the ASTD showed no systematic trend. The average of the in situ ASTD values is −0.11°C. But this is $ASTD_6$ (that is, the ASTD when the air temperature is measured at 6 m), whereas all the curves

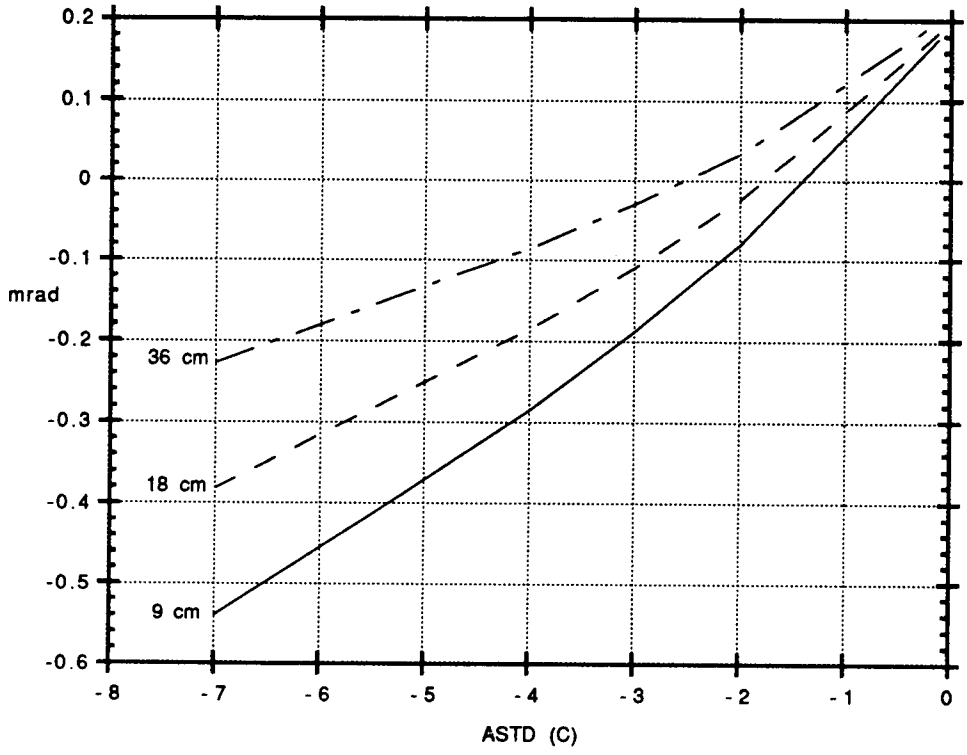

Fig. 47 — Apparent direction of the rays which become horizontal at small heights above the nonimal surface

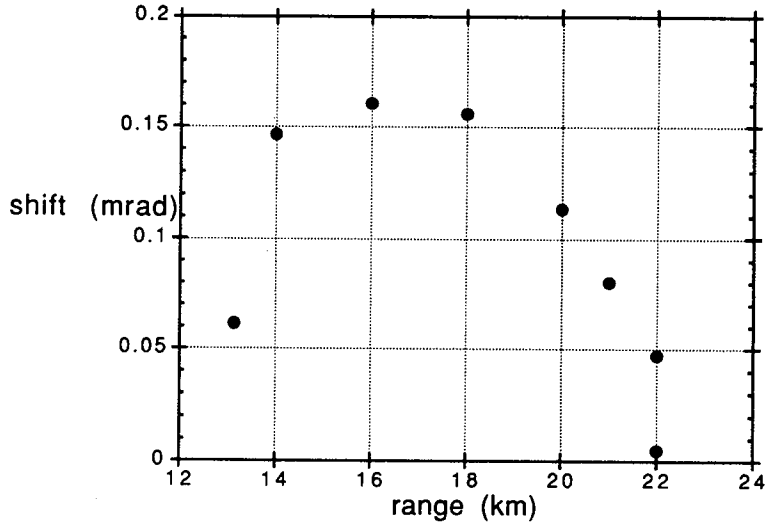

Fig. 48 — Relative apparent direction as a function of range; measurements at Wallops Island, June 27, 1991

for the model are labeled by $ASTD_{12}$. Figure 49 shows a temperature profile calculated using the DREV refractive profile code, for $ASTD_6 = -0.11°C$ and for the average surface temperature (22.1°C) and wind speed (2.6 m/s) pertinent to the data. Figure 48 shows $ASTD_{12}$ to be −0.146°C (−0.15°C, to a more realistic accuracy). On the scale of Fig. 37, this would indeed appear as a small negative value. This confirmation supports the model.

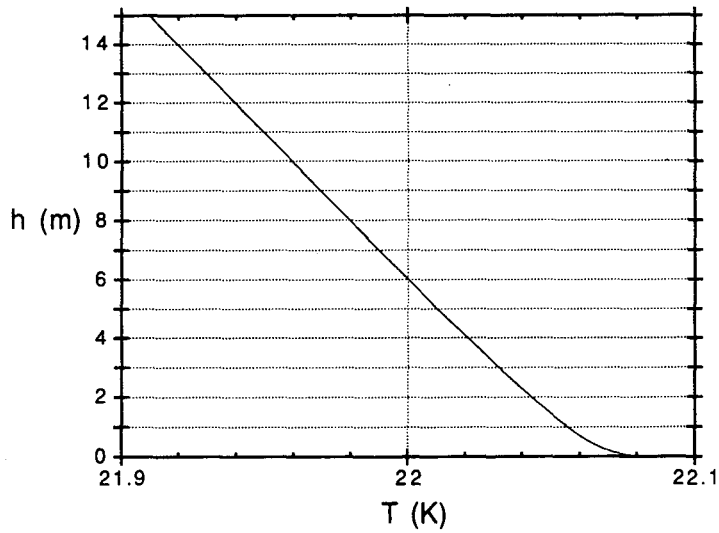

Fig. 49 — Modeled temperature profile based on the meteorological data for June 27, 1991

The present analysis infers the ASTD from Fig. 37, using the in situ measurements used only as a check. This avoids undue dependence on the assumption of horizontal inhomogeneity, which is more often violated in coastal waters than in the open ocean.

Figure 48 resembles Fig. 30, which is for a similar target altitude and ASTD. This is additional support for the model.

Turning to Fig. 36, a small negative ASTD and a target altitude of about 3 m implies that the maximum apparent elevation is about +0.35 to +0.40 μrad above the straight-line horizon. According to Fig. 47, the maximum apparent elevation is +0.16 μrad above the fixed but unknown angular origin. Hence the angular origin used in recording the data must be +0.19 to +0.24 μrad above the straight-line horizon. The angles in the data are now known relative to an absolute origin.

The two rightmost points in Fig. 48 resulted from an attempt to determine the MIVR during the field experiment. Since the source was bobbing up and down on a small boat, the maximum range was judged to occur when the source could be seen only about half the time. The occurence of two rightmost points is due to the experimental uncertainties; in principle, the MIVR should correspond to the single point at the tip of the bird's beak in a figure such as Fig. 30. The two points probably do not correspond to the upper and lower branches of a mirage, because these data were acquired during an attempt to determine the maximum range at which the source was visible.

According to Figs. 38 and 42, when the ASTD is small and negative a target at an altitude of 3 m should have a MIVR of about 24 km, and should appear to be about +0.2 μrad above the straight-line

horizon when it first becomes potentially visible. A MIVR at 24 km is in reasonable agreement with the range of the two rightmost points of Fig. 48. (If the two points represented a mirage rather than the MIVR, a MIVR of 24 km would agree with Fig. 48 even better, since the tip of the beak would be somewhat to the right of the mirage points.) A direction $+0.2$ μrad above the straight-line horizon should be -0.04 to $+0.01$ μrad above the angular origin used in recording the data. This, too, is compatible with the data. Given the experimental uncertainties and the crudeness of the preliminary analysis, the range and apparent direction of first visibility provided by the model agree remarkably well with the data.

DISCUSSION AND SUMMARY

Models of near-surface refraction are useful to designers of hardware and algorithms for surface-based horizon-searching sensors and point-defense weapons, and to the users of such systems. Refractive models tell hardware designers the range at which the target first becomes potentially visible, and hence the time available for responding to the target. This determines the update rates needed by target-search sensors. The modeled dependence of detection range on the sensor's signal to noise ratio helps to determine the needed detectivity and size of the detectors, and their integration time. Refractive models indicate the range of apparent directions spanned by the target in various portions of its trajectory, and how much the apparent directions and velocities deviate from the true ones. This places additional constraints on the size and integration time of the detectors. The same refractive information is also useful for the designers of algorithms for detection, track-estimation, and target tracking. In addition, refractive models tell algorithm designers when mirages or refractive ducts are likely to occur, and the time-varying angular extent of mirages. The models indicate whether the target will become visible suddenly at a range which is relatively short but independent of the details of sensor, target, and atmosphere, or whether the target will become visible gradually at a range which depends significantly upon the sensor noise and target contrast. Likewise, the models indicate when the apparent horizon will be sharp and when it will be gradual, and how close the target must approach before it must be distinguished against radiance from the surface. Users of deployed systems also benefit from knowing how far away, how suddenly, and at what elevation angle a target is likely to appear. Since the effects of refraction depend upon the meteorological conditions, a refractive model allows thresholds for detection and tracking to be updated according to user-supplied local meteorological measurements.

The present report reviewed models presently available for computing near-surface refraction, and applied the models to extract representive information useful for applications. Methods were outlined for comparing a refractive model to field measurements and for using the model to estimate angular offsets which are difficult to measure under field conditions. A very preliminary analysis of field data supported a wide variety of predictions by the model.

A refractive model has three components: (a) computation of the refractivity profile from the values of near-surface meteorological parameters; (b) calculation of ray trajectories, based on the refractivity profile; and (c) extraction of information from the ray trajectories. Computer codes presently exist for the first two of these components, but the last one has not yet been automated. Extraction of information from the ray trajectories is an iterative and often intricate process, involving manual and computer-aided measurements on plots, the extraction of isolated pieces of information from computer-generated tables, and manual data entry. The set of rays to be traced must frequently be revised in the light of the results of partial analyses. Present plans include writing software for extracting information from the ray trajectories. Because of the iterative character of the ray analyses, the analysis software will have to be integrated with the ray-tracing software. To generate plots as a function of the meteorological conditions, it would be desirable for the integrated software package to include the profile generating software

package as well. The profile-generating and ray-tracing programs discussed in this report are candidates for inclusion in the integrated package.

The four refractive-profile models discussed in this report all use the Monin-Obukhov scaling theory of the profiles of passive scalar quantities in the near-surface atmosphere. This theory is valid when turbulence driven by the horizontal wind (rather than laminar or turbulent vertical convection) dominates the vertical mixing, and applies at altitudes where the surface is close enough to have a strong influence. The theory fails when the horizontal wind is weak, such as in a dead calm. The big advantage of the Monin-Obukhov theory is that its parameters can be obtained from a few feasible measurements: the temperature at a moderate height and just above the surface, and the wind speed and relative humidity at a moderate height above the surface. The NOSC, DREV, and NPGS/NRL refractivity models differ in how they estimate the Monin-Obukhov parameters from the meteorological measurements.

Of the four refractive profile models, attention can be restricted to three, since DREV's older model has been superceded by its newer model. The NOSC, DREV and NPGS/NRL refractive profile models give similar results (especially for the refractivity gradient) under most conditions, but under some meteorological conditions the NOSC model gives different profiles of refractivity and temperature than the other two. The DREV and NPGS/NRL models generally agree well, despite their different ways of inferring the parameters of the Monin-Obukhov theory from the meteorological measurements.

The overall agreement between the DREV and NPGS/NRL refractivity models suggests that these two models may be adequate, at least when the horizontal wind is strong and there is adequate horizontal homogeneity. Of course, validation requires experimental checks, not just internal agreement. The analysis described in the previous section of this report provides some preliminary experimental support for the refractivity model, but has to be refined and applied to additional data. Measurements of long-path refractive effects test the refractivity model jointly with the assumption of horizontal homogeneity (and, more trivially, with the ray tracing code). Since horizontal homogeneity can occasionally fail, especially at the relatively near-shore locations used in most field measurements (see the Appendix), it would be desirable to test the refractivity model by itself. A test of the refractivity model, independent of horizontal homogeneity, would require measurements of the profiles of refractivity, temperature, and horizontal wind speed. Even when an array of sensors is available, such measurements seem to be difficult on a small boat. As stressed by Walmsley (1988), even downwind obstacles can have a significant effect on tests of the Monin-Obukhov wind and temperature profiles. Hence even isolated islands are not an adequate site for the measurements, unless they are low above the water.

Provisionally assuming the correctness of the DREV and NPGS/NRL refractivity profile models, DREV's model would be the better one to incorporate into the future integrated package. DREV's model is the most developed. In particular, it includes the effects of the spatial variation in surface height caused by the waviness of the surface (Beaulieu, 1992). The original motivation for including these effects was to handle the repeated reflections which occur when a refractive duct is present, particularly in the RF spectral region, where surface reflections are strong. Although originally motivated by concerns about RF reflections, the physical arguments for the corrections are convincing and general. They apply to near-surface refraction as well as to reflection in all spectral regions. The corrections behave very plausibly, and although they have not yet been experimentally validated, they probably represent a significant step forward in modeling propagation very close to the surface. Admittedly, very near-surface refraction is less important in the visible and IR than in the RF, because of weaker reflections. Regardless of the role of reflections, for typical target and sensor altitudes many of the important effects of ray bending do not involve rays which dip close to the surface. In addition, a complete treatment of very near-surface propagation would have to include aerosols and turbulence.

Nevertheless, the inclusion of corrections for surface relief would lead to a more versatile integrated software package, since RF propagation could be more readily included. Corrections for surface relief are also a necessary ingredient of any future solution of the serious problems of determining the rule for terminating near-surface rays, and of computing the apparent horizon in the visible and IR spectral regions.

The ASTD is the air temperature at some upper altitude minus that just above the surface. As discussed earlier, confusion can result when comparing field measurements or models using different upper altitudes for the meteorological data, unless the difference in the altitudes is recognized and is corrected for. Although the differences in the ASTDs are not large numerically when both altitudes are large, they will (if not corrected) slowly but monotonically increase the entropy of discussions in this field. When one or both upper altitudes are small, the differences in the ASTDs can be numerically significant; an example would occur if field measurements obtained from a small boat were used to estimate the performance of a sensor mounted on a large ship. The refractive profiling component of the integrated software package should therefore be extended to conveniently provide the temperature and ASTD referred to any altitude, given the near-surface air temperature, upper air temperature or ASTD, relative humidity and wind speed referred to any other upper altitude. Of course, both of the upper altitudes must be within the region of validity of the Monin-Obukhov theory, and the wind speed must be sufficiently large. Limitations on the region of validity of the profiles are discussed in this report in the Appendix, in the section entitled *Profiles of Intensive Variables*, and in the paragraph following Eq. (23); they are also discussed in Beaulieu (1992).

The present report emphasizes the visible and infrared portions of the spectrum. Although similar methods can be applied at radio frequencies, typical behavior at radio frequencies differs from that in the visible and IR. Beaulieu (1992) has instructive comparisons between RF and visible/IR propagation. Water vapor has a stronger influence on the refractive index at radio frequencies. Consequently, near-surface RF propagation is often complementary to that in the visible and IR: there are often refractive ducts at RF when there are mirages in the visible and IR, and vice versa (Beaulieu, 1992, p. 30). Whereas the ASTD is the most important meteorological parameter for visible and IR propagation, the relative humidity and the ASTD are both important for RF refraction. Reflections from wave tops are very significant in the RF region, but are much less so in the visible and IR. In the RF it is therefore especially important to include the refractive effects of wave topography, which can be estimated by Beaulieu's (1992) method.

The ray tracing routine incorporated in the integrated software package should produce smooth rays: kinks caused by the discreteness of the refractive profile table introduce serious quantization noise into quantities calculated from the ray trajectories. Both of the NRL ray tracing codes produce smooth rays. For analysis of the traced ray trajectories, the equispaced steps in range produced by ALLRAYS2 are much more convenient than the automatically adapted, unequal steps used by ALLRAYS1. Some types of information can be obtained from Bouguer's theorem without tracing entire ray trajectories.

Extraction of useful information from the ray trajectories would be substantially easier if the ray tracing program included in the integrated software package provided information on the angular divergence of the rays, along with the position information presently provided. The angular divergence is needed in the plane perpendicular to that of the ray traces, as well as in the plane of the ray traces. Providing the additional information for all ray points would increase processing time and storage requirements, however. ALLRAYS1 (but not ALLRAYS2) presently lists the local direction of the ray along with its position; this, too, is useful for some types of analysis, and since the ray direction must be computed to trace the rays, it does not require additional computing time. Computation of the two angular divergences is much more complicated, however.

Many important features of the rays can be determined directly from Bouguer's conservation law, Eq. (31), without any need for tracing rays. For example, the minimum altitude of the rays as a function of look angle can be obtained from Eq. (31) by setting $\beta = 0$ and solving for r (or h). Using these values of r or h, the along-surface range can be obtained by evaluating a definite integral. This would provide all the information needed for an alternate method (Beaulieu, 1992, pp. 10-12) of computing the MIVRs when the ASTD is negative, or for deriving plots analogous to Fig. 46. For obtaining the special types of information just described, the use of Eq. (31) together with a numerical integration is potentially faster than ray tracing. The integrated software package might therefore include this capability along with a ray tracing capability. (If Eq. (31) is used, a warning is in order. Equation (31) is used extensively in ALLRAYS1. Experience in developing ALLRAYS1 showed that double precision arithmetic and series expansions of the cosine are needed to avoid loss of significant figures when using Eq. (31). The loss stems from two features of near-surface, nearly horizontal propagation: the differences between radii are small compared to their values, and the refractive effects derive from small changes in the cosine of the very small angle β.)

Analysis of ray trajectories leads to the following conclusions, for a sensor at 20 m and targets at altitudes of 5, 10 and 15 m. (The summary applies to systems using visible or IR radiation. For RF systems the conclusions would be somehat different, as mentioned earlier.)

When the ASTD is negative, the set of ray trajectories passing through the sensor folds over on itself, and has an envelope or caustic. The target suddenly becomes visible when it crosses the caustic; no matter how bright it is, the target cannot be seen before then. The target's crossing of the caustic thus defines a MIVR which is independent of the details of the sensor, target, and atmosphere. The MIVR for a target of arbitrary brightnes in an atmosphere having negative ASTD is smaller than the detection range of a bright target flying at the same altitude in an atmosphere with positive ASTD. When the target first appears (i.e., at the MIVR), its apparent direction is above the direction of the straight-line horizon. As it approaches closer, the image of the target splits into a two-fold mirage, because two rays through the sensor pass through the target. The upper branch of the mirage rises at first, but then drops as the target comes close enough for refractive effects to become unimportant. In contrast, the lower branch of the mirage drops steadily as the target approaches. As the target gets closer, the ray responsible for the lower branch of the mirage dips ever closer to the surface between the source and the sensor. In most cases, surface or near-surface effects will terminate the lower branch of the mirage; in the remaining cases, the lower branch of the mirage eventually becomes the image of the target reflected by the surface. The factors controlling the visibility of the lower branch of the mirage are more numerous and difficult to model than those controlling most refractive effects of interest, since they involve details of the sensor, target, surface, and near-surface, and not just information contained in the ray trajectories. However, the angular separation between the two branches of the mirage is easily calculated as a function of target range. The apparent horizon should be fairly sharp, but its direction (and consequently, the range of the target when it first must be distinguished from surface clutter) is difficult to calculate. In addition to the same complicating factors which afflicted the lower branch of the mirage, the apparent horizon may be influenced by the pattern of cloud cover and by the location of the Sun. In this report, only indicative results could be presented on the duration of the lower branch of the mirage and on the direction of the clutter horizon.

Before turning to the corresponding results for positive ASTD, it is useful to point out a corollary of the results for negative ASTD. It is sometimes asserted that good angular resolution is unèccessary for ship-based horizon-scanning IRST, because turbulence would worsen the effective resolution to that of a sensor having only moderate resolution. Despite turbulence, good angular resolution is needed for the following reason. For a given speed of the horizontal wind, turbulence is strongest when the air is

hydrostatically unstable, that is, when the ASTD is more negative than it would be for the adiabatic lapse rate. Strongly negative ASTDs produce mirages. In a mirage, the upper image is produced by rays which never dip into the region significantly affected by turbulence and aerosols, whereas the lower image is likely to be degraded. Detection and tracking should be based on the upper image; the lower image, when it is good enough to be detected at all, should be used only as a check. The resolution of the sensor must be good enough to distinguish between the upper and lower images. (The PtSi data showed turbulence to be confined to a narrow range of directions, where it does not undermine the possibility of separating the two branches of the mirage: the point spread function of the optics fully accounts for the observed width of the pip in Fig. 44, which shows the turbulent blurring to have been negligible. The limited role of turbulence is further indicated by the smallness of the angular width of the wavy turbulent horizon: in the field observations the waviness occurred only in the vicinity of the horizon, and did not affect the rest of the angular range.)

When the ASTD is sufficiently positive, the set of rays through the sensor bifurcates into a set of rays which eventually rise without limit and a set of rays which eventually strike the surface. It is as if the bundle of rays were torn. The region below the middle of the tear acts as a refractive duct to rays launched nearly horizontally below the duct. No mirage occurs: the image of the target first rises, then falls, much like that of the upper branch of a mirage. The density of rays through the sensor is very low in the vicinity of the tear, increasing gradually as the target approaches. The target therefore becomes visible gradually. The detection range depends upon details of the sensor, target, and atmosphere; there is no MIVR, deducible solely from the ray trajectories, as there was for negative ASTD. (Although the MIVR does not exist for sufficiently positive ASTD, the plots in this report have used the term MIVR for all ASTD. The alternative would have been to say "the range from which the detection range can be deduced, given additional details" for positive ASTD.) A sufficiently bright target at a given altitude (above the duct height) can potentially be seen at much larger ranges when the ASTD is positive than when the ASTD is negative. Curves were presented which allow the detection range to be determined when additional information about the sensor and target are provided. If surface reflections are weak, a target flying below the duct height cannot be seen until it is so close that it is seen against the background of the surface. The apparent horizon should be fuzzy and indistinct, and should be relatively featureless: the effects of glint, aerosols, and turbulence are all suppressed by the small density of rays near the edges of the tear. Surface clutter is confined to directions below the apparent direction of the refractive duct (which itself is featureless as seen from a sensor above the duct height), so the height of the refractive duct provides a useful ceiling on the apparent directions in which the target will be seen against surface clutter.

Application of the refractive model to field data was illustrated in a preliminary way. Despite the crudeness of the analysis, the model seems capable of explaining the observed refractive effects. Under the conditions of measurements in the field, it is often difficult to determine the absolute direction of a sensor having a narrow field of view. The method of analysis presented here showed how the angular origin used in the measurements can be estimated from the data itself, together with the model. This permits more aspects of the model to be tested than would otherwise be possible. It is likely to be particularly useful if there are future measurements to assess the factors which determine the apparent horizon. The only data needed for estimating the absolute angular origin are the true range and the apparent direction (expressed as a relative angle) of the target's point of maximum apparent elevation. These data are far easier to measure than the maximum detection range.

Appendix
UNFAVORABLE ATMOSPHERIC AND GEOGRAPHIC CONDITIONS

All of the approaches discussed in this report rely on simplifying assumptions: horizontal statistical homogeneity, domination of vertical profiles by wind-driven turbulence, neglect of turbulent fluctuations in refraction, and neglect of clouds, fog, and aerosols. These assumptions are likely to fail in unfavorable weather or geography. It is useful to recognize unfavorable conditions while performing experiments and while using sensors operationally. The unfavorable conditions are identified in this section. The first subsection enumerates conditions which are likely to invalidate the assumptions of horizontal homogeneity; the second subsection enumerates conditions which are likely to invalidate the assumed vertical profiles; the third discusses refractive turbulence, and the fourth discusses clouds, fog, and aerosols.

Horizontal Inhomogeneity and Anisotropy

In the present political climate, naval forces are more likely to find themselves standing off a hostile shore than facing an enemy on the high seas. Experimental tests of refractive models for horizon-searching are also usually performed relatively close to the shore. For both reasons, it is useful to be aware of offshore phenomena which sometimes invalidate the assumption of horizontal homogeneity.

When dry, stable, subsiding over-land air moves out over warm water, the refractive profile strongly disagrees with that predicted by the Monin-Obukhov theory (Gossard, 1982). Spectacular mirages can occur. The effects are so severe that "the prediction of ducting based on sea and air temperature over the path failed badly and caused a program for incorporation of duct prediction into fleet procedures to be abandoned" (Gossard, 1982). These refractive conditions sometimes occur off the coast of southern California; Gossard expects them to occur also in the eastern Mediterranean and in "the monsoonal regions of the Near East and Southeast Asia."

Horizontal gradients of surface temperature can occur in bays; see e.g., Davidson et al. (1981, p. 2921).

Horizontal inhomogeneities can develop without the presence of land: horizontal homogeneity frequently fails after the passage of a squall line or front, as repeatedly stressed by Bowditch (1966). The boundaries of warm or cold currents are also likely to produce horizontal inhomogeneity.

Vertical Problem

The Monin-Obukhov similarity profiles do not always apply at all heights relevant to the horizon searching-problem.

The surface layer swells during the day and shrivels at night; it can be as thin as 10 m at night (e.g., Panofsky and Dutton, 1984, p. 113). When the surface layer becomes this thin, the sensor lies above

the region of validity of the similarity profiles, and the target may lie above it as well. Ray tracing based on similarity profiles may still be fairly accurate for negative ASTD, since much of the important bending then occurs at low altitudes. But when the ASTD is positive and the rays from the target correspond to the upper branch of the tear (Fig. 3(b)), the relevant rays may all stay above the region of validity of the similarity profiles.

The similarity profiles apply only when wind-driven turbulence and gravitational stratification jointly determine the dynamics. At times, turbulence may be absent, or may be strong but driven by thermal convection rather than by the horizontal wind. Turbulence is absent when the winds are weak or when the hydrostatic stability of the atmosphere is sufficient to damp out wind-driven turbulence; convection is important when the atmosphere is hydrostatically unstable. Some of these conditions are common enough to be included in the typical diurnal cycle (e.g., Livingston, 1970, pp. 99-101). Monin-Obukhov similarity is less accurate under hydrostatically stable conditions: see Kretschmer, Foken, and Kottmeier (1991). When convective turbulence is important, a "mixed" layer may occur in which the wind and potential temperature vary little with height; the mixed layer is described by a similarity theory different from Monin-Obukhov similarity theory (Panofsky and Dutton, 1984, pp. 116). However, over the ocean there are occasions when neither of the similarity theories apply (Panofsky and Dutton, 1984, pp. 117).

The similarity profiles are inapplicable in the offshore meteorological conditions described by Gossard (1982), as described in the previous subsection.

Turbulent Refraction

The ray tracing programs discussed in this report presently ignore turbulence-induced refractive fluctuations: turbulence is included only insofar as it influences the vertical profile of the average refractive index.

Turbulence can be taken into account either by tracing rays or by solving transport equations. Solving transport equations would require a computer code very different from those hitherto used for analyzing refraction in the horizon searching problem, and would require considerable computer time. Hence only the ray tracing options will be discussed here. Ray tracing can be performed at two levels of accuracy and computer time: deterministic ray tracing in the averaged medium, with the cumulative effects of refraction estimated by integrating along the deterministic refracted ray; and Monte Carlo (non-deterministic) ray tracing. Both techniques are reviewed in Hornstein (1977). The use of integrals along rays in the averaged medium can be viewed as solving the transport equations perturbatively, whereas Monte Carlo ray tracing can be viewed as the Monte-Carlo evaluation of a path-integral reformulation of the transport equations. The former technique would require little modification of the existing ray tracing codes described earlier and would require hardly any additional computer time, but would cease to be valid over long paths (where the cumulative RMS turbulent angular deviation exceeded about 10°). The Monte Carlo technique is not limited to weak turbulent refraction, but is very time-consuming: estimates must be based on an entire ensemble of rays.

Monin-Obukov similarity theory provides profiles of the second order statistics needed by all of the methods used for computing turbulent refraction. The present report discussed only the Monin-Obukhov similarity profiles for first order statistics (means), however all of the references cited in the Section on Monin-Obukhov similarity also have material on similarity profiles for second order statistics.

Turbulence effects seem to be small in much of the data discussed in this report. They are likely to be significant for the lower image in a mirage. But since the lower image in a mirage is less useful than

the upper image, the inclusion of turbulent refraction may not be worth the effort and increased computer time.

Clouds, Fog and Aerosols

The MIVR gives only partial information on the maximum range at which targets will first be detected, because the MIVR does not include attenuation or the effect of clutter upon detectability.

When the shore is not visible in the directions of interest, the main potential sources of clutter are clouds, sea glint, turbulence, and birds. Of these, only clouds will be discussed here. In near-horizon scanning, clouds are rarely noticeable in directions close to the horizon. Most of the radiance from long, relatively attenuating surface-grazing paths is path radiance from regions nearer than the nearest cloud, unless the rays intercept a target. When attenuation and non-cloud clutter do not have a significant effect upon detectability, clouds do not either, and the MIVR then gives a good indication of detectability.

Attenuation is caused by the geometric spreading of rays produced by both mean refraction and turbulence, by turbulent redirection (without spreading) of rays, and by absorption and scattering by aerosols. Attenuation caused by ray divergence in mean refraction is not yet included in the ALLRAYS and RAYS ray tracing codes, although with some difficulty it could be included; it is included in DREV's ray tracing code. Potential methods of including attenuation caused by the turbulent redirection and spreading of optical beams were discussed earlier, but, as noted earlier, these sources of attenuation are probably not important in the horizon-searching problem. Except in fog, attenuation by aerosols falls off rapidly with height. Therefore, non-fog aerosol-induced attenuation should only be important for the lower image in a mirage, and hence should not be critical in horizon-searching. (The lower branch of a torn bundle of rays (positive ASTD) is too low for most targets.) DREV has extensively discussed aerosol effects. They are one of the main remaining unknowns, and play an important role in the controversy on how to treat near-surface rays. LOWTRAN (Kueizys et al., 1988) provides models of attenuation by low-altitude aerosols.

Attenuation by fog aerosols does not fall off rapidly with height. Electro-optic horizon-searching sensors cannot provide useful information under foggy conditions. Attack by infrared guided missiles is also unlikely in fog, for the same reason. Radar warning sensors and radar-guided missiles are both feasible in fog.

Rain is not strictly an aerosol, but should be discussed here. Rain strongly degrades target detection by both infrared and radar sensors. But attacking missiles are unlikely to be knowingly launched toward a rain-shrouded target, because both infrared and radar guidance systems will be degraded as well.

BIBLIOGRAPHY

Atlas, D., R.M. Cunningham, R.J. Donaldson, Jr., G. Kantor, and P. Newman. 1965. "Some aspects of electromagnetic wave propagation," Chapter 9 (pp. 9-1 to 9-26) in Valley, S.L. (ed.), *Handbook of Geophysics and Space Environments*, McGraw-Hill, New York.

Beaulieu, A.N. 1992. "Atmospheric Refraction Model and the Effects of Surface Waves," DREV report DREV R-4661/92, CDRV R-4661/92, Defence Research Establishment (DREV), Centre de Recherches Pour la Defense (CRDV), Valcartier, Canada.

Blanc, T.V. 1986. "Superstructure Flow Distortion Corrections for Wind Speed and Direction Measurements Made from Tarawa Class (LHA1-5) Ships," NRL Report 9005.

Bowditch, N. et al. 1966. *American Practical Navigator*, U.S. Government Printing Office, Washington, D.C.

Born, M. and E. Wolf. 1980. *Principles of Optics* (6th edn.), Pergamon Press, Oxford.

Charnock, H. 1958. "A note on empirical wind-wave formulae," *Quart. Jl. Roy. Met. Soc.* **84**, 443-447.

Cox, C. and W. Munk. 1954. "Measurement of roughness of the sea surface from photographs of the sun's glitter," *Jl. Opt. Soc. Am.* **44**, 838-850.

Crane, R.K. 1976. "Refraction effects in the neutral atmosphere," Chapter 2.5 (pp. 186-200) in M.L. Meeks (ed.), *Astrophysics (Part B: Radio Telescopes)* (vol. 12 in L. Marton (ed.), *Methods of Experimental Physics*), Academic Press, New York.

Davidson, K.L., G.E. Schacher, C.W. Fairall, and A.K. Goroch. 1981. "Verification of the bulk method for calculating overwater optical turbulence," *Applied Optics* **20**(17), 2919-2924.

Dion, D., B. Leclerc, and C. Lassonde. 1989. "Investigation of the air refractivity effects on IR sensors in the marine boundary layer," unofficial DREV memorandum.

Donelan, M.A. and W.J. Pierson. 1987. "Radar scatter and equilibrium ranges in wind-generated waves with applications to scatterometry," *Jl. Geophys. Res.* **92**, 4971-5029.

Edlén, B. 1953. "The dispersion of standard air," *Jl. Opt. Soc. Am.* **43**(5), 339-344.

Feinberg, R. and H.G. Hughes. 1979. "Marine boundary layer refractive effects in the infrared," *Applied* Optics **18**(15), 2532-2534.

Fulkerson, S.A., J.D. McGlynn, and R.F. Rauchmiller. 1989. "Infrared simulation of ocean thermal clutter," IRIA-IRIS Proceedings of the 1989 Targets, Backgrounds and Discrimination meeting.

Goody, R.M., *Atmospheric Radiation*, Oxford Univ. Press, Oxford, 1964. (The 1989 second edition, by R.M. Goody and Y.L. Yung, does not discuss the refractive index of air.)

Gossard, E.E. 1982. "Formation of elevated refractive layers in the oceanic boundary layer by modification of land air flowing offshore," *Radio Science* **17**(2), 385-398.

Hepfer, K., (NSWC/Dahlgren), personal communication, 1992.

Hess, S.L. 1979. *Introduction to Theoretical Meteorology*, Holt, Rinehart & Winston, 1959; reprinted by Robert E. Krieger Pub. Co., Huntington, New York.

Hill, R.J., S.F. Clifford, and R.S. Lawrence. 1980. "Refractive-index and absorption fluctuations in the infrared caused by temperature, humidity, and pressure fluctuations," *Jl. Opt. Soc. Am.* **70**(10), 1192-1205.

Hill, R.J. and R.S. Lawrence. 1986. "Refractive index of water vapor in infrared windows," *Infrared Physics* **26**(6), 371-376.

Holton, J.R. 1979. *An Introduction to Dynamic Meteorology* (2nd. edn.), Academic Press, New York.

Hornstein, J. 1981. "Ray Methods in Random Media," pp. 16-25 in R.W. Fenn (ed.), *Atmospheric Transmission*, SPIE Proceedings 277.

Hughes, H.G. 1989. "Apparent infrared radiance of the sea," NOSC Technical Report 1271.

Iribarne, J.V. and W.L. Godson. 1981. *Atmospheric Thermodynamics* (2nd edn.), D. Reidel Pub. Co., Dordrecht.

Kerr, D.E. (ed.). 1951. *The Propagation of Short Radio Waves*, MIT Rad. Lab. Rept., McGraw-Hill, New York, 1951; reprinted by Dover.

Kessler, B.V. et al. 1989. "New IRAMMP dual-band radiometric sensor," IRIA-IRIS Proceedings of the 1989 Targets, Backgrounds and Discrimination meeting.

Kinsman, B. 1984. *Wind Waves*, Prentice-Hall, Inc., Englewood Cliffs, New Jersey, 1965; reprinted by Dover Publications, New York.

Kneizys, F.X. et al. 1988. "User's guide to LOWTRAN 7," AFGL-TR-88-0177, AFGL.

Kretschmer, D., Th. Foken, and Ch. Kottmeier. 1991. "Experimentelle untersuchungen zu parameterisierungsansätzen für die stabile bodenschicht," *Z. f. Meteorol.* **41**(6), 430-438.

Livingston, D.C. 1970. *The Physics of Microwave Propagation*, Prentice-Hall, Inc., Englewood Cliffs, New Jersey.

Longuet-Higgens, M.S. 1952. "On the statistical distribution of the heights of sea waves," *Jl. Marine Research*, **XI**(3), 245-265.

Low, T.B. and D.R. Hudack. 1990. Draft Final Report on the "Development and Testing of a Marine Boundary Layer Model," Kel Research Corporation, 850-A Ainess Street, Suite 9, Downsview, Ontario, Canada M3J 2H5.

Monin, A.S. 1973. "Boundary layers in planetary atmospheres," pp. 419-468 in P. Morel (ed.), *Dynamic Meteorology*, D. Riedel Pub. Co., Dordrecht.

Monin, A.S. and A.M. Yaglom. 1971. *Statistical Fluid Mechanics* (vol. 1), Nauka Press, Moscow, 1965 (in Russian); English edition: MIT Press, Cambridge, Mass.

Moskowitz, L. 1964. "Estimates of the power spectrums of fully developed seas for wind speeds of 20 to 40 knots," *Jl. Geophys. Res.* **69**(24), 5161-5179 and 5202-5203.

Owens, J.C. 1967. "Optical refractive index of air: dependence on pressure, temperature and composition," Applied Optics **6**(1), 51-59.

Panofsky, H.A. and J.A. Dutton. 1984. *Atmospheric Turbulence*, John Wiley & Sons, New York.

Patterson, W.L., C.P. Hattan, H.V. Hitney, R.A. Paulus, A.E. Barrios, G.E. Lindem, and K.D. Anderson. 1990. "Engineer's Refractive Effects Prediction System (EREPS) Revision 2.0," NOSC TD 1342, Naval Ocean Systems Center, San Diego, CA.

Paulson, C.A. 1970. "The mathematical representation of wind speed and temperature profiles in the unstable atmospheric surface layer," *Jl. Appl. Meteorol.* **9**, 857-861.

Paulus, R.A. 1991. "Validation of the bulk method for overwater optical refractivity," NOSC Technical Report 1462.

Penndorf, R. 1957. "Tables of the refractive index for standard air and the Rayleigh scattering coefficient for the spectral region between 0.2 and 20.0 μ and their application to atmospheric optics," *Jl. Opt. Soc. Am.* **47**(2), 176-182.

Pierson, W.J., Jr. 1964. "The interpretation of wave spectrums in terms of wind profile instead of the wind measured at a constant height," *Jl. Geophys. Res.* **69**(24), 5191-5203.

Pierson, W.J., Jr. and L. Moskowitz. 1964. "A proposed spectral form for fully developed seas based on the similarity theory of S./ A. Kitaigorodskii," *Jl. Geophys. Res.* **69**(24), 5181-5190 and 5202-5203.

Priest, R.G. and I.B. Schwartz. 1988. "A probabilistic model of the radiance of a rough sea," NRL Memorandum Report 6092.

Priest, R.G., E.P. Shettle, and E.H. Takken. 1992. "High resolution imagery of the sea horizon: data and modeling," IRIA-IRIS Proceedings of the 1992 Targets, Backgrounds and Discrimination meeting.

Priestley, C.H.B. 1959. *Turbulent Transfer in the Lower Atmosphere*, Univ. of Chicago Press, Chicago.

Rees, W.G., C.M. Roach, and C.H.F. Glover. 1991. "Inversion of atmospheric refraction data," *J. Opt. Soc. Am. A*, **8**(2), 330-338.

Rogers, R.R. 1979. *A Short Course in Cloud Physics* (2nd edn.), Pergamon Press, Oxford.

Takken, E.H., R.G. Priest, E.P. Shettle, and J.C. Kershenstein. 1991. "IR horizon phenomenology: report on IRAMMP field test," IRIA-IRIS Proceedings of the 1991 Targets, Backgrounds and Discrimination meeting.

Tatarskii, V.I. 1971. *The Effects of the Turbulent Atmosphere on Wave Propagation*, English translation: Israel Program for Scientific Translations, Jerusalem.

Walmsley, J. 1988. "On theoretical wind speed and temperature profiles over the sea with applications to data from Sable Island, Nova Scotia," *Atmosphere-Ocean* **26**(2), 203-233.

Wells, N. 1986. *The Atmosphere and Ocean: A Physical Introduction*, Taylor & Francis, London.